UNIVERSITY OF SOUTHAMPTON

HIGH RESOLUTION SPECTROSCOPY OF GAS PHASE FREE RADICALS

by

Christopher R. Brazier

A dissertation submitted in partial fulfilment of the requirements for the degree of Doctor of Philosophy at the University of Southampton.

October 1983

UNIVERSITY OF SOUTHAMPTON

ABSTRACT

FACULTY OF SCIENCE

CHEMISTRY

Doctor of Philosophy

HIGH RESOLUTION SPECTROSCOPY OF GAS PHASE FREE RADICALS

by Christopher R. Brazier

Laser induced fluorescence has been used to obtain spectra of diatomic free radicals. The structure observed was examined in greater detail by two high resolution techniques, microwave optical double resonance and intermodulated fluorescence.

The first molecule studied was CuF for which recording of a previously unobserved sub-band has allowed conclusive identification of the upper state in the yellow system as $b^3\Pi$. The hyperfine structure has been examined and the seven constants determined are interpreted in terms of the electronic configurations which could give rise to a $^3\Pi$ state. The lambda doubling and spin-rotation parameters are compared with calculated values based on perturbations due to the $a^3\Sigma^+$ state.

The ground state microwave spectrum of the CH radical has been observed for the first time in the laboratory. These measurements have been used to determine improved lambda doubling and hyperfine constants, and make accurate predictions for possible astrophysical observations. The $A^2\Delta$ state has been examined in detail and effects due to the very small lambda doubling in this state observed. A fourth order perturbation treatment is used to obtain calculated values for comparison. The three proton hyperfine parameters for the $^2\Delta$ state have been determined and it is shown that the wavefunction involves a significant hydrogen 1s contribution.

Initial, but so far unsuccessful attempts to observe the ground state microwave spectrum of SiH by MODR are also described.

ACKNOWLEDGEMENTS

I would like to thank John Brown, my supervisor for much help and guidance throughout my PhD. I would also like to express my gratitude to Tim Steimle who showed me how to perform the experiments described here and with whom most of the results for CuF were obtained. I very much appreciate the efforts of Agnes Stewart who entered my thesis into the computer, this thesis having been produced on a C-ITOH 8600 printer using a SIRIUS computer. Finally I would like to thank my mother for her continued support throughout my period of research.

CONTENTS

Chapter 1 Introduction

Great interest exists in free radicals in many areas, most having little direct concern with their study. Among the more important of these are kinetic studies involving free radicals as reactive intermediates and photochemistry where the production of very small quantities of radicals can lead to extensive chain reactions. The term free radical is usually taken to mean any molecule possessing unpaired spin or orbital angular momentum. This includes such common stable species as NO and NO_2 together with O_2 in its ground state, although the unstable second excited state of O_2 would not be considered a free radical. Similarly unstable molecules such as CS and HNO would not be termed radicals.

Another major area of importance for free radicals is the upper atmosphere which is subject to large amounts of electromagnetic radiation and high energy charged particles leading to radical production. The fairly low molecular density means that quite large populations of these species can be built up. Much interest exists in the complex chemical processes in the upper atmosphere and particularly the effects of the various breakdown products of atmospheric pollution such as CF, CCl and NO on the level of ozone. These species are likely to initiate chain reactions and thus can be very important even in very low concentrations.

The interstellar medium being subject to large amounts of radiation and with an extremely low molecular density, is an ideal environment for building up large quantities of free radicals. This was an area of particular interest for the research carried out here because while many radicals such as OH, NO, NS, ClO, CN have already been seen, several important species which are thought to exist in high concentrations have been extremely elusive. The CH radical is of particular interest in such studies as it can lead to the production of more complex organic molecules, and for many years it could not be seen. There have been many observations of CH in its lowest rotational level in different

interstellar sources, since its first observation, but much interest remains in the extent of rotational excitation in the different sources and one of the aims of this work was to measure the ground state microwave spectrum, as more accurate knowledge of the transition frequencies is likely to make observation much easier. Despite many searches using microwave absorption and electron paramagnetic resonance, this spectrum of CH has remained elusive to laboratory observation. The technique of microwave optical double resonance, which essentially involves using fluorescence detection to monitor microwave transitions, is vastly more sensitive however, particularly when dealing with short lived species, which are hard to obtain in high concentration. By this means we have made the first laboratory observation of the microwave spectrum of CH and together with other measurements this has led to the very accurate evaluation of the transition frequencies which may be observed astrophysically. It was very pleasing to learn during the composition of this thesis of the observation of CH in an excited rotational level, the search having been made on the basis of our predictions, the measured frequencies agreeing with our calculations to better than 10kHz.

The SiH molecule is also of much astrophysical interest and has not yet been seen in the interstellar medium. It was hoped to perform similar experiments on this species to those on CH but the very difficult region of the optical transition made this impossible. Acquisition of an improved laser system should make the relevent transitions accessible and allow measurement of the so far unobserved ground state microwave spectrum.

Many molecules which are stable solids on earth are dispersed in the gas phase in interstellar sources. While these molecules are not usually free radicals the high temperatures required for their production, frequently involving the reaction of a metal with an oxidising agent, mean that the same techniques are required for their study. Some of these species such as SiO have been seen but others for example BaO and MgO are thought to exist in quite high

concentration but so far have not been observed. Such species are of particular importance as it is thought that they form clusters which can act as catalytic surfaces for interstellar reactions. The microwave spectrum of BaO was measured by MODR some time ago and that of MgO has recently been recorded.

Other species such as CuF have $^1\Sigma^+$ ground states but have many excited states with unpaired angular momentum, which show many interesting effects. The yellow system of CuF has also been considered as a possible basis for a chemical laser because the reaction of copper and fluorinating agents leads to strong fluorescence in this region. The transition involved is quite strong but the fluorescent lifetime is also reasonably long so that a population inversion could be maintained. Clearly if such a laser is to be developed a thorough understanding of the energy levels involved is required. At the beginning of our study even the nature of the excited state was not known. The high sensitivity of laser induced fluorescence has resulted in the detection of a strongly dis-allowed sub-band of the system leading to a conclusive assignment for the transition.

The presence of unpaired spin and orbital angular momenta leads to coupling between different electronic states. This causes perturbation of the energy levels, for example in a Π state the two orientations of Λ along the internuclear axis are degenerate but mixing with Σ states splits the levels apart leading to Λ type doubling. Measurement of such splittings leads to the determination of effective constants describing the interaction which may then be interpreted in terms of the states causing the perturbations.

If one of the nuclei in the molecule has a spin magnetic moment then this can interact with the unpaired electron leading to nuclear hyperfine splittings. These provide a direct probe of the nature of the electronic wavefunction in the region of the nucleus. Hence determination of hyperfine constants can lead to important

information about both the electronic state, and the possible configurations which could contribute to this. Nuclear hyperfine splittings are usually quite small and require high resolution techniques to observe them, although in the case of CuF such structure was visible at Doppler-limited resolution. MODR in the excited state which has a resolution of typically 5 MHz is a very useful means of observing such splittings although for most molecules only the lowest levels may be investigated as the transition frequencies rapidly move out of the microwave region. However other types of transition, such as lambda doubling and spin-rotation, allow extension to higher energy levels as well as to very light molecules like CH where even the first rotational transition is in the far infrared.

Another method of probing hyperfine structure is the use of intermodulated fluorescence to observe splittings obscured by the Doppler profile. This technique does not offer quite as high a resolution as MODR typically 30 MHz but as only one radiation source is required it is somewhat easier. It is also possible to examine virtually all of the levels of interest, providing the transitions involved are of sufficient intensity.

The next three chapters of this thesis contain, respectively, a description of the molecular Hamiltonian used to interpret the results, an explanation of the high resolution techniques used and a review of the fitting procedure used to obtain effective constants. Chapter 5 contains a description and interpretation of the measurements made on CuF. The results obtained on CH together with their analysis is given in Chapter 6 while the final chapter contains a description of the attempt to perform similar measurements on SiH.

Chapter 2 The Effective Hamiltonian

Coupling Schemes

For molecules possessing unquenched spin or orbital angular momenta there exist various ways in which these momenta may be coupled together. The possible coupling schemes which can arise were originally investigated by Hund (1) who showed that there were five possibilities, designated a, b, c, d and e. Of these only the first three are of importance for diatomic molecules with cases a and b occurring most commonly for light molecules.

The angular momenta of the non-rotating molecule consist of the orbital angular momentum of the electrons L, and their spin angular momentum S. The way in which L and S couple with the rotational motion of the molecule R is dependent on the size of the spin-orbit coupling relative to the coupling with the rotational angular momentum this depends on $|A/2B|$. If this quantity is very large, a situation which occurs mainly for heavy molecules then the appropriate scheme is case c shown in figure 1. Here the spin and orbital angular momenta couple together to give a resultant J_a. Due to the cylindrical symmetry of the molecule this will precess about the internuclear axis and consequently only its projection onto that axis, Ω, remains a constant of the motion. This then couples with R to give the total angular momentum J. While Ω the projection of J_a is a good quantum number, the strong coupling of L and S means that their individual projections Λ and Σ are no longer well defined and thus the usual designations such as $^2\Sigma^+$, $^2\Pi$ et cetera can not be used, the states instead being labelled by Ω.

If $|A/2B|$ is somewhat smaller, then L and S no longer couple together, L continues to precess about the internuclear axis and thus only Λ its projection onto that axis remains well defined. The spin-orbit coupling remains strong enough however to orient the spin S so that its magnetic moment Σ lies along the internuclear axis. This is

Figure 1. Hund's case c which occurs when there is a large spin-orbit interaction. The orbital **L** and spin **S** angular momenta couple together to give a resultant J_a which precesses about the internuclear axis.

Case c

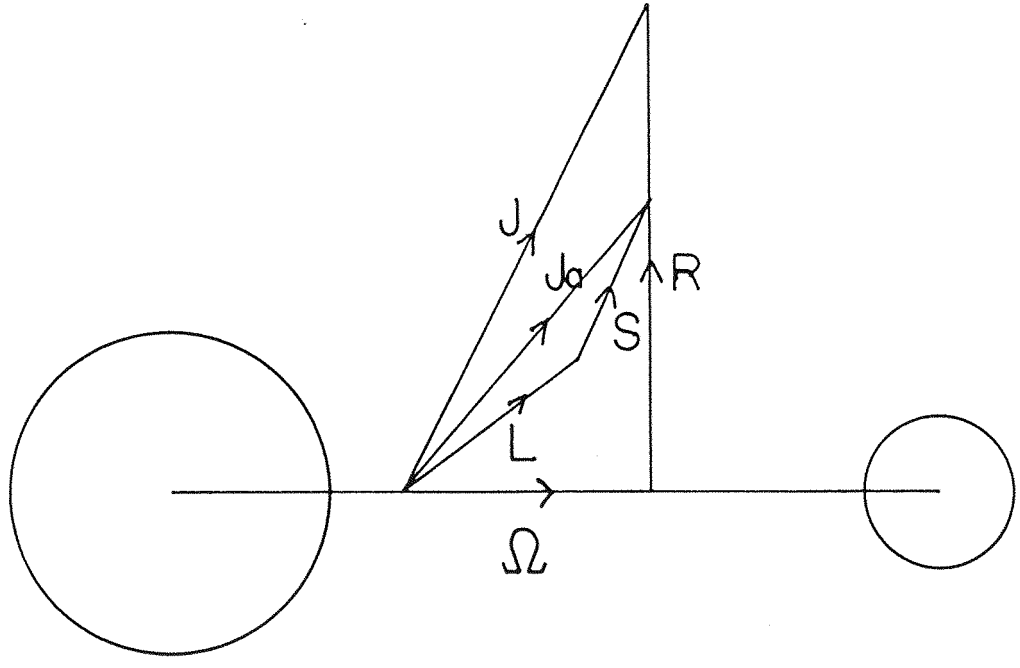

$$J_a = L + S$$

$$J = R + |\Omega|$$

Figure 2. Hund's case a for intermediate spin-orbit interaction with both L and S precessing separately about the internuclear axis. CuF obeys this type of coupling, the two nuclear spins are added as shown by $a_{\beta J}$ coupling. As the effect of the copper nucleus is greater, this is chosen as I_1.

Case $a_{\beta J}$

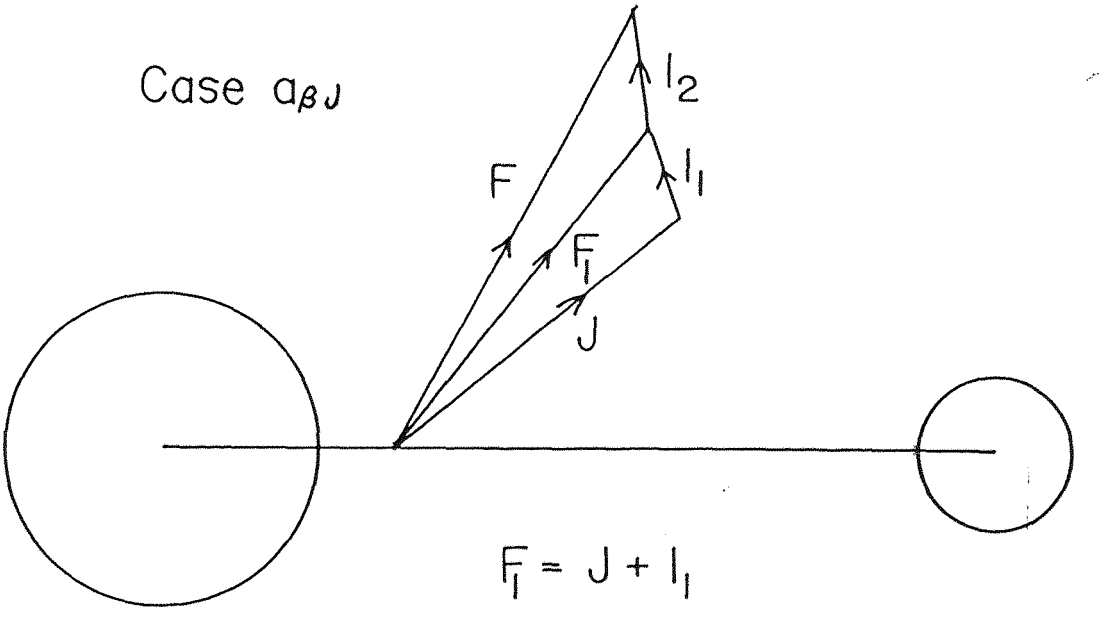

$$F_1 = J + I_1$$
$$F = F_1 + I_2$$

Case a

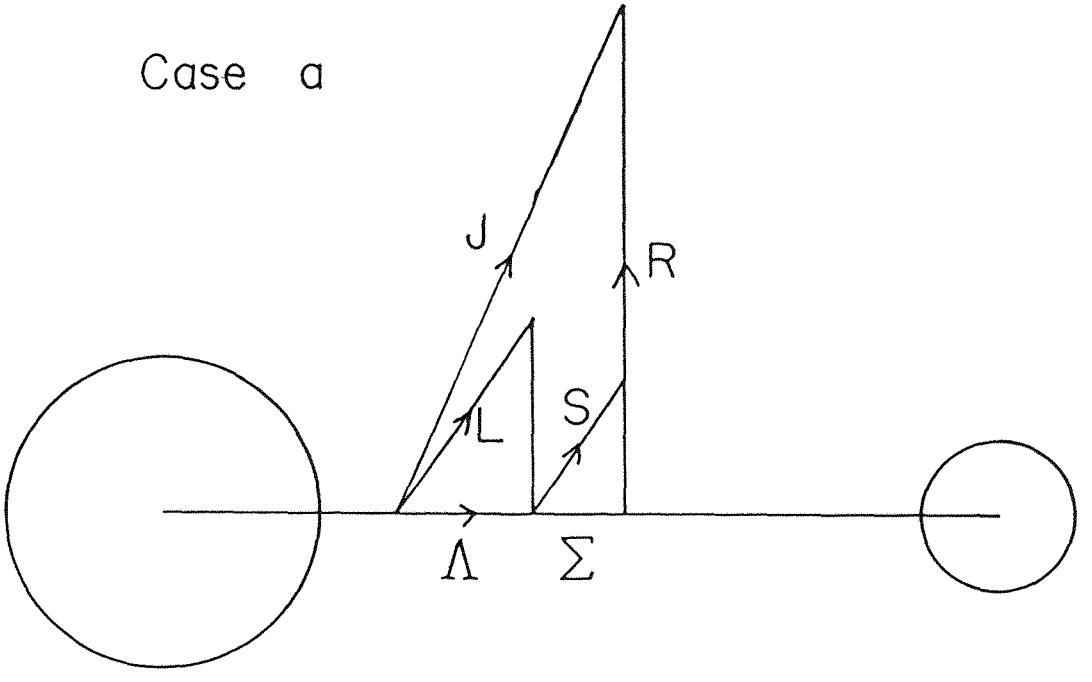

$$\Omega = \Lambda + \Sigma$$
$$J = R + |\Omega|$$

Figure 3. Hund's case b where the spin-orbit interaction is small, and the spin S is no longer coupled to the internuclear axis. This is the situation which occurs for CH, the proton spin is then coupled to J in a similar way to CuF, giving the overall scheme $b_{\beta J}$.

Case b

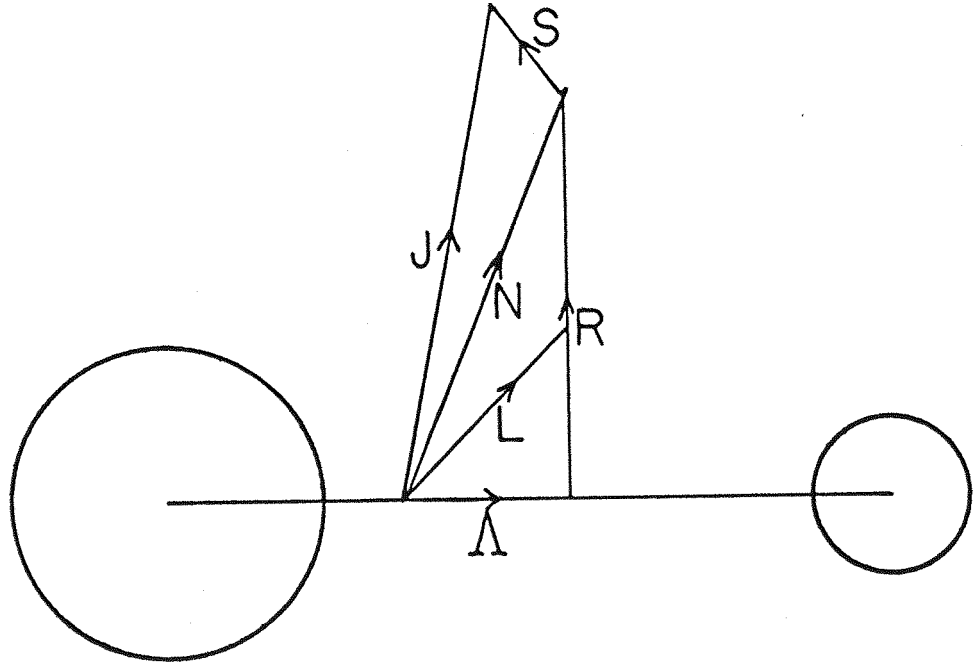

$$N = R + |\Lambda|$$

$$J = N + S$$

case a coupling shown in figure 2. CuF in its $b^3\Pi$ state is best represented by case a coupling and here $|\Lambda| = 1$ and Σ which can take on values S,S-1,..,-S is equal to 1, 0 or -1. The two projections couple together to give a resultant Ω

$$\Omega = \Lambda + \Sigma \qquad 2.1$$

this takes on values $|\Omega| = 0$, 1 and 2 leading to the three $^3\Pi$ sub-states $^3\Pi_0$, $^3\Pi_1$ and $^3\Pi_2$. Each of these is doubly degenerate as Λ may equal ± 1 and thus $\Omega = \pm(0,$ 1 or 2). L and S are coupled with the rotational angular momentum R to produce the total angular momentum J

$$J = R + L + S \qquad 2.2$$

A further quantum number N the total angular momentum without spin is also used

$$N = J - S \qquad 2.3$$

If $|A/2B|$ is small then the spin angular momentum S is no longer coupled to the internuclear axis, this is case b coupling shown in figure 3. L remains coupled to the internuclear axis and couples with the rotational motion R to give the resultant N

$$N = R + L \qquad 2.4$$

This then couples with the spin S to give the total angular momentum J

$$J = N + S \qquad 2.5$$

As Σ the projection of S onto the internuclear axis is no longer well defined the sub-states cannot be labelled by their value for Ω. CH in both its $X^2\Pi$ and $A^2\Delta$ states is a good example of case b coupling, the sub-states are labelled F_1 and F_2 where for F_1 $J = N+\frac{1}{2}$ and for F_2 $J = N-\frac{1}{2}$.

When the nuclei possess spin angular momentum it is necessary to couple this with the other angular momenta. This also leads to several different schemes for each of the coupling cases so far described, but as only one of these occurs for the molecules being considered the others will not be discussed here. For CH only one nucleus has spin angular momentum and this is coupled with J, the scheme being designated $b_{\beta J}$, to give the total angular momentum F

$$F = J + I \qquad 2.6$$

For CuF both nuclei have spin and using the equivalent coupling scheme $a_{\beta J}$ they add to J as follows

$$F_1 = J + I_1 \qquad 2.7$$

$$F = F_1 + I_2 \qquad 2.8$$

Energy levels for the $b^3\Pi$ state of CuF

The good quantum numbers for a molecule in an $a_{\beta J}$ state have been derived in the previous section, if these are to be useful in evaluating the molecular energies then it is necessary to combine them in basis states which reflect the values of the quantum numbers. For a case $a_{\beta J}$ molecule the basis states are of the form

$$|\eta\ \Lambda;S\ \Sigma;J\ \Omega;I_1\ F_1\ I_2\ F\rangle \qquad 2.9$$

Where η represents the other vibrational and electronic quantum numbers not given explicitly. For CuF $I_2 = 1/2$ for the ^{19}F nucleus giving rise to two possible values of F_1 for each given F while $I_1 = 3/2$ for the ^{63}Cu nucleus giving a total of four J values for each F_1, ie a total of eight different basis states for a given total angular momentum F. For each J value there are six possible values of Ω hence there are in total 48 basis functions for each F. This is

somewhat unwieldy and it is likely to take rather a long time for a computer to diagonalise a matrix of this size, fortunately it is possible to reduce this by a factor of two by taking Wang combinations of the basis functions

$$2^{-1/2}(|\eta\ \Lambda;S\ \Sigma;J\ \Omega;I_1\ F_1\ I_2\ F\rangle \pm |\eta\ -\Lambda;S\ -\Sigma;J\ -\Omega;I_1\ F_1\ I_2\ F\rangle) \qquad 2.10$$

which have parities of $\pm(-1)^{J-S}$ respectively (2).

The effective Hamiltonian operator for the energy levels of a molecule in a $^3\Pi$ state (3)(4) is given by

$$\mathcal{H}_{eff} = \mathcal{H}_{rot} + \mathcal{H}_{cd} + \mathcal{H}_{cdcd} + \mathcal{H}_{ss} + \mathcal{H}_{sscd} + \mathcal{H}_{so} + \mathcal{H}_{socd} + \mathcal{H}_{sr} + \mathcal{H}_{LD} + \mathcal{H}_{hfs1} + \mathcal{H}_{hfs2} + \mathcal{H}_{Q} \qquad 2.11$$

where

$\mathcal{H}_{rot} = BN^2$ is the rotational energy 2.12

$\mathcal{H}_{cd} = -DN^2N^2$ is the first centrifugal distortion correction 2.13

$\mathcal{H}_{cdcd} = HN^2N^2N^2$ is the second centrifugal distortion correction 2.14

$\mathcal{H}_{ss} = 2/3\lambda(3S_z-S^2)$ is the spin-spin interaction 2.15

$\mathcal{H}_{sscd} = 2/3\lambda_D(3S_z-S^2)N^2$ is the centrifugal distortion correction to the spin-spin interaction 2.16

$\mathcal{H}_{so} = AL_zS_z$ is the spin-orbit interaction 2.17

$\mathcal{H}_{socd} = A_DL_zS_zN^2$ is the centrifugal distortion correction to the spin-orbit interaction 2.18

$\mathcal{H}_{sr} = \gamma N.S$ is the spin-rotation term 2.19

$\mathcal{H}_{LD} = 1/2(o+p+q)(S_+^2+S_-^2)-1/2(p+2q)(J_+S_++J_-S_-)+1/2q(J_+^2+J_-^2)$ is the lambda doubling term 2.20

$\mathcal{H}_{hfs1} = a_1I_{1z}L_z+b_{F1}I_1.S+1/3c_1(3I_{1z}S_z-I_1.S)-1/2d(S_+I_{1+}+S_-I_{1-})$ is the magnetic hyperfine term for the copper nucleus 2.21

$$\mathcal{H}_{hfs2} = a_2 I_{2z} L_z + b_{F2} \mathbf{I}_2 \cdot \mathbf{S} + 1/3 c_2 (3 I_{2z} S_z - \mathbf{I}_2 \cdot \mathbf{S}) - 1/2 d (S_+ I_{2+} + S_- I_{2-})$$

is the magnetic hyperfine term for the fluorine nucleus 2.22

$$\mathcal{H}_Q = \frac{eq_0Q}{4I(I-1)} (3I_z - I^2) + \frac{eq_2Q}{8I(2I-1)} (I_+^2 + I_-^2)$$

is the electric quadrupole interaction for the copper nucleus 2.23

The rotational expressions are written in terms of N^2 rather than R^2, as this is now the accepted standard form (5). The lambda doubling parameters p and q are defined in the same form as that originally derived by Mulliken and Christy (6). While the third lambda doubling parameter o, which had previously been used to describe a non-determinable contribution acting equally on both lambda doublets, is used in the more consistent form described by Brown and Merer (3). The hyperfine expressions (7) consist of a the nuclear-spin orbit interaction, b_F the Fermi contact interaction, c the spin dipolar interaction and d the lambda doubling spin dipolar interaction. We have chosen to use b_F rather than Frosch and Foley's b (7) as this is more readily interpretable. They are related to each other as follows

$$b_F = b + 1/3\ c \qquad 2.24$$

The full set of hyperfine contributions are included although insufficient data were available to determine all of them.

The matrix elements between the effective Hamiltonian eqn 2.11 and the basis functions eqn 2.10 are readily evaluated using spherical tensor algebra (8)(9). Most of the elements are given by Brown et al (11), and the additional centrifugal distortion corrections are readily evaluated from the effect of the rotational matrix on the original terms. The hyperfine term for the second nucleus

which is not given, is shown below

$$\langle \eta\ \Lambda';S\ \Sigma';J'\ \Omega';I_1\ F_1'\ I_2\ F|\mathcal{H}_{hfs2}|\eta\ \Lambda;S\ \Sigma;J\ \Omega;I_1\ F_1\ I_2\ F\rangle$$

$$= (-1)^{F_1+I_2+F}\begin{pmatrix} F & I_2 & F_1' \\ 1 & F_1 & I_2 \end{pmatrix}[I_2(I_2+1)(2I_2+1)]^{1/2}$$

$$\times(-1)^{J'+I_1+F_1+1}\begin{pmatrix} I_1 & J' & F_1' \\ 1 & F_1 & J \end{pmatrix}[(2F_1'+1)(2F_1+1)]^{1/2}$$

$$\times\{\delta_{\Lambda'\Lambda}\sum_q(-1)^{J'-\Omega'}\begin{pmatrix} J' & 1 & J \\ -\Omega' & q & \Omega \end{pmatrix}[(2J'+1)(2J+1)]^{1/2}$$

$$\times[a\Lambda\delta_{\Sigma'\Sigma}\delta_{\Omega'\Omega}+b_F(-1)^{S-\Sigma'}\begin{pmatrix} S & 1 & S \\ -\Sigma' & q & \Sigma \end{pmatrix}[S(S+1)(2S+1)]^{1/2}$$

$$+\sqrt{(30)}/3c(-1)^{q+S-\Sigma'}\begin{pmatrix} S & 1 & S \\ -\Sigma' & q & \Sigma \end{pmatrix}\begin{pmatrix} 1 & 2 & 1 \\ -q & 0 & q \end{pmatrix}[S(S+1)(2S+1)]^{1/2}]$$

$$-d\sum_{q=\pm1}\delta_{\Lambda'\Lambda\pm2}(-1)^{J'-\Omega'}\begin{pmatrix} J' & 1 & J \\ -\Omega' & -q & \Omega \end{pmatrix}[2J'+1)(2J+1)]^{1/2}$$

$$(-1)^{q+S-\Sigma'}\begin{pmatrix} S & 1 & S \\ -\Sigma' & q & \Sigma \end{pmatrix}[S(S+1)(2S+1)]^{1/2}\} \qquad 2.25$$

The $^3\Pi$ Hamiltonian matrix for a molecule without hyperfine effects is of dimension 3 x 3, the basis states having the three possible values of Ω for each J value. The explicit representation of this matrix for a given rotational level is given in table 1. Inclusion of hyperfine effects for the first nucleus considered (Cu : I = 3/2) which have selection rules of $\Delta F = 0$, $\Delta F_1 = 0$, $\Delta J = 0$, ±1 increases the matrix size to 12 x 12. The effects due to the second nucleus considered (F : I = 1/2) which have selection rules $\Delta F = 0$, $\Delta F_1 = 0$, ±1, $\Delta J = 0$, ±1 results in a 24 x 24 matrix. The Hamiltonian can be broken down into an 8 x 8 matrix where each 3 x 3 sub-block has a different J or F_1 value, this representation is shown in table 2. The explicit form of the copper hyperfine elements on-diagonal in J is shown in table 3, while table 4 contains the off-diagonal block. The fluorine hyperfine effects were programmed in terms of the 3-j and 6-j symbols in eqn 2.25 rather than the explicit form, due to the complexity of the expressions. The electric quadrupole interaction obeys the selection rule $\Delta F = 0$, $\Delta F_1 = 0$, $\Delta J = 0, \pm1, \pm2$, but the terms off-diagonal in

Table 1. Matrix elements for rotational levels J in a $^3\Pi$ state (Matrix W)

| 0 >	| 1 >	| 2 >
$- A + (B-A_D+2\lambda_D/3)(x+2) + 2\lambda/3 - 2\gamma - D(x^2+6x+4) \mp(o+p+q)$	$- (2x)^{1/2}[B^*-1/2A_D-\lambda_D/3 \mp 1/2(p+2q) - 2D(x+2)]$	$- [x(x-2)]^{1/2}(2D\pm 1/2q)$
	$- 4\lambda/3 + (B-4\lambda_D/3)(x+2) - 2\gamma - D(x^2+8x) \mp 1/2qx$	$- [2(x-2)]^{1/2}[B^*+1/2A_D - \lambda_D/3 - 2Dx]$
		$A + (B+A_D+2\lambda_D/3)(x-2) + 2\lambda/3 - D(x^2-2x)$

$x = J(J+1)$, $B^* = B-1/2\gamma$.

Upper and lower sign choices refer to e and f levels respectively.

Table 2. Block structure for levels with a given F value

F_1 values							
F - 1/2				F + 1/2			
J values							
F - 2	F - 1	F	F + 1	F - 1	F	F + 1	F + 2
W+X+F+Q	$Y+F+Q_1$			Z			
	W+X+F+Q	$Y+F+Q_1$		Z	Z		
		W+X+F+Q	$Y+F+Q_1$	Z	Z	Z	
			W+X+F+Q		Z	Z	Z
				W+X+F+Q	$Y+F+Q_1$		
					W+X+F+Q	$Y+F+Q_1$	
						W+X+F+Q	$Y+F+Q_1$
							W+X+F+Q

The off-diagonal quadrupole elements Q_1, and fluorine hyperfine terms F and Z were not evaluated explicitly.

Table 3. Copper hyperfine terms on-digonal in J (Matrix X)

| 0 >	| 1 >	| 2 >
0	$(b \pm d)(2x)^{1/2}R(F)/(4x)$	0
	a R(F)/(2x)	$b[2(x-2)]^{1/2}R(F)/(4x)$
		2(a+b+c)R(F)/(2x)

R(F) = F(F+1)-J(J+1)-I(I+1).

Upper and lower sign choices refer to e and f levels respectively.

Table 4. Copper hyperfine terms off-diagonal in J (Matrix Y)

	$\lvert J+1, 0 \rangle$	$\lvert J+1, 1 \rangle$	$\lvert J+1, 2 \rangle$
$\lvert J, 0 \rangle$	$-[a-(b+c)]W(F)$ $(J+1)$	$1/2(b \pm d)W(F)$ $[2(J+1)(J+2)]^{1/2}$	0
$\lvert J, 1 \rangle$	$-1/2(b \mp d)W(F)$ $[2J(J+1)]^{1/2}$	$-a\ W(F)$ $[J(J+2)]^{1/2}$	$1/2b\ W(F)$ $[2(J+2)(J+3)]^{1/2}$
$\lvert J, 2 \rangle$	0	$-1/2b\ W(F)$ $[2J(J-1)]^{1/2}$	$-(a+b+c)W(F)$ $[(J-1)(J+3)]^{1/2}$

Upper and lower sign choices refer to e and f levels respectively.

$$W(F) = \left[\frac{(F+I+J+2)(-F+I+J+1)(F-I+J+1)(F+I-J)}{(2J+1)(2J+2)^2(2J+3)}\right]^{1/2}.$$

Table 5. On diagonal electric quadrupole terms (Matrix Q)

$\langle 0 \vert$	$\langle 1 \vert$	$\langle 2 \vert$
$eq_0Q\ T(F)x$	0	0
	$eq_0Q\ T(F)(x-3)$ $\pm 1/6 eq_2Q\ T(F)$ $[J(J+1)(J+2)(J+3)]^{1/2}$	0
		$eq_0Q\ T(F)(x-12)$

Upper and lower sign choices refer to e and f levels respectively.

$$T(F) = \frac{[5x-Y(Y-1)]}{2(2J+3)(2J+2)2J(2J-1)} .$$

$$Y = J(J+1)-F(F+1)+I(I+1) .$$

J by 2 were not included as they were considered to be insignificant. The explicit representation of the other quadrupole terms is given in table 5. For each given F level there are two matrices, one with positive and one with negative parity and in constructing these from the sub-blocks for different J it is necessary to take alternately e and f components for the lambda doubling terms, as the e levels have parity $(-1)^J$ and the f levels parity $-(-1)^J$. The actual energies are obtained by setting up and diagonalising the two 24 x 24 matrices for each F value being considered, the energies are assigned to the appropriate basis functions by examination of the corresponding eigenvector for each one.

$^2\Pi$ and $^2\Delta$ energy levels for CH

The Hamiltonians for case $b_{\beta J}$ $^2\Pi$ and $^2\Delta$ states are very similar and so they can be considered together. Besides those quantum numbers already considered an additional one K, which relates to the projection of **N** onto the internuclear axis, is needed this is equivalent to λ for a diatomic molecule as R is perpendicular to the internuclear axis. The basis set for a case $b_{\beta J}$ molecule with one nuclear spin has the form

$$|\eta\ \lambda;S\ N\ K\ J\ I\ F\rangle \qquad 2.26$$

The case a basis functions are however rather easier to deal with and the appropriate matrix elements have been evaluated (2). The appropriate Wang combinations of case a functions are then

$$2^{-1/2}(|\eta\ \lambda;S\ \Sigma;J\ \Omega;I\ F\rangle \pm (-1)^{J-S}|\eta\ -\lambda;S\ -\Sigma;J\ -\Omega;I\ F\rangle) \qquad 2.27$$

For a $^2\Pi$ state $|\lambda| = 1$ and $S = 1/2$ which gives $\Sigma = -1/2$ or $+1/2$ and thus $|\Omega| = 1/2$ or $3/2$ this leads to two basis states for a given N. For CH $I = 1/2$ and thus if the off diagonal hyperfine terms are included the matrices are of

dimension 4 x 4, one with positive and one with negative parity occurring for each F value. The terms included in the effective Hamiltonian are as follows

$$\mathcal{H}_{eff} = \mathcal{H}_{rot} + \mathcal{H}_{cd} + \mathcal{H}_{cdcd} + \mathcal{H}_{so} + \mathcal{H}_{sr} + \mathcal{H}_{srcd} + \mathcal{H}_{LD}$$
$$+ \mathcal{H}_{LDcd} + \mathcal{H}_{LDcdcd} + \mathcal{H}_{hfs} + \mathcal{H}_{hfscd} \qquad 2.28$$

Although only low N levels were observed the small mass of CH requires the inclusion of several high-order centrifugal distortion terms. This is particularly true of the lambda doubling and lambda-doubling type hyperfine terms, due to the very high precision of the experimental results. Expressions for all of the elements above are given in reference 2.

For a $^2\Delta$ state $|\Lambda| = 2$ and $S = 1/2$ giving $\Sigma = -1/2$ and $+1/2$ and thus $|\Omega| = 3/2$ and $5/2$, the two basis states for a given N, although these are usually written as F_2 and F_1 respectively as Ω is not a good quantum number. The spectra observed, which involve the $^2\Delta$ state were not as precise as those in the $^2\Pi$ state and only the following terms were needed

$$\mathcal{H}_{eff} = \mathcal{H}_{rot} + \mathcal{H}_{cd} + \mathcal{H}_{cdcd} + \mathcal{H}_{so} + \mathcal{H}_{sr} + \mathcal{H}_{srcd} + \mathcal{H}_{LD} + \mathcal{H}_{hfs} \qquad 2.29$$

The same expressions (2) as for the $^2\Pi$ state may be used to evaluate the $^2\Delta$ matrix elements. As the rotational spacing is large in CH it was decided not to include terms off-diagonal in J and thus the matrices were only of dimension 2 x 2, this is shown in table 6.

No expression for $\mathcal{H}_{socd}$, the centrifugal distortion correction to the spin-orbit interaction has been included because for $^2\Pi$ and $^2\Delta$ states the two parameters A_D and γ, the spin-rotation interaction, are not separately determinable. This 100% correlation between the two terms has been shown by Brown and Watson (10), to be due to the actual form of the matrix elements. The only means of separating the terms

Table 6. Matrix representation of the energy levels of a molecule in a $^2\Delta$ state

	| 3/2 >	| 5/2 >
| 3/2 >	$-A-3/2\gamma-\gamma_D(2z+9)+B(z+6)$ $-D[(z+6)^2+z]+H(z^3+21z^2+122z+216)$ $\mp(p+4q)(J+1/2)[z(z+3)]^{1/2}$ $+3\{2a-1/2(b+c)\}R(F)/[4J(J+1)]$	$-\{B-1/2\gamma-1/2\gamma_D(z+5)-2D(J+1/2)^2$ $+H(3z^2+25z+52)\mp 1/2q(J+1/2)(z+3)$ $-bR(F)/[4J(J+1)]\}z^{1/2}$
| 5/2 >		$A+1/2\gamma+\gamma_D+B(z+2)$ $-D(z^2+5z+4)+H(z^3+5z^2+6z+8)$ $+5\{2a+1/2(b+c)\}R(F)/[4J(J+1)]$

Upper and lower sign choices refer to e and f levels respectively.

$z = (J+1/2)^2 - 4$.

$R(F) = F(F+1)-J(J+1)+I(I+1)$.

is by measuring two isotopes eg CH and CD and taking advantage of the different isotope modification effects for γ and A_D. As this has not been done, the values determined in the $^2\Pi$ and $^2\Delta$ states for A and γ are only effective parameters containing contributions from A_D.

References

1. F.Hund, Z. Phys. 36, 657 (1926) and 40 742 (1927).
2. J.M.Brown, M.Kaise, C.M.L.Kerr and D.J.Milton, Mol. Phys. 36, 553-582 (1978).
3. J.M.Brown and A.J.Merer, J. Mol. Spectrosc. 74, 488-494 (1979).
4. J.M.Brown, I.Kopp, C.Malmberg and B.Rydh, Phys. Scrip. 17, 55-67 (1978).
5. J.M.Brown, E.A.Colbourn, J.K.G.Watson and F.D.Wayne, J. Mol. Spectrosc. 74 294-318 (1979).
6. R.S.Mulliken and A.Christy, Phys. Rev. 38, 87-119 (1931).
7. R.A.Frosch and H.M.Foley, Phys.Rev. 88, 1337-1349 (1952).
8. A.R.Edmonds, "Angular Momentum in Quantum Mechanics", Princeton University Press, Princeton, N.J. 1960.
9. J.M.Brown and B.J.Howard, Molec. Phys. 31, 1517 (1976) and 32, 1197 (1976).

Chapter 3 High Resolution Spectroscopic Techniques

3.1 Intermodulated fluorescence

Introduction

While most people would consider the resolution obtainable by laser induced fluorescence, typically 1.5 GHz fairly high, there still remains much structure of interest which could be observed with a narrower linewidth. The limiting factor for observations of this type is the Doppler linewidth and although hyperfine effects can be seen even at this resolution, as will be shown for CuF in Chapter 5, much structure remains hidden. Various saturation techniques have been developed to observe this structure, involving two counter propagating beams of light. The transition becomes saturated when the laser is tuned to the centre of the Doppler profile, and molecules which are stationary with respect to the line of the beams can absorb from both. The fluorescence signal will show a similar decrease to the absorption and the saturation signals may be detected in this way. Any spectra recorded in this manner will consist of small peaks on a large background and clearly much better sensitivity could be obtained if the saturation signals were produced with no background. This can be done by using intermodulated fluorescence which involves amplitude modulation of both beams and detection of signals at the sum frequency of the modulation. This technique was originally developed by Sorem and Schawlow (1), who recorded lines in the I_2 spectrum, using the 514.5 nm line of an argon ion laser. The development of tunable dye lasers with a single frequency linewidth of 1 MHz has made this a much more useful technique. Several other species have been observed by this method some of them in this laboratory and a summary of these is given by Brown et al (2).

Figure 1. Schematic of the arrangement of apparatus for intermodulated fluorescence measurements. The laser is split into two equal beams which are chopped at different frequencies and passed colinearly in opposite directions through the sample. The fluorescence modulated at the sum frequency is detected by a lock-in amplifier. The polarisation rotator and polariser are used to stop the returning beam from re-entering the laser. The 1m confocal etalon acts as a relative frequency calibration for measuring splittings between lines.

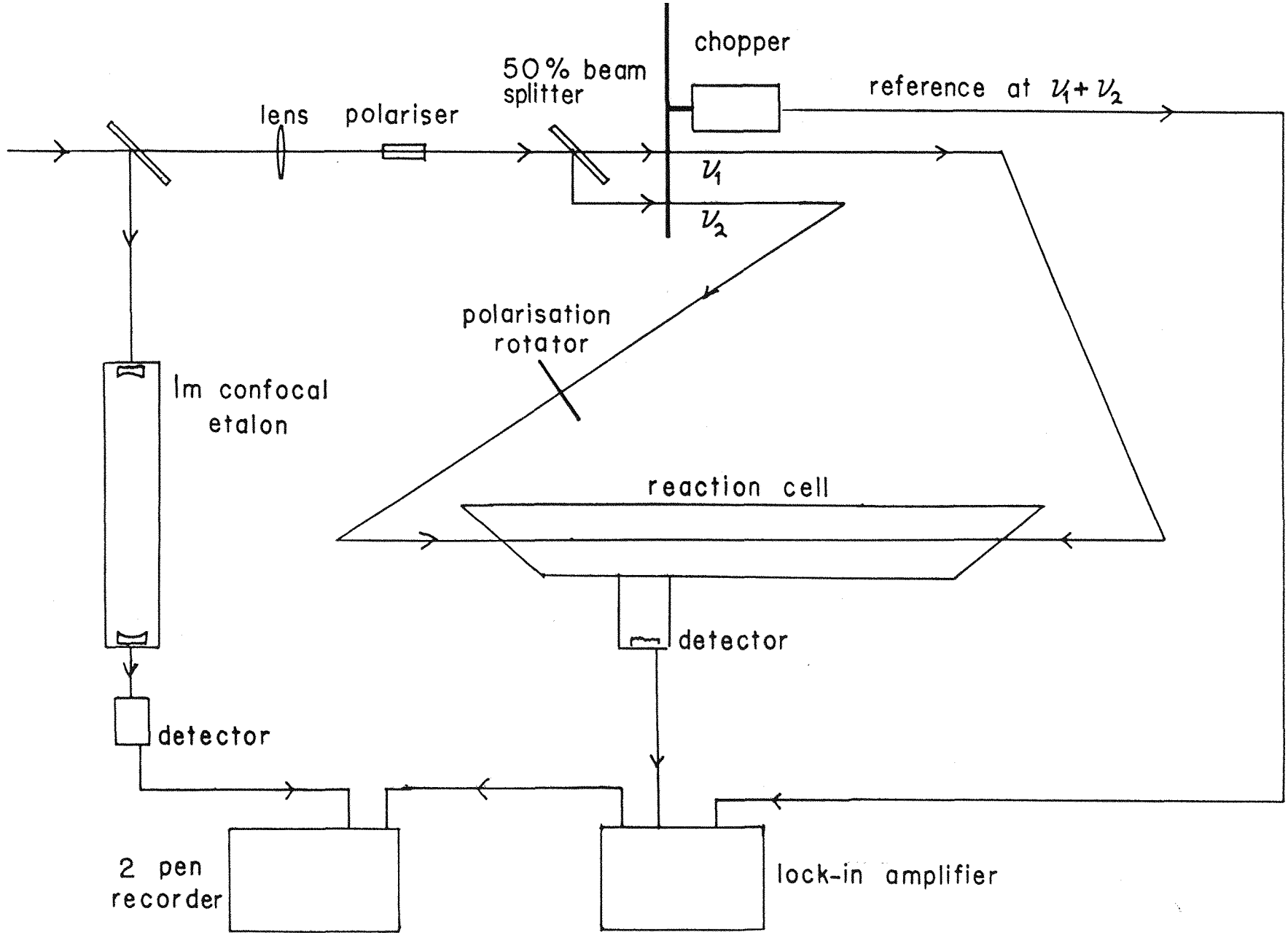
chopper
50% beam splitter
reference at $\nu_1 + \nu_2$
lens
polariser
ν_1
ν_2
polarisation rotator
1m confocal etalon
reaction cell
detector
detector
2 pen recorder
lock-in amplifier

Experimental Procedures

The experimental set-up used for recording signals is shown in figure 1. The laser beam is passed through a dielectric coated beam splitter producing two beams of approximately equal intensity, the angle of the beam splitter being adjusted to make the two intensities as equivalent as possible. Both beams are passed through a mechanical chopper with three sets of holes, the two inner ones are used for the laser beams giving modulation frequencies of 356 and 499 Hz while the outer ring provides a reference signal at the sum frequency 855 Hz. The two beams are focussed and passed colinearly through the apparatus in opposite directions, the beam waists being adjusted to be the same size when actually passing through the region of interaction with the sample. This leads to maximum overlap of the two beams and hence the best signal possible. Feedback of the beam to the laser is eliminated by rotating the plane of polarisation inside the ring of counter-propagating beams and using a plane polariser outside of this to block the returning radiation This allows the positions of the beams to be adjusted so that they lie exactly on top of each other, which leads to stronger signals and the removal of the small residual Doppler linewidth produced when the beams are crossed at an acute angle. The non-linear response of the molcules to the radiation mixes the two frequencies and signals are produced at the sum with zero Doppler linewidth, a photomultiplier tube and tuned lock-in amplifier system being used to record the results. The output from the lock-in amplifier together with the signals at 75.1 MHz intervals from a 1 m thermally stabilised confocal etalon are recorded on a two pen chart-recorder. Facility for recording the signals using a computer also exist.

The linewidths are typically of the order of 30 MHz, a factor of 50 improvement on the Doppler limited signals. Spectra have been observed of CuF and CH in this work with linewidths of 25 and about 30 MHz respectively. The

ultimate limiting factor is the lifetime of the excited state but in both these cases this provides a contribution much smaller than the observed linewidths, these probably being caused by collisional and power broadening effects. The signals seen for CuF probably involve the weakest optical transition so far seen using IMF, $^3\Pi - {}^1\Sigma^+$ which is quite strongly forbidden, the lines seen being only just visible by eye. To record these, an additional slit and lens were added to the detection system which gave an improvement of two orders of magnitude in sensitivity. Lines in SrF observed using the unmodified apparatus (2) with a signal to noise of about 40 were seen with essentially no noise and even the very weak lines in that system could be seen easily. The optical transition for CH $^2\Delta - {}^2\Pi$ is much stronger and lines were observed comparatively easily.

Intermodulated fluorescence is a fairly sensitive technique and could be used for most molecules which give reasonably strong signals when observed using laser induced fluorescence. The minimum signal to noise for LIF signals required for observation of IMF is typically 1000 to 1 but this is likely to depend on other factors such as the upper state lifetime and the change in dipole moment for the optical transition.

3.2 Microwave Optical Double Resonance

Introduction

Another method of observing signals at a much higher resolution than LIF is by microwave spectroscopy. Due to the much lower frequency the Doppler linewidth is only of the order of 100 kHz and frequently is not the limiting factor. Conventional microwave absorption spectroscopy is not as sensitive as LIF and for free radicals it is often hard to obtain a sufficient concentration of the species under investigation. The great sensitivity of fluorescence detection means that , when a suitable optical transition is available, signals which are either very weak or unobservable using conventional microwave absorption spectroscopy, may be seen quite easily with good signal to noise using microwave optical double resonance. The one major disadvantage is that the linewidth is usually limited by the relaxation lifetime for the excited state and is frequently somewhat greater than that obtainable with microwave absorption. Transitions in excited vibrational and electronic states, which usually cannot be observed at all using microwave absorption, may also be recorded using MODR.

This technique of monitoring microwave transitions via changes in fluorescence intensity was used even before the advent of laser excitation, by pumping the appropriate optical line with emission from an atomic discharge tube (3)(4). Since the advent of tunable dye lasers many molecules have been studied using this technique.

Experimental

MODR transitions are observed by tuning the laser radiation to connect with one component of the transition of interest and varying the microwave frequency. The requirement for observing double resonance signals is that, when the microwave transition is resonant there should be a significant change in the level of fluorescence. The actual

Figure 2. Pumping scheme for Microwave Optical Double Resonance experiments. For ground state measurements a laser is used to depopulate level 2, an increase in total fluorescence occurs when the microwave transition is in resonance and repopulates this level. For excited state measurements a laser is used to promote a significant population to level 2. When the microwave transition is tuned into resonance the population in level 2 falls leading to greater absorption of the laser beam and hence an increase in the total fluorescence.

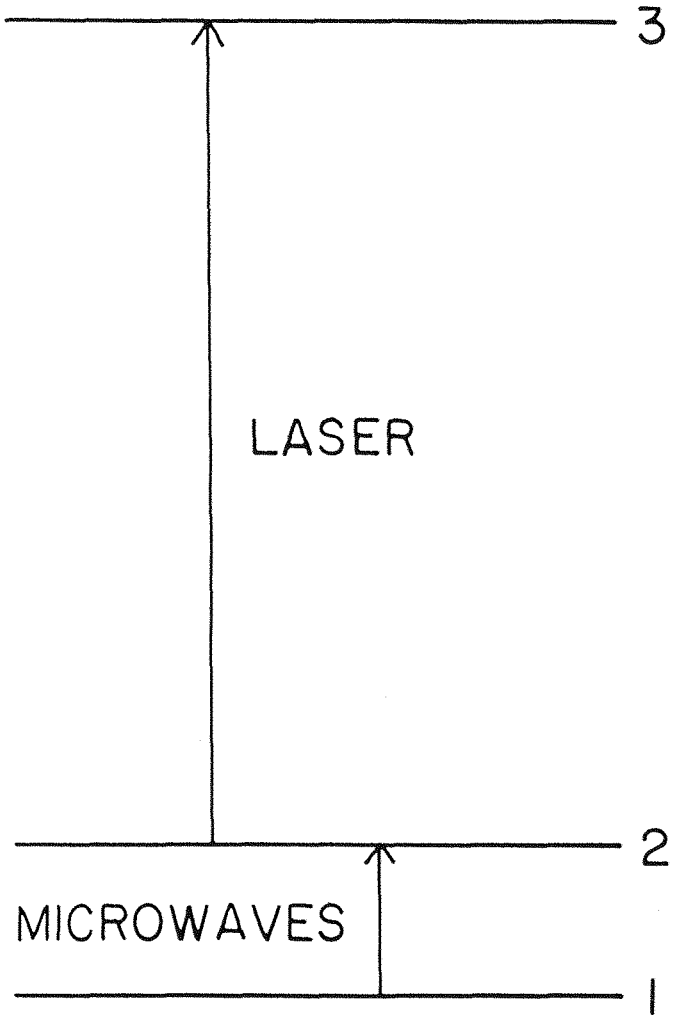

Ground State MODR

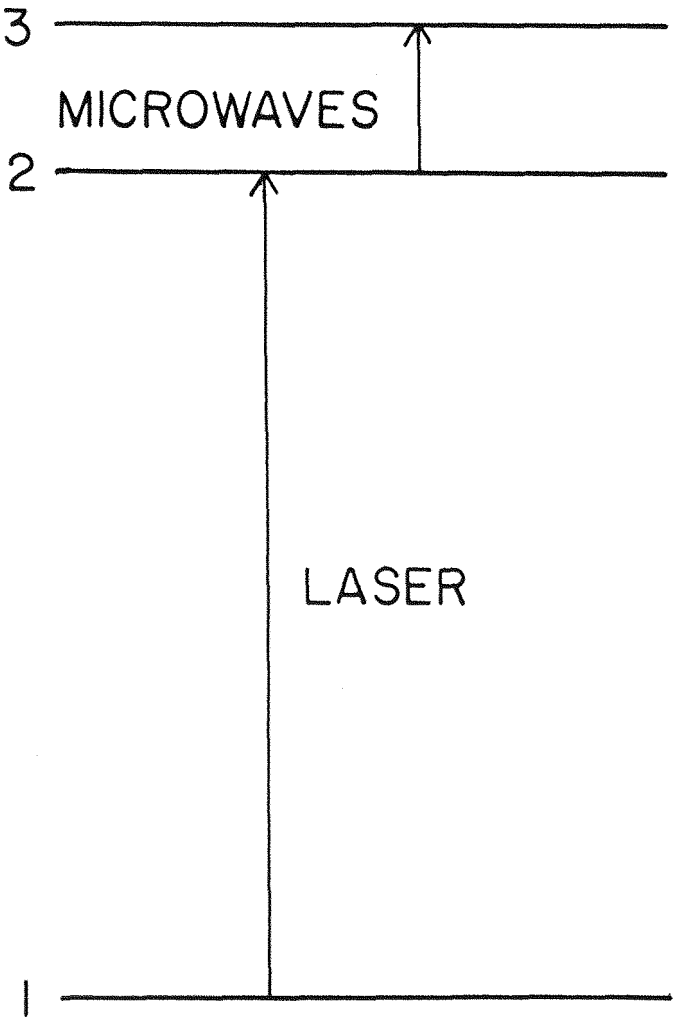

Excited State MODR

amount of change required will clearly be dependent on the signal to noise for the optical transition, if this is very high then only minute, perhaps 1 in 10^5, changes can be detected but for weak optical transitions the change in the fluorescence level must be large. It is possible to observe MODR transitions in both ground and excited electronic states, the pumping schemes for these two cases are shown in figure 2. Ground state MODR transitions are usually quite easy to observe even if the optical transition is weak. When the optical pump originates from level 2 there is already a Boltzmann population difference between levels 1 and 2 which if saturation of the microwave transition is achieved will lead to an increase in fluorescence. If pumping were to originate from level 1 then a decrease in fluorescence could be observed in this case, however MODR signals are frequently not obtainable in this situation. This is the main reason why for ground state MODR it is best to pump from the upper level as it is quite possible for the effect of pumping from level 1 to equalise the distribution in the two levels, in which case no signal would be observed. If the optical pumping is very strong leading to significant depletion from level 2 then MODR transitions may be seen with fairly low microwave powers. This is known as the strong pumping limit and using a dye laser, giving typically 50 mWatts this is the situation normally obtained.

The study of upper state MODR, although this began before ground state (3), is usually more difficult. If the optical pumping transition is weak, then the amount of fluorescence will depend only on the population of level 1 as level 2 will have an insignificant population relative to this. Hence a resonant microwave transition between levels 2 and 3 can make no difference to the total level of fluorescence even if saturation is achieved and no signal may be observed. The only possibility of observing MODR is if the radiative transition from one excited state has a different lifetime to the other, or that collisional effects lead to a significant loss from one of the upper state levels via non-radiative effects. This could lead to either an increase or

decrease in fluorescence depending on which level is effected. Signals involving effects of this type have been seen in the A^2A_1 state of NH_2 (5). Upper state MODR transitions may also be seen with weak pumping by dispersing the resultant fluorescence with a monochrometer, providing that the resolution of this is sufficient for fluorescence only from level 3 to be detected. It is also possible to take advantage of the polarisation of the laser and microwave radiation fields in order to detect signals with only weak pumping. This has been described by Orullinger and Zare (6) and by Field et al(7) who observed signals by this method in BaO. The change in polarisation of the fluorescence when a microwave transition is resonant is dependent on the different number of M_J components in the rotational levels 2 and 3. Thus this form of detection favours low J rotational observations.

If the optical pumping transition is stronger leading to a significant (usually greater than 0.1%) population in the excited state then the transitions are said to be occurring at the strong pumping limit. This is the situation attained for most experiments using dye laser excitation. In this case the rate of optical pumping is dependent on the difference in population between levels 1 and 2 and hence a resonant microwave transition, resulting in a fall in the population of level 2, will lead to an increase in the total fluorescence. Even in the strong pumping limit and with microwave saturation a signal is not always certain to occur because if the rate of repopulation of the ground state by collisional processes is slow relative to relaxation from the excited state then the factor limiting the total fluorescence will be this collisional repopulation and hence the fluorescence intensity will be independent of any microwave transitions between levels 2 and 3. This could clearly be a problem in some systems and the only way around it would be to use the change of polarisation method of detection or else dispersed fluorescence.

Although MODR has been used for several molecules,

there remain many more for which spectra unobtainable with microwave absorption may be recorded due to the very high sensitivity possible with fluorescence detection.

References

1. M.S.Sorem and A.L.Schawlow, Optics. Comm. **5**, 148-151 (1972).
2. J.M.Brown, D.J.Milton and T.C.Steimle, Faraday Disc. RSC, No. 71, Faraday Symposium 71 (1981).
3. K.M.Evenson, J.C.Dunn and H.P.Broida, Phys. Rev. **136**, 1566 (1964).
4. K.German and R.N.Zare, Phys. Rev. Lett. **23**, 1207 (1969).
5. G.W. Hills,C.R.Brazier, J.M.Brown, J.M.Cook and R.F.Curl Jr. J. Chem. Phys. **76**, 240-252 (1982).
6. R.E.Drullinger and R.N.Zare, J. Chem. Phys. **51**, 5532 (1969).
7. R.W.Field, A.D.English, T.Tanaka, D.O.Harris and D.A.Jennings, J. Chem. Phys. **59**, 2191-2203 (1973).

Chapter 4 Least Squares Fitting

In order to satisfactorily fit a large quantity of experimental data, a model with several adjustable parameters is required. To actually derive these constants from the data, a means of varying the parameters and observing whether they lead to a better or worse reproduction of the experimental data is needed. The generally accepted technique for doing this is the least squares method (1)(2).

The essential principal of this method is to minimise the sum of the squares, of the residuals between the observations and the calculated values. Hence the set of residuals r_i is given by

$$r_i = y_i - f_i(\beta_1, \ldots, \beta_m) \quad i = 1, 2, \ldots \qquad 4.1$$

where y_i are the experimental observations and $f_i(x)$ represents the calculated values from the initial set of parameters β_j. For most spectroscopic observations the relationahip between the data and the parameters is non-linear and it is necessary to change this into a linear form by expanding in a Taylor series about the initial values, only the first two terms in the expansion are required. The residuals are then given by equation 4.2

$$r_i = y_i - f_i(\beta_1^{(0)}, \ldots, \beta_m^{(0)}) - \sum_j \frac{\partial f_i}{\partial \beta_j}\Big|_{\beta_j^{(0)}} (\beta_j - \beta_j^{(0)}) \qquad 4.2$$

It is possible to make this expression somewhat simpler by writing the various elements in matrix form

$$r = a - Ad \qquad 4.3$$

where r is the new set of residuals of dimension n x 1, and a the original residuals also n x 1. A is the n x m matrix of derivatives for each point with respect to each parameter while d is the m x 1 set of corrections to the constants.

The requirement of the fit is to find the matrix d which leads to the smallest value for the sum of the squares of the residuals, this is given by 4.4

$$r^2 = \tilde{r}r = (\tilde{a} - \tilde{d}\tilde{A})(a - Ad) \qquad 4.4$$

The smallest value for rr is when the derivative with respect to d is zero ie

$$\partial/\partial d((\tilde{a} - \tilde{d}\tilde{A})(a - Ad)) = 0$$
$$2\tilde{A}Ad - 2\tilde{A}a = 0$$
$$d = (\tilde{A}A)^{-1}\tilde{A}a \qquad 4.5$$

Equation 4.5 shows that in order to obtain the best set of constants all that is required is the matrix of derivatives and the set of initial residuals, simple matrix multiplication giving corrections required to the original constants. The matrices are often quite large involving the fitting of hundreds of points to tens of constants and hence it is necessary to use a computer for the manipulations.

Sometimes different data points are known to different accuracies and a fit with each point weighted according to its measurement precision must be used. The weight matrix W is usually diagonal and consists of the inverse squares of the measurement errors. In some cases where the data points are correlated to each other, off diagonal elements should also be included. These representing the error common to both points in question. Equation 4.4 represents the special case when all the weights are unity, the corresponding general formula is

$$\tilde{r}Wr = (\tilde{a} - \tilde{d}\tilde{A})W(a - Ad) \qquad 4.6$$

Following the same procedure as before gives

$$d = (\tilde{A}WA)^{-1}\tilde{A}Wa \qquad 4.7$$

and hence the changes to the parameters may be evaluated.

The derivative matrix can be obtained by two methods. The simpler of these involves making a small change in the parameter in question, typically 1 in 10^5 and then recalculating the frequencies for each observation. The derivative is simply the change in frequency divided by the change in parameter. However this method involves setting up and diagonalising the full set of energy matrices for each parameter to be varied and results in a prohibitively high run-time when a large number of parameters are involved. An added disadvantage is that the initial value for a parameter can not be taken as zero. The second method uses the Hellmann-Feynman theorem

$$(\partial E/\partial \beta) = \langle \partial \mathcal{H}/\partial \beta \rangle \qquad 4.8$$

That is the derivative of the energy with respect to a parameter is equal to the expectation value, of the derivative of the Hamiltonian with respect to that parameter, taken over the appropriate wavefunction. If the Hamiltonian contains only diagonal elements then the expectation value is simply the derivative, but in most cases the basis states are mixed together by off-diagonal elements and it is necessary to average over all of the states contributing to a particular energy level. The appropriate coefficients are contained in the eigenvectotr matrix obtained from the diagonalisation of the energy matrix and hence pre- and post-multiplying the derivative of the Hamiltonian by this will give the expectation values of the derivatives.

If the set of parameters, to be varied, has been correctly selected and sufficient data are available to determine all of them, the process described above will lead to an improvement in the quality of reproduction of the data. Usually only two or three cycles are required before no further improvement is produced, and the best fit constants obtained. Provided that the matrix of weights has been formulated in terms of the actual estimated experimental errors then the standard deviation of fit $\tilde{r}Wr/(n-m)$

where n-m is the number of degrees of freedom should be close to 1. If it is significantly larger, say about 2 then clearly some of the data is not fitted correctly, while if it is significantly smaller, say about 0.5, then the parameters have been over-determined, possibly by allowing too many to vary. An estimate of the precision with which each parameter is determined is also required, this is given by the variance-covariance matrix

$$V = \{\tilde{r}Wr/(n-m)\}(\tilde{A}WA)^{-1} \qquad 4.9$$

where the first term is the standard deviation of fit described above, and the second is the dispersion matrix. The leading diagonal of V contains the estimated variances for the parameters, the errors being the square roots of these terms. The off-diagonal elements are the covariances which provide a measure of how the error in one parameter is related to that in each of the others. These terms are not particularly easy to understand and they are usually normalised to give the correlation matrix C the elements of which are given by

$$c_{ij} = v_{ij}(v_{ii}v_{jj})^{-1/2} \qquad 4.10$$

The correlation matrix provides a ready guide as to how the error in each parameter is related to the errors in all the others, a coefficient close to ±1 implying a high degree of correlation and one close to 0 a very low degree. The confidence limits of the parameters obtained, usually 95%, are equal to about twice the estimated error, provided the number of degrees of freedom is large. However if the correlation coefficients are large then it is possible for some of the parameters to be out by rather more than would usually be expected if the ones with which they are correlated are also in error.

References

1. D.L.Albritton, A.L.Schmeltekopf and R.N.Zare, 'Molecular Spectroscopy: Modern Research' (K. Narahari Rao, Ed.), Vol II, pp.1-67, Academic Press, New York, 1976.
2. R.F. Curl Jr. J. Comp. Phys. 6, 367-377 (1970).

CHAPTER 5 THE YELLOW SYSTEM OF CuF

5.1 Introduction

The first rotational analysis of the various bands in the visible spectrum of CuF was attempted by Woods (1) in 1943, using spectra obtained in emission from a hollow-cathode discharge source. However a full analysis of the three bands observed at 570 nm, 506 nm and 492 nm was not possible due to the complexity of the systems. The positions of the low lying states of CuF, so far discovered, are shown in figure 1. There was little further interest until a kinetic study by Johnson et al (2) into the chemilumen-escence from the reaction of several fluorine-containing compounds with copper atoms. They showed that this was due to CuF. Steele and Broida (3) investigated the same reactions as well as the products which occur from heating CuF_2 and measured radiative lifetimes and photon yields. They also remeasured and analysed the $A^1\Sigma^+-X^1\Sigma^+$ system at 506 nm. A molecular beam study of the reaction between copper atoms and F , carried out by Schwenz and Parson (4) gave values for the relative rates of formation of the various excited states of CuF.

The most important general spectroscopic study has been performed by Ahmed et al (5) using a grating spectrograph. They observed five band systems, the three previously mentioned and two new ones, also seen by Steele and Broida, at 685 nm and 440 nm. From their analysis they were able to assign the 492 nm band as $B^1\Pi-X^1\Sigma^+$, the 440 nm band as $c^3\Delta-X^1\Sigma^+$ and the 685 nm band as $a^3\Sigma^+-X^1\Sigma^+$.

They were not able however to assign the 570 nm, yellow system definitively, and it was this deficiency which prompted the present study. The observed yellow system consisted of two sub-bands which were clearly due to transitions between the ground $X^1\Sigma^+$ state and two excited state levels characterised by $\Omega = 0^+$ and 1. Ahmed et al chose to assign this to a 'p-complex'. If the copper and fluorine nuclei are considered as being united in a single

Figure 1. Low lying electronic states of copper monofuoride. The ground state is mainly Cu^+F^-, the Cu^+ having a $3d^{10}4s^0$ configuration. The six excited states shown arise from promotion of an electron from the 3d to the 4s orbital. The spins of the unpaired electrons can be either parallel or antiparallel giving rise to singlets and triplets. The d orbital is split into δ, π and σ components in the cylindrical symmetry of CuF giving rise to Δ, Π and Σ electronic states. The positions of the so far unobserved sub-states (shown as dashed lines) are from the work of Schamps et al. (8). The energies of the A, B and c states are from Ahmed et al. (5).

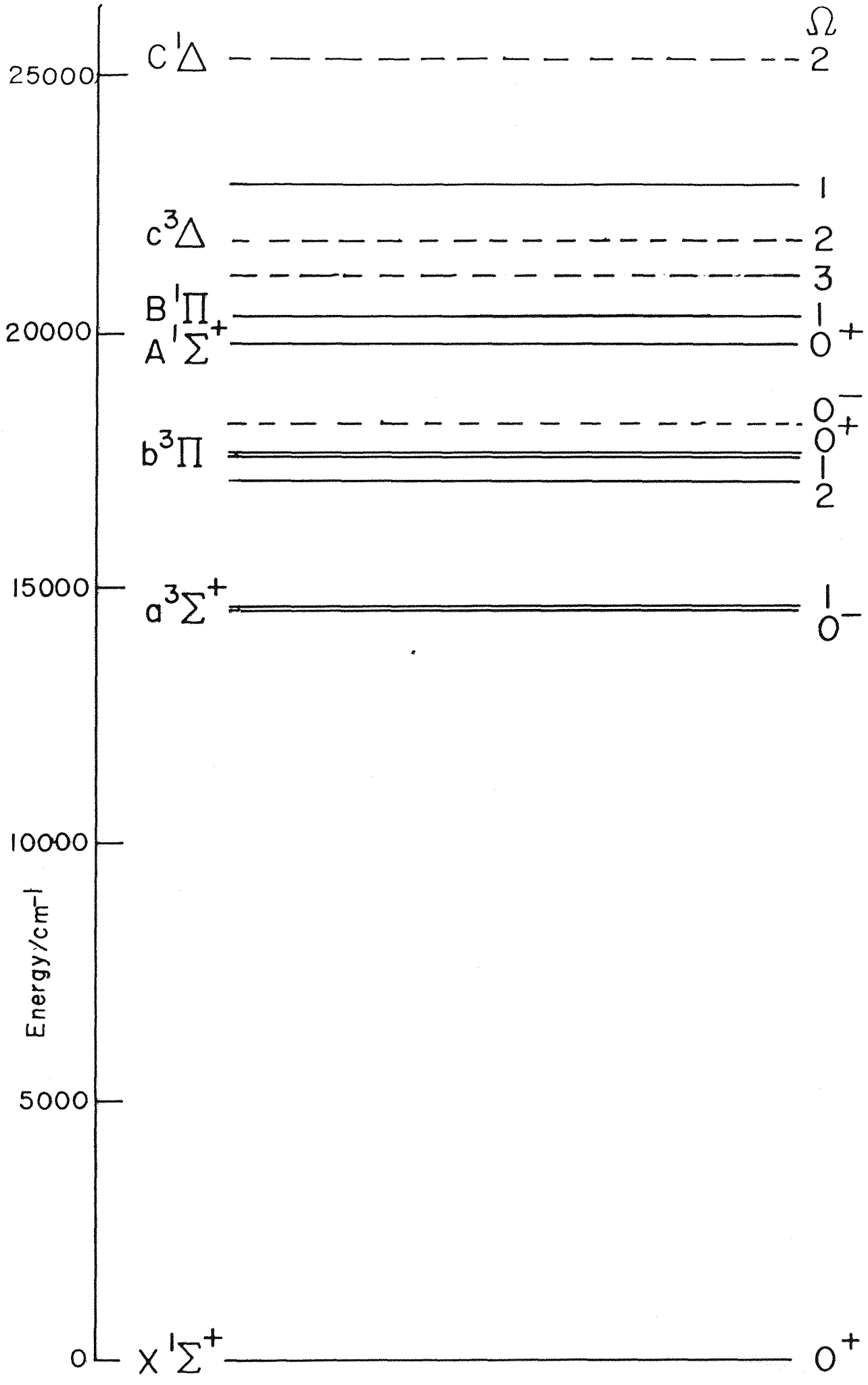
Ω
25000
20000
15000
10000
5000
0
Energy/cm⁻¹
C ¹Δ
2
1
c ³Δ
2
3
B ¹Π
1
A ¹Σ⁺
0⁺
0⁻
b ³Π
0⁺
1
2
a ³Σ⁺
1
0⁻
X ¹Σ⁺
0⁺

atom, then the effect of drawing out the fluorine nucleus to form CuF will be to perturb the atomic energy levels. In particular the ^1P state will give rise to a $^1\Pi$ and a $^1\Sigma^+$ state, thus the term 'p complex' to describe these levels when they remain sufficiently close together to interact. However, the two sub-states could equally as well be interpreted as a $^3\Sigma^-$ state with a large spin-spin splitting, the separation between the two components being about 55 cm^{-1}.

Ahmed et al (5) observed some evidence of hyperfine structure in the red system of CuF; this has since been more extensively analysed in this laboratory (6). It was hoped that observation of similar hyperfine structure in the yellow system at the improved resolution possible in our experiments would result in a conclusive identification of the excited state. The various hyperfine effects, which arise from unpaired electrons, may be interpreted in terms of the possible electronic configurations involved in the state in question. If several assignments are being considered then it is possible that only one will have the correct electronic configuration to explain the hyperfine parameters.

Our first experiments using laser induced fluorescence resulted in the detection of hyperfine structure due to the copper nucleus (I=3/2) at Doppler limited resolution (FWHM = 1.02 GHz). This consisted of partially resolved quartets at high J (>20) in the branches associated with the 0^+ and 1^+ sub-levels. Upon analysis of the hyperfine splittings it was realised that the isomorphism between the 'p-complex' and $^3\Sigma^-$ models for the excited state extended to the hyperfine effects (7). Interpretation of the hyperfine parameters in terms of unpaired spin density on the copper atom gave values reasonably consistent with either of the two models.

In order to obtain information on hyperfine structure in the levels which showed no effects at Doppler-limited linewidth, two experiments of much greater resolution were undertaken, these were intermodulated fluorescence (IMF) and microwave optical double resonance (MODR) which were

described in Chapter 3. The reduced linewidth obtained using IMF (FWHM = 0.025 GHz) meant that each of the four peaks in those branches previously showing copper structure could be seen to be split into doublets by the fluorine (I=1/2) hyperfine interaction. Transitions to the 1^- sub-level which previously showed no structure were now found to be split into quartets by the copper nucleus, the fluorine structure was too small to be resolved.

This structure was unusual however as there was a strong asymmetry in the splittings between the four components. All the features observed except for this were adequately reproduced by the $^3\Sigma^-$ model and hence the isomorphic 'p-complex' model. Many attempts were made to obtain splittings of this type with the $^3\Sigma^-$ model, these included copper quadrupole and nuclear spin rotation interactions but no asymmetry could be produced. Without these inexplicable observations the present chapter could well be about the $b^3\Sigma^-$ state of CuF, but at this stage we began to doubt the $^3\Sigma^-$ (and thus 'p-complex') assignment and this feeling was strengthened when we learned of theoretical calculations by Schamps (8) which suggested that the observed yellow bands might involve a $^3\Pi$ upper state. In order to test this possibility, the rotational frequencies were fitted as subbands of a $^3\Pi-^1\Sigma^+$ transition with the origins of the unobserved $^3\Pi_2$ and $^3\Pi_0$- subbands fixed at the values predicted by Schamps. The quality of fit was found to be essentially the same as for the $^3\Sigma^--^1\Sigma^+$ assignment, and furthermore we were able to reproduce the relative intensities of the different branches with a second order perturbation treatment which involved two independent transition moments (9) (10). Schamps' calculations (8) had predicted that the $^3\Pi_2$ component was 17200 cm^{-1} above the ground state some 350 cm^{-1} below the $^3\Pi_1$ component. Our intensity calculation also allowed us to predict the relative intensities of lines in the $^3\Pi_2$ subband. It suggested that if the subband was within 600 cm^{-1} of the observed system (ie above 17000 cm^{-1}) it should be observable. A search of the region between 17000 and

17500 cm^{-1} was made and the $^3\Pi_2$ subband was eventually found with an origin at 17105 cm^{-1} (11).

Observation of this subband resulted in conclusive identification of the upper state as $b^3\Pi$ although it did not immediately solve the problem of the asymmetric hyperfine structure which originally led us to consider this assignment. The magnetic hyperfine effects still gave essentially symmetric splittings but now there was in addition a lambda-doubling type quadrupole interaction eq_2Q which was found to be responsible for the asymmetry, providing additional proof for the new excited state assignment.

The remainder of this chapter consists of a description of the experimental procedures, a summary of the results obtained, the reduction of these results to a set of effective Hamiltonian parameters, and an analysis of those parameters in terms of the possible electronic configurations involved in the excited state.

Figure 2. The Broida type oven for production of high temperature molecules. The sample is electrically heated in a graphite crucible and the vapour swept into the region of interaction by argon. A laser beam is passed through the vapour and the resultant fluorescence detected in a perpendicular direction, out of the page, via a slit, lens and filter arrangement, by a photomultiplier tube (not shown). For MODR measurements the microwave radiation is admitted through a piece of waveguide from the opposite side of the oven to the detector, ie from below the page.

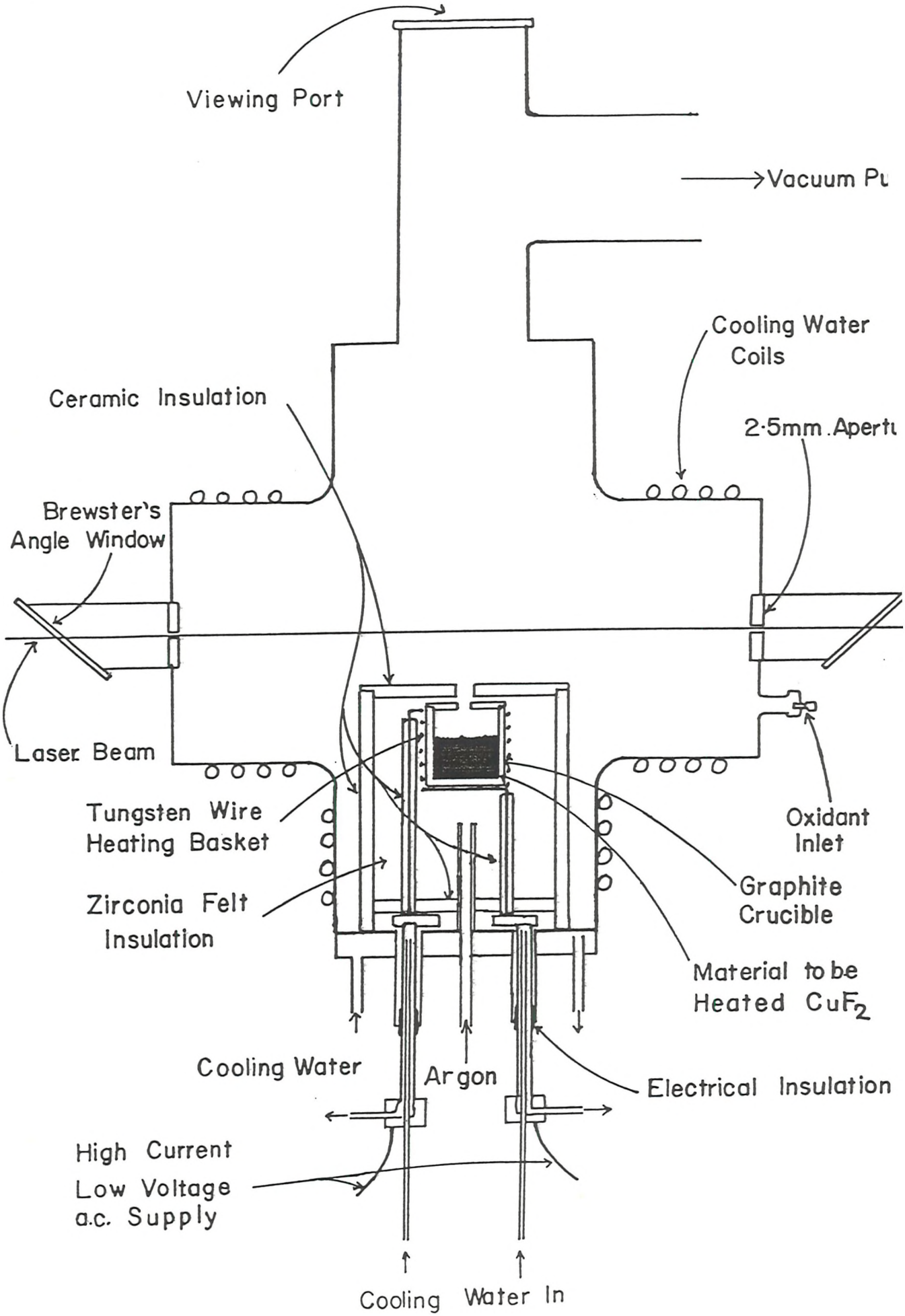
Viewing Port
Vacuum Pu
Cooling Water Coils
Ceramic Insulation
2·5mm. Apertu
Brewster's Angle Window
Laser Beam
Tungsten Wire Heating Basket
Zirconia Felt Insulation
Oxidant Inlet
Graphite Crucible
Material to be Heated CuF_2
Cooling Water
Argon
Electrical Insulation
High Current Low Voltage a.c. Supply
Cooling Water In

5.2 Experimental Details

When copper difluoride is heated to temperatures of around 1000K or greater it produces a vapour which consists to a large extent of copper monofluoride. In each of the experiments the difluoride compound was resistively heated in a flowing gas furnace apparatus of the Broida design (12). A cut away view of the oven is shown in figure 2, the basic structure consists of a 10cm diameter stainless steel cross. The base section contains the actual furnace which is made up of a graphite crucible sitting in a tungsten heating basket. This is surrounded by either graphite or zirconia felt for insulation and finally a ceramic tube and lid which keeps everything in place and provides added insulation. Electrical power for the element is provided via two water cooled electrodes which pass into the oven in insulating nylon sleeves, these are connected to a low voltage transformer and variac adjustable ac supply. Argon gas is passed through the furnace and sweeps the effluent vapour out through a small hole in the top of the cover and into the region of interaction.

The side arms of the cross contain glass windows at Brewster's angle through which either one or two laser beams can be passed, 2.5 mm diameter irises are placed just inside of the windows to reduce the amount of scattered laser light in the cell to a minimum. The oven is pumped out through the top via a particle filter, this section also contains a window through which the interior of the heated cubicle can be observed. Two additional ports are situated on the faces of the cross. Through one microwave radiation is admitted to the oven via a section of waveguide, sometimes with a horn attached where this is physically possible. Opposite to this is the fluorescence detection system which consists of a collimating slit, lens and band-pass interference filter, which for CuF was centred at 555 nm with a 50 nm bandwidth. These were arranged in such a way as to focus the laser induced fluorescence from where the laser beam passed through the sample, onto the photomultiplier tube.

To produce the CuF vapour efficiently, the difluoride powder had to be dry and it was also necessary to heat it fairly slowly in order to fuse it into a solid mass. The best signals were obtained just before solid matter began to shoot out of the crucible and, for weak signals, it was always a problem to keep the level of heating as close as possible to this point. The total pressure in the oven was maintained at about 400 mTorr for the LIF and IMF measurements, however the MODR signals were found to be very sensitive to collisional relaxation and the optimum pressure was determined to be ~150 mTorr. Thermal dissociation was used as the production scheme rather than the reaction of metal vapour with fluorine, or a fluorine-containing compound because a lower pressure could be maintained and the background signal from chemilumenescence was eliminated.

The radiation source was a Coherent Radiation 599-21 standing wave dye laser pumped with 3.5 Watts of the 514.5 nm line of a Spectra-Physics 170 Argon ion laser. For most measurements, Rhodamine 110 dye was used. The exception being those involving the $^3\Pi_2$ sub-band which were covered by Rhodamine 6G. In both cases R6G dye-laser mirrors were used and this was probably the cause of the moderately low 60 - 90 mWatts of single mode output obtained from R110. Using R6G about 150 - 200 mWatts were produced. The output is scannable over a range of 30 GHz (~1 cm^{-1}), before readjustment is necessary and has a linewidth of about 1 MHz. This makes it ideal for most of the experiments performed where the scans are fairly short and the resolution possible quite high (~10 MHz).

For LIF and IMF measurements the laser radiation was amplitude modulated at about 900 Hz and a tuned lock-in amplifier used to analyse the signal from the photomultiplier tube. This results in much improved signal to noise as signals from unmodulated sources in this case primarily background radiation from the oven, are much reduced relative to those which are modulated. Though it was still necessary to align the laser-beam carefully through the oven in order to reduce the amount of scattered laser light

reaching the detector to a minimum. A description of the special modulation scheme used in IMF measurements was given in Chapter 3.

Absolute frequency calibration was provided by simultaneously recording the laser induced fluorescence spectrum of iodine. This could then be compared with the published atlas (13) to obtain the line positions. It was necessary to assume linearity of the laser scan, but as the measured iodine lines are fairly close together, about 4.5 lines per cm^{-1} on average, no large interpolations or extrapolations were required. All results quoted here include the small correction to the absolute frequencies given in the atlas (14). The size of observed splittings in both LIF and IMF lines was determined by simultaneously monitoring the transmission of a 1 m thermally stabilised confocal etalon with a finesse of about 65, which yielded markers at 75.1 MHz intervals. A description of the calibration of the etalon is given in the next chapter.

Microwave optical double resonance (MODR) experiments were performed in three different microwave frequency regions. Microwave radiation was passed along metal waveguide, which allows only a narrow band of frequencies to pass efficiently. All three experiments involved electric dipole allowed transitions in the $b^3\Pi$ state of CuF. The first at about 23 GHz was the $J = 1 \leftarrow 0$ rotational transition which occurs only for the $\Omega = 0$ component as J values less than $|\Omega|$ are not allowed. As no transitions to the $^3\Pi_0$- subband were observed, it was clearly not possible to perform measurements on the $\Omega = 0^-$ levels. Even when this branch is found it is unlikely that transitions to the lowest rotational levels will be of sufficient intensity for MODR, as the forbidden $0^- \leftarrow 0^+$ transition gains intensity only by rotational mixing, which increases rapidly with J. For the $^3\Pi_{0^+}$ transition the power was supplied by a Hewlett-Packard Backward wave oscillator (BWO) HP8696A in an H-P sweeper unit. The quoted power for this source is >10 mWatts, but we have no means of determining the absolute power level, only relative powers over the scan range of a

given source. The next rotational transition J = 2←1 at 46 GHz was also examined, this occurs for both $|\Omega|$ = 0 & 1, and hence it was hoped that valuable information on the lowest levels of the $|\Omega|$ = 1 sub-band would be obtained. In this case the microwave radiation source was a klystron Oki 47V12 powered by an Oki KS-7 klystron power supply. The power obtainable was rather higher in this case ~200 mWatts but this was offset by the problems involved in adjusting the klystron frequency and also in scanning the frequency. Searching a given range with a BWO is trivial as it merely involves setting that range on a scale and using an inbuilt voltage sweep. Once the approximate klystron frequency had been obtained by successive adjustments of the various controls, it was then necessary to scan it. This is most easily done by applying a sweep voltage to the reflector on the klystron via a high voltage isolator. However, this was not possible in this case, and it was necessary to adjust the fine manual control in order to scan the klystron. Fairly linear sweeps were obtained by fitting a 'slow-synch' low-geared driving motor to this control, by means of a coupling which could slip at the ends of the range. Although this proved satisfactory when the transitions being searched for were well predicted, searching over a wider region was more difficult.

The final microwave experiment involved a lambda doubling transition in the Ω = 1 component for J=7 at about 16 GHz the source used was a BWO HP8695A, but at this frequency a Hughes 1177H travelling wave tube amplifier (TWTA) was available which yielded powers of upto 10 Watts.

In each experiment measurements were made by adjusting the laser to a transition connecting to one of the excited state levels, usually the lower one and sweeping the microwave frequency. Amplitude modulation of the microwaves was used and the total undispersed fluorescence, at this modulation frequency, monitored using a tuned lock-in amplifier. Previously measured ground state transitions (15,16) were used to set up the conditions correctly for the excited state measurements at 23 GHz and 46 GHz. Accurate

Figure 3. Schematic of the arrangement of microwave equipment for MODR measurements. The radiation of interest is amplitude modulated and passed into the cell, the resultant change in fluorescence intensity modulated at this frequency is detected by a lock-in amplifier. A small portion of the radiation is mixed with a harmonic of a stabilised reference frequency and the difference frequency detected to give absolute and relative frequency calibration as the microwave source is swept.

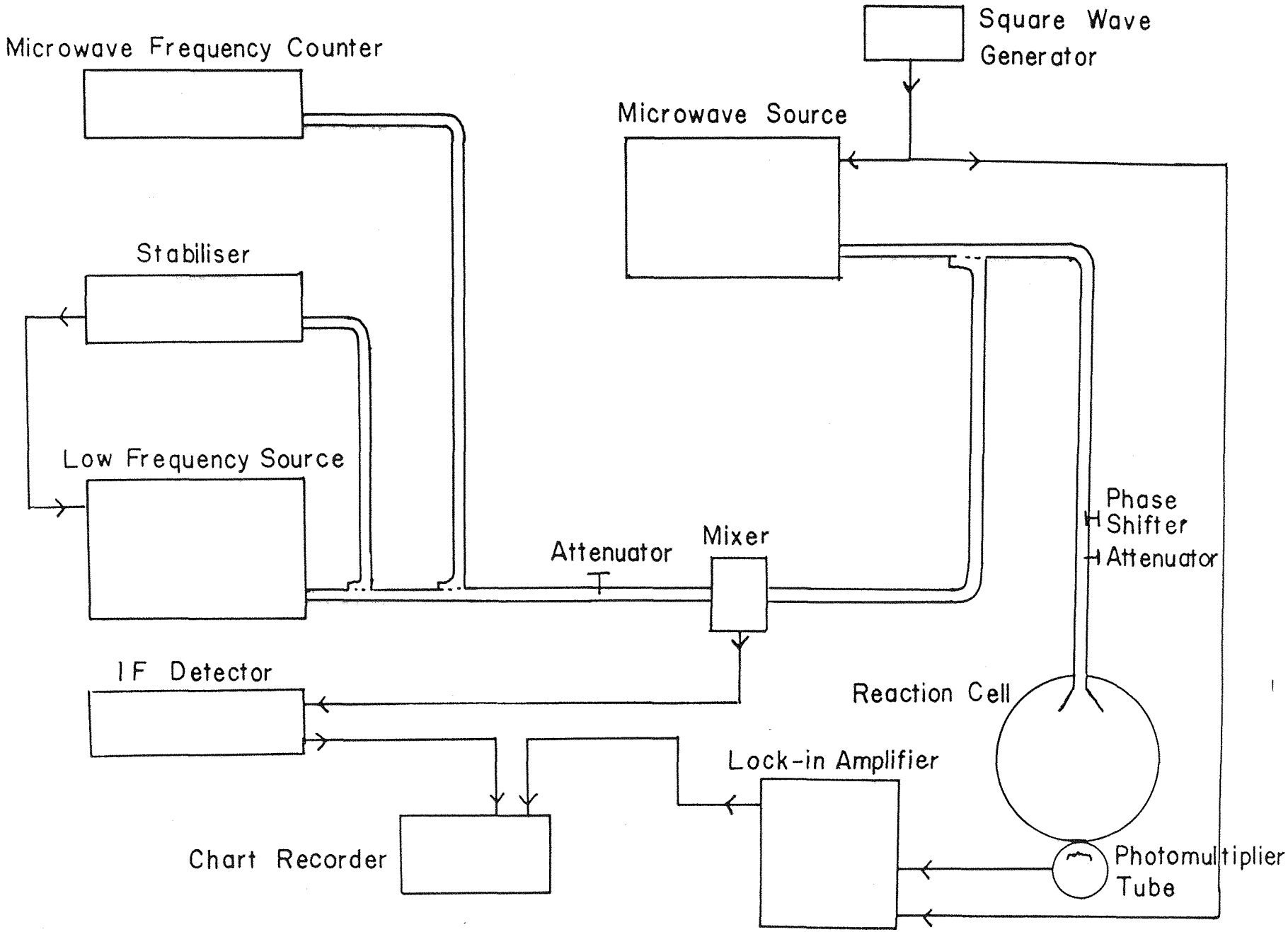
Microwave Frequency Counter
Square Wave Generator
Microwave Source
Stabiliser
Low Frequency Source
Attenuator
Mixer
Phase Shifter
Attenuator
IF Detector
Reaction Cell
Lock-in Amplifier
Chart Recorder
Photomultiplier Tube

values for the frequencies of the various microwave transitions observed, were determined by mixing a portion of the swept radiation with a fixed and stabilised reference frequency at some integer fraction of the main signal. A typical set up for this type of measurement is shown in figure 3. Beat signals from the frequency mixer were picked up by a 30 MHz amplifier-detector, Microwave Systems Model PLS-30, and the signals plotted out simultaneously with the MODR spectrum. Thus on a scan of greater than 60 MHz two markers would be obtained separated by 60 MHz with the centre frequency measured very accurately (ie. to the nearest kiloHertz) by means of an HP5245L counter with 5256A frequency converter plug-in. However, it was frequently not possible to obtain a 60 MHz scan using the klystron, but fortunately careful adjustment of the mixing set-up resulted in further beat signals from higher order mixings appearing 15 MHz from the centre and also 10 MHz et cetera, making measurement of very short scans possible, provided care was taken in deciding which beat signals were being observed.

Figure 4. Splitting of the v=0 levels of the components of the $b^3\Pi$ state of CuF, due to spin-orbit coupling, and mixing with other near-by states. The $\Omega=0^-$ component, which has not yet been seen, is shown by a dashed line in the position predicted by Schamps et al. (8). The energy scale is in cm^{-1} relative to v=0 of the $X^1\Sigma^+$ state.

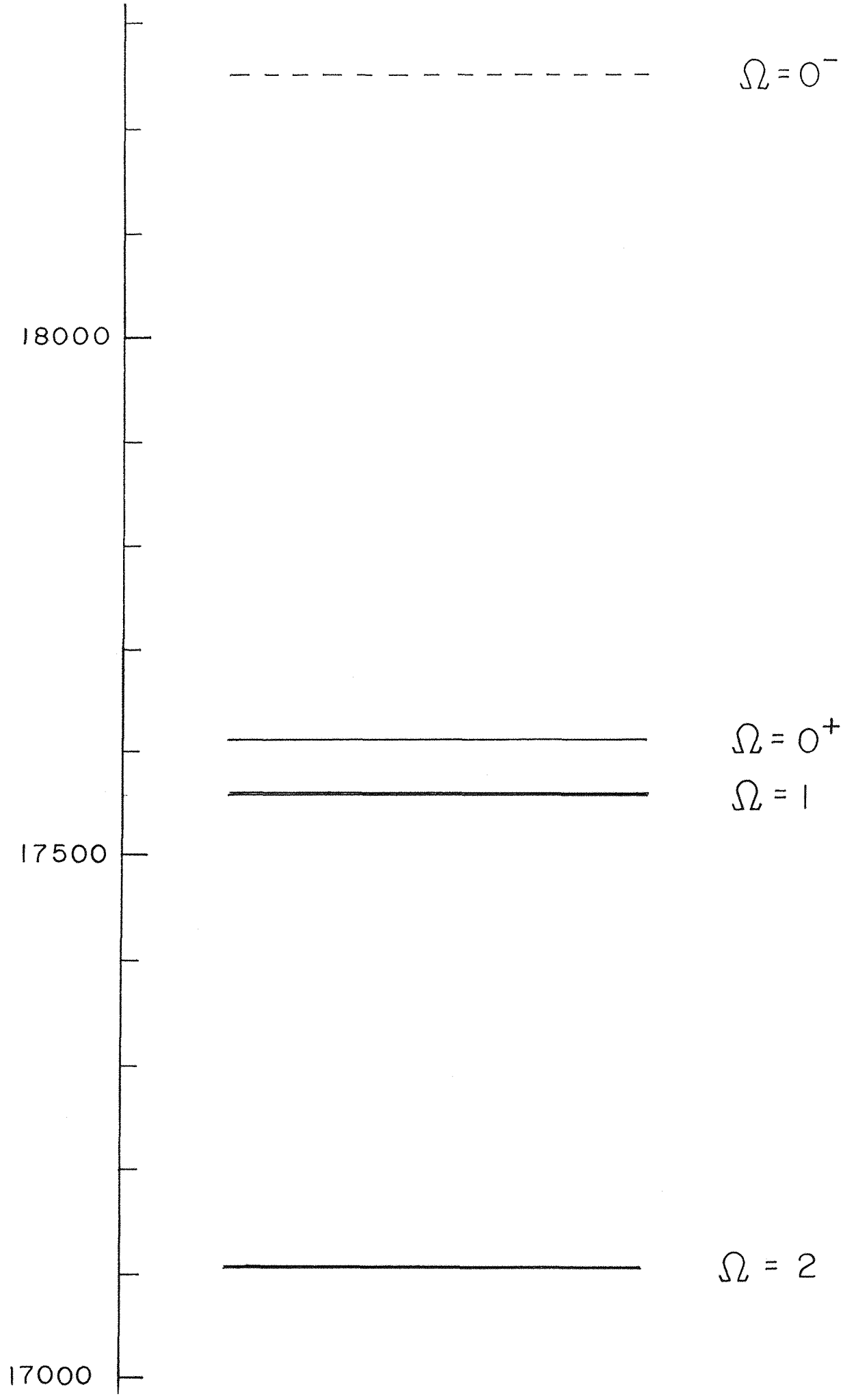
18000
17500
17000
Ω = 0⁻
Ω = 0⁺
Ω = 1
Ω = 2

5.3 Observations

Laser Induced Fluorescence

The $b^3\Pi - X^1\Sigma^+$ system of CuF consists of four sub-bands, the positions of which, for the $v' = 0$ vibrational levels relative to the $v'' = 0$ level are shown in figure 4. Our initial measurements involved transitions to the $\Omega = 0^+$ and 1 only. Identification of the lines was easy as they had already been seen at quite high resolution by Ahmed et al (5). There are two copper isotopes ^{63}Cu and ^{65}Cu which have natural abundances of 70% and 30% respectively, however only transitions involving ^{63}CuF were recorded and similarly only the (0,0) vibrational band was measured although both (1,1) and (2,2) transitions were observed.

These first measurements consisted of P and R branches to the $^3\Pi_{0^+}$ component and P,Q and R branches to the $^3\Pi_1$ component. The resolution of these recordings was an improvement over that achieved in previous work, being limited by the Doppler effect (FWHM = 1.02 GHz). The majority of rotational lines show a partially resolved quartet structure, due to the Cu (I=3/2) nuclear hyperfine splitting. The characteristics of the hyperfine structure are as follows. No significant broadening or splitting is observable for low J in any of the five branches. The lines in the Q branch remain narrow as J increases but the P and R branch lines first broaden (about J=15) and eventually split ($J \approx 30$) into four partially resolved conponents. The maximum level of splitting is reached at about J=50 and observation of some very high J lines ($J \geq 90$) shows that there is no further increase. An example of this hyperfine structure for a typical line where the splitting is close to its limiting value is shown in figure 5.

The signal to noise for most of the lines observed was at best about 100 to 1. This rather poor value is due to the measurements having been made before a slit and lens were added to improve the detection system which has resulted in an approximate 100 fold improvement in the

Figure 5. Partially resolved hyperfine structure on the $P_1(55)$ line in the (0,0) band of the $b^3\Pi - X^1\Sigma^+$ system of CuF. The structure is interpreted as arising from hyperfine interactions involving the ^{63}Cu nucleus (I=3/2).

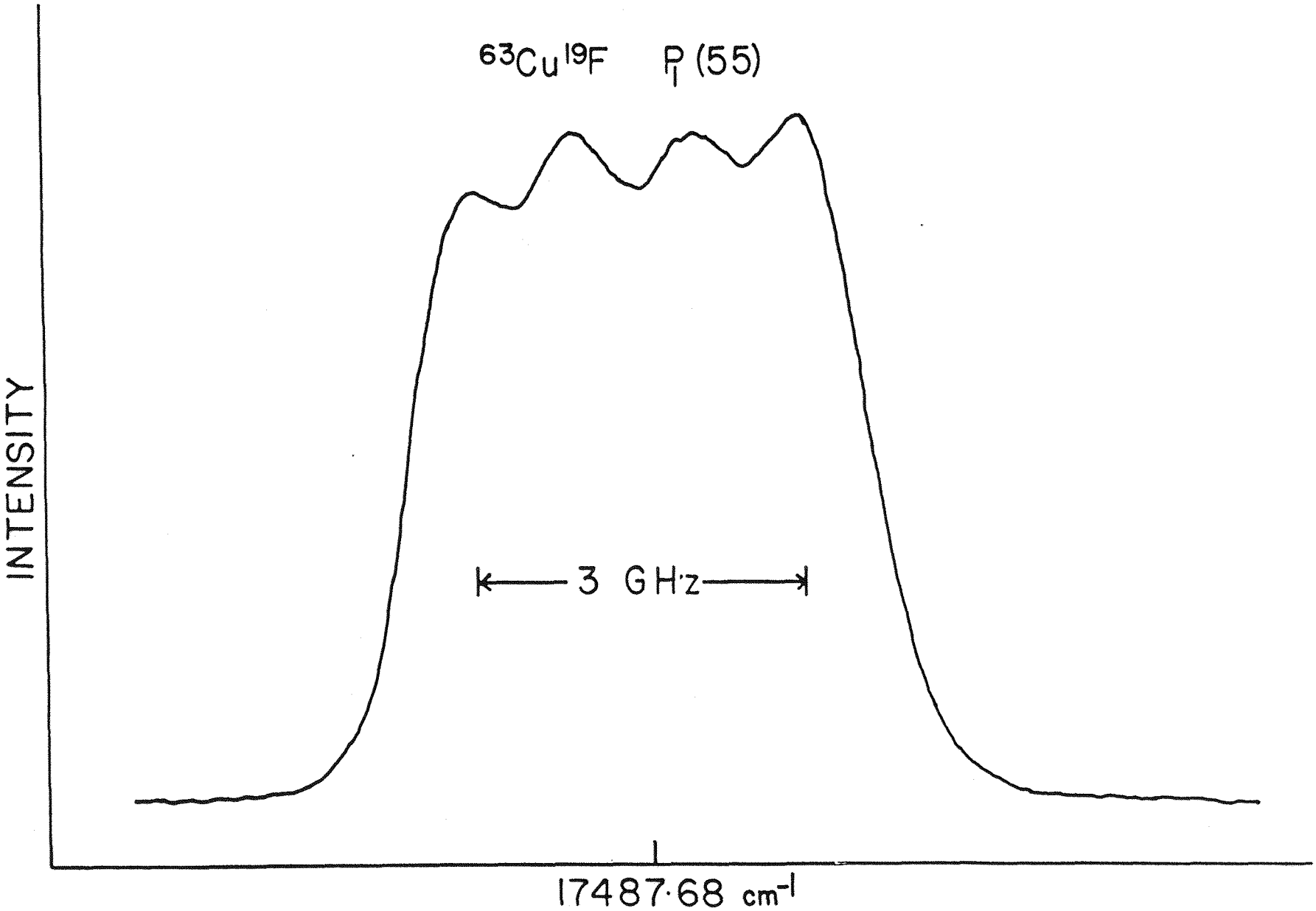
$^{63}Cu^{19}F$ $P_1(55)$
INTENSITY
3 GHz
17487·68 cm^{-1}

Figure 6. Part of the Q branch of the $b^3\Pi_2 - X^1\Sigma^+$ sub-band of ^{63}CuF. The diagram is a composite of five experimentally recorded sections. The J values involved in the transitions are shown above the spectral lines.

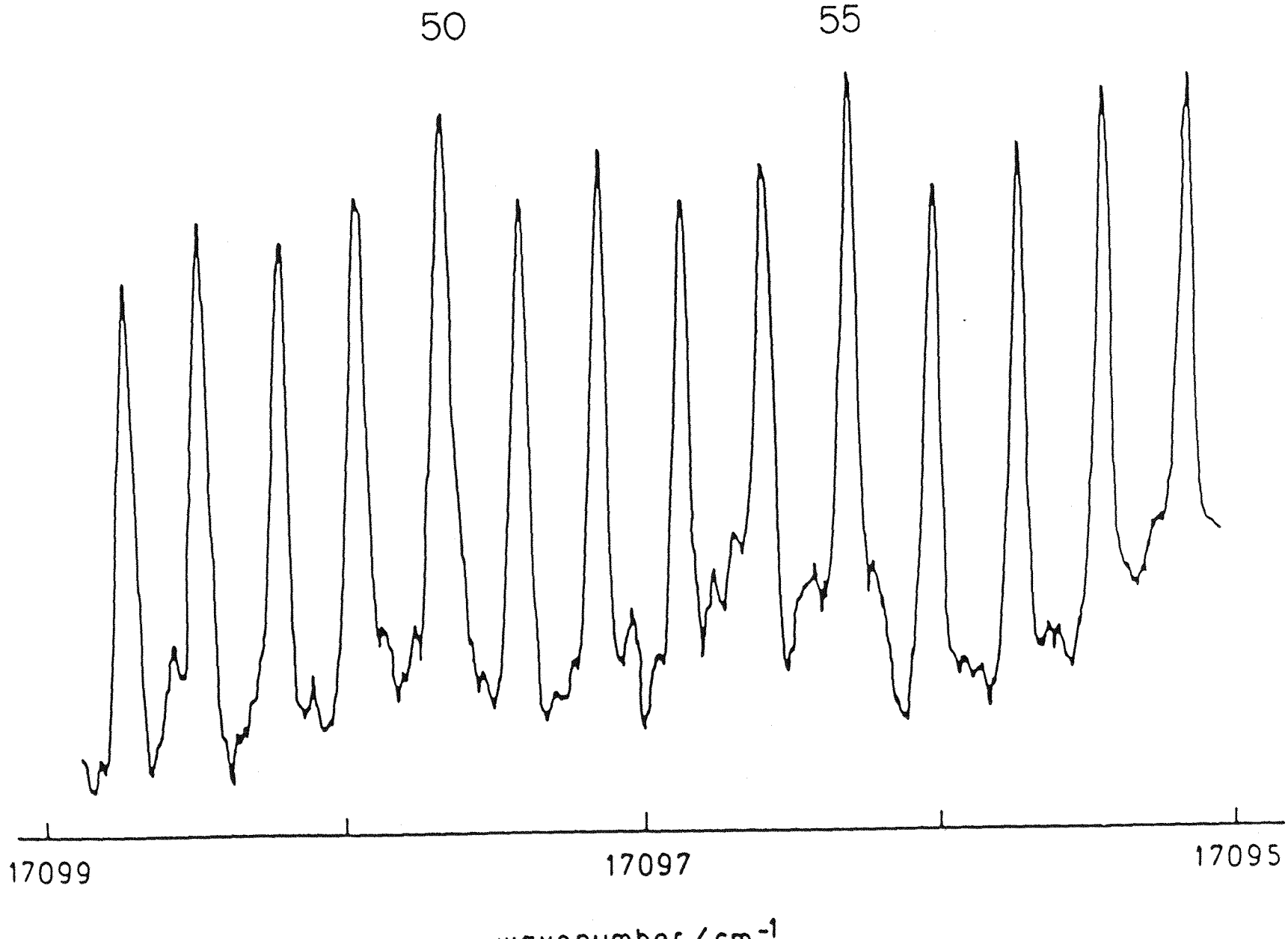
50
55
17099
17097
17095
wavenumber / cm-1

sensitivity. It was possible to follow most of the branches down to the first members, the exceptions being the Q_1 branch where the first 10 lines are not resolved from each other and the first P_1 branch line overlapped by the beginning of the Q_1 branch. It was not felt necessary to determine the position of every line, a selection of about 200 features from throughout the five branches being measured.

Observation of lines in the $^3\Pi_2 - {}^1\Sigma^+$ sub-band were made some time after the original measurements and resulted in the determination of the nature of the excited state. Lines in the Q and R branches of the sub-band for J values from 20 to 70 were observed and also a few weak lines in the P branch around J=30. The signal to noise ratio of the observed lines was typically 10:1 and never more than 20:1. Some of the weaker lines had to be recorded with a longer time constant (1 sec instead of 0.3 sec) to improve the signal to noise ratio. A portion of the Q branch from J=46 to 59 is shown in figure 6. Accurate estimation of the relative intensity of this sub-band is difficult because of the change of dye, and hence laser power, and also the inclusion of the slit and lens in the detection system. Allowing for these factors the lines in the $^3\Pi_2 - {}^1\Sigma^+$ sub-band appear to be about three orders of magnitude weaker than those in the $^3\Pi_1$ and $^3\Pi_{0^+} - {}^1\Sigma^+$ sub-bands. Within the sub-band, the R and P lines are respectively about two and ten times weaker than the Q lines. These relative intensities are completely in accord with the predictions of a second-order perturbation calculation (9,10) carried out to determine whether observation of these transitions was feasible. The result of this calculation is shown in figure 7, which also shows the relative weakness of the R_1 branch, in agreement with the experimental observations. The absence of lines with J less than 20 in the $^3\Pi_2$ branches is also shown. This is consistent with the assignment to a $^3\Pi_2 - {}^1\Sigma^+$ sub-band which acquires intensity through rotational mixing between the Ω = 1 and 2 spin components. Because the Ω doubling in the $^3\Pi_2$ components is small,

Figure 7. Relative intensities of lines in the (0,0) band of the $b^3\Pi - X^1\Sigma^+$ system of CuF. This is a computer simulation based on a second-order perturbation calculation (9,10). Transitions for J between 0 and 90 in multiples of 10 are shown, with the transitions to $^3\Pi_2$ and $^3\Pi_{0-}$ expanded by a factor of 1000. These intensities are in good agreement with the experimental observations.

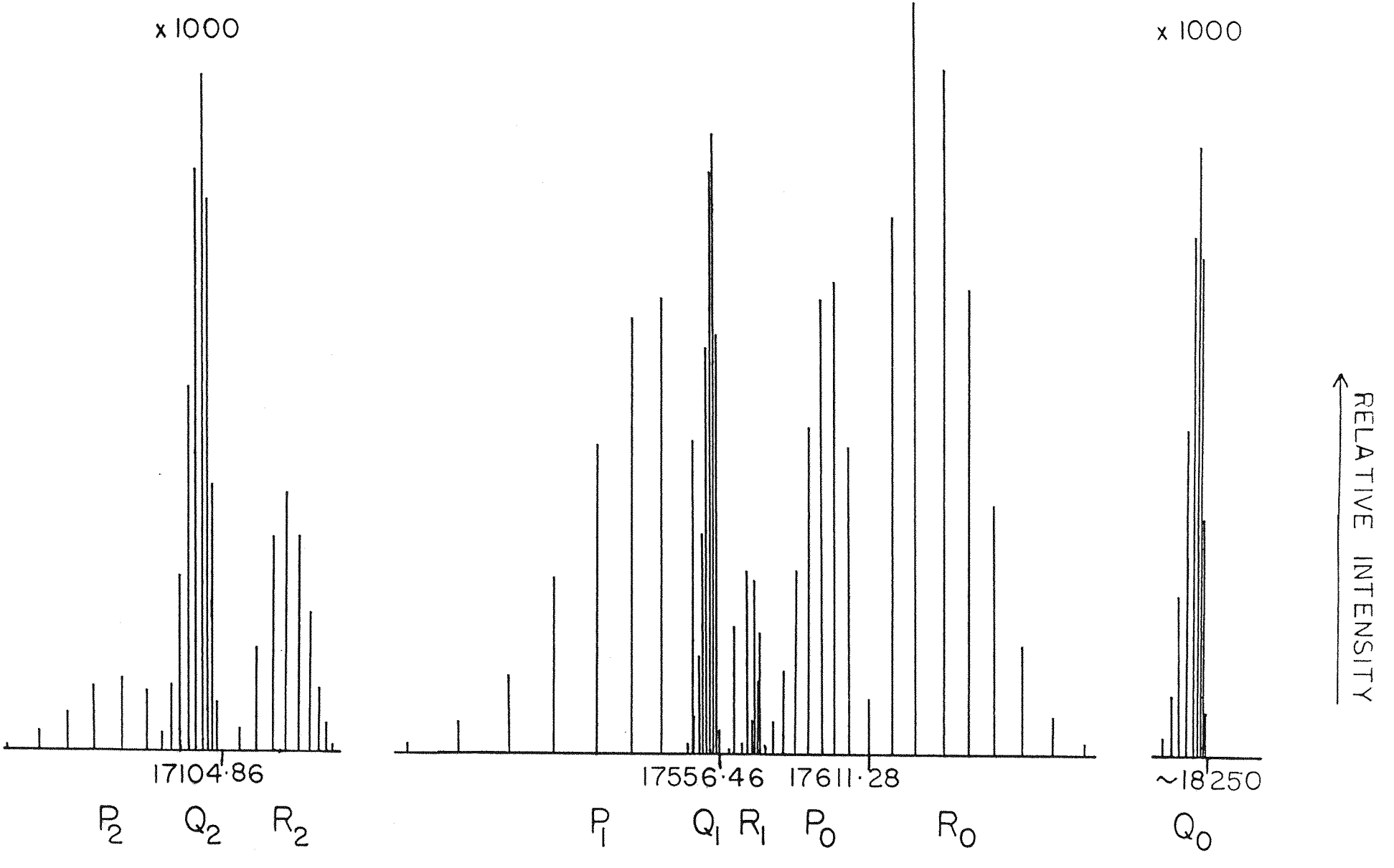
x 1000
x 1000
17104·86
17556·46
17611·28
~18250
P2
Q2
R2
P1
Q1
R1
P0
R0
Q0
RELATIVE INTENSITY

lower-state combination differences R(J)-Q(J+1) could be constructed to confirm that the lower levels belong to the $X^1\Sigma^+$ state v=o and to provide J quantum number assignments.

None of the lines in this sub-band show copper hyperfine splittings although there is some evidence of line broadening. This is consistent with calculations of the hyperfine structure based on the observed splittings in the other sub-bands. No transitions have so far been observed to the $^3\Pi_o$- component, although as can be seen from figure 7, these are expected to have sufficient intensity to be observable. A search of the region from 17700 to 18200 cm^{-1} was made but no lines observed. It is possible that the lines could lie in this region but were missed, because of their weakness, however it is more likely that the sub-band lies more than 18200 cm^{-1} above the ground state. Searching this region would involve the use of a different laser dye coumarin 6 and an associated mirror set, and the information to be gained from this was not considered sufficiently important to make the experiments worthwhile.

Intermodulated Fluorescence

The detection of IMF signals requires that the signal to noise ratio for the line of interest, when observed by laser induced fluorescence, be typically of the order of 1000:1 or greater. The result of this restriction was that only the very strongest lines in the spectrum could be observed, these lay between J=10 and 35 in the R_o and between J=15 and 30 in the P_o, P_1 and Q_1 branches, as can be seen in figure 7. A total of ten rotational lines were examined, four in the R_o branch, two in the P_1 and four in the Q_1.

In all cases the IMF lines were weak with a signal to noise of at best 20:1 in the R_o branch and only between 5 and 10:1 in the P_1 and Q_1 branches, to maximise the signal to noise a long time constant (3 secs) was used. This required very slow scans in order not to distort the signals, which resulted in problems with the laser 'mode-

Figure 8. Hyperfine structure on the $R_0(18)$ line in the (0,0) band of the $b^3\Pi - X^1\Sigma^+$ transition of CuF. This spectrum was recorded using intermodulated fluorescence which reduces the linewidth to about 40 MHz. The frequency was swept more rapidly between each doublet in order to reduce the possibilty of laser mode hops occurring. The splittings were measured by simultaneously recording fringes from a 75 MHz etalon. The structure is interpreted as arising from first copper (I = 3/2) and then fluorine (I = 1/2) nuclear hyperfine interactions.

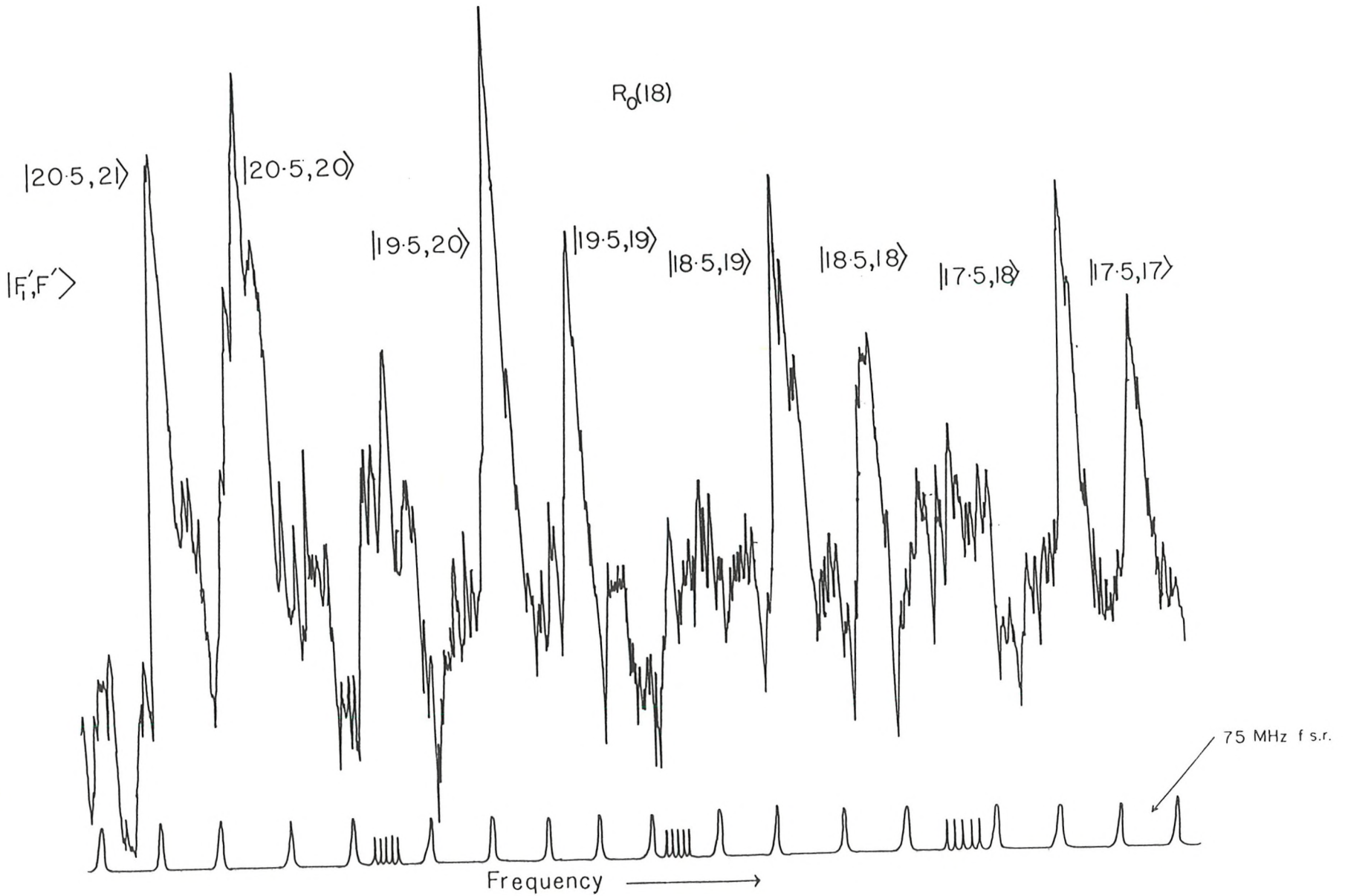
R0(18)
|20·5,21⟩
|20·5,20⟩
|19·5,20⟩
|19·5,19⟩
|18·5,19⟩
|18·5,18⟩
|17·5,18⟩
|17·5,17⟩
|F1′,F′⟩
75 MHz f s.r.
Frequency

Figure 9. Asymmetric hyperfine structure on the $Q_1(19)$ and $Q_1(33)$ lines. The splittings arise from the copper hyperfine interaction, the fluorine splitting is too small to be resolved. For $Q_1(19)$ the $F_1' = 17$ and 18 components are not resolved and give rise to one line of double intensity. These spectra clearly illustrate the large asymmetry in the splittings in the Q_1 branch which arises from a combination of magnetic hyperfine and electric quadrupole interactions.

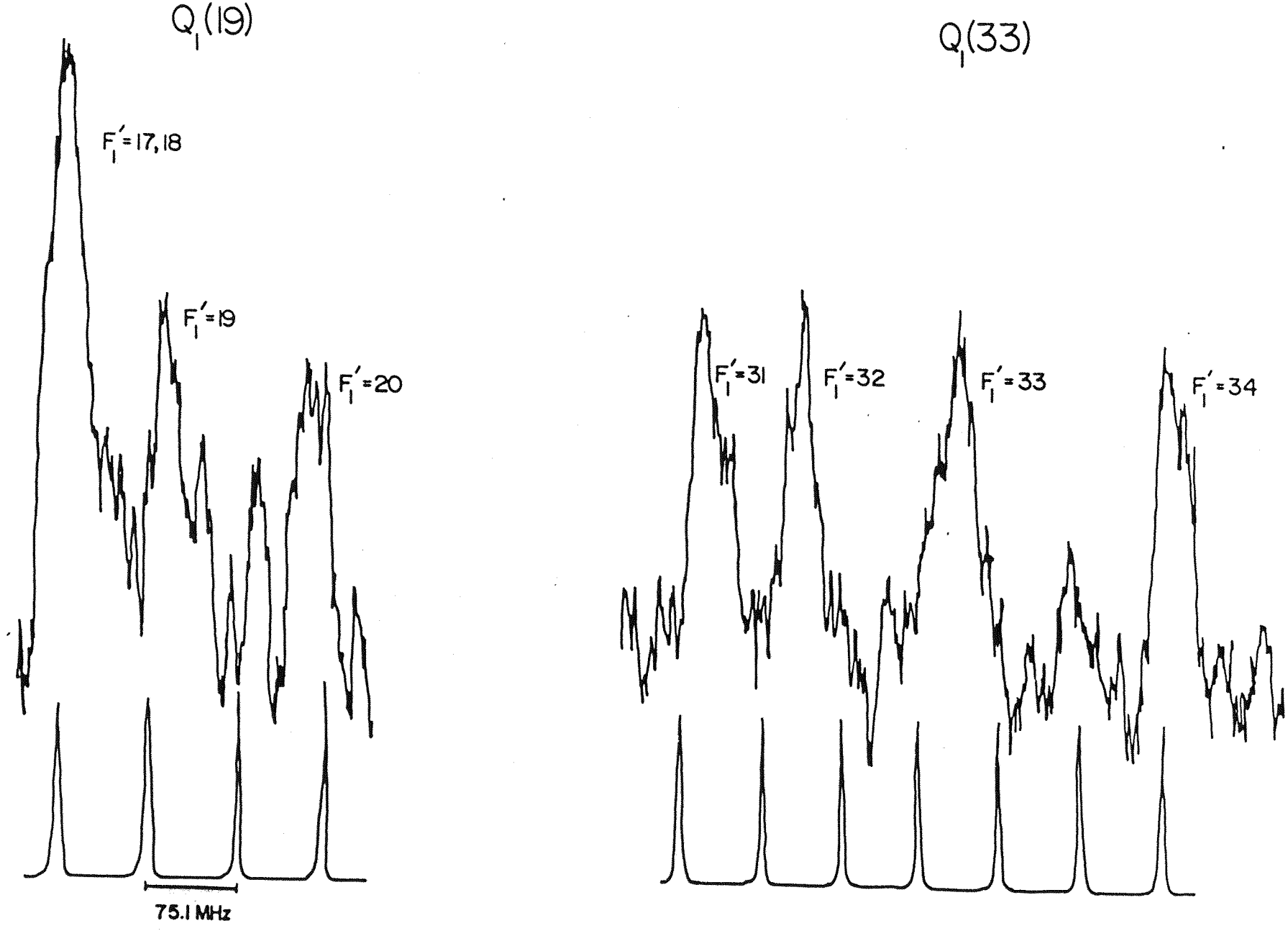
Q1(19)
F1′=17,18
F1′=19
F1′=20
75.1 MHz
Q1(33)
F1′=31
F1′=32
F1′=33
F1′=34

hopping'. Thus it was necessary to record each line several times to make sure that a scan free of 'mode-hops' was obtained. For some lines with relatively large gaps between components it was possible to speed up the scan between lines to reduce this problem. Hyperfine structure had already been observed in the R_0 and P_1 branches at Doppler limited resolution, and the IMF recordings showed the same quartet pattern due to the ^{63}Cu (I=3/2) nucleus continued at lower J. Each of these lines also showed an additional doublet splitting due to the ^{19}F (I=1/2) nucleus, this splitting being about 10% of that due to the copper nucleus. This pattern can be seen in figure 8 which shows one of the lines recorded using the technique of speeding up the scan between components. The pattern of lines in the Q_1 branch was rather different with no sign of any structure due to the fluorine nucleus. As the linewidth was very narrow (FWHM = 0.025 GHz), any fluorine hyperfine effects in this sub-level must be small. Two of the observed rotational lines showed only three copper hyperfine components, with one line of double intensity indicating an unresolved splitting, this is shown in figure 9. Also shown is the pattern at higher J where all four components are resolved and the degree of asymmetry in the splittings, virtually 1:2:3 is clear.

Microwave Optical Double Resonance

The three MODR experiments were performed to obtain information on hyperfine structure at lower J. The first at about 23 GHz was the measurement of the J=0 to J=1 pure rotational transition in the $^3\Pi_{0^+}$ sub-level the pumping scheme for which is indicated in figure 10, which also shows the allowed copper hyperfine components for the two lowest rotational levels. The microwave spectrum, as can be seen from figure 11 shows three components, due to the Cu (I=3/2) nucleus, but there is no observable structure due to the fluorine nucleus. Subsequently the next pure rotational transition J=1 to J=2 at about 46 GHz was examined, for the

Figure 10. Pumping scheme for the J = 1 - 0 MODR transition in the $b^3\Pi_{0+}$ sub-state of CuF. The laser was tuned to the $P_0(1)$ transition which pumps the J = 0 level of the excited state. The microwave radiation at about 23 GHz was then tuned across the three hyperfine components of the transition.

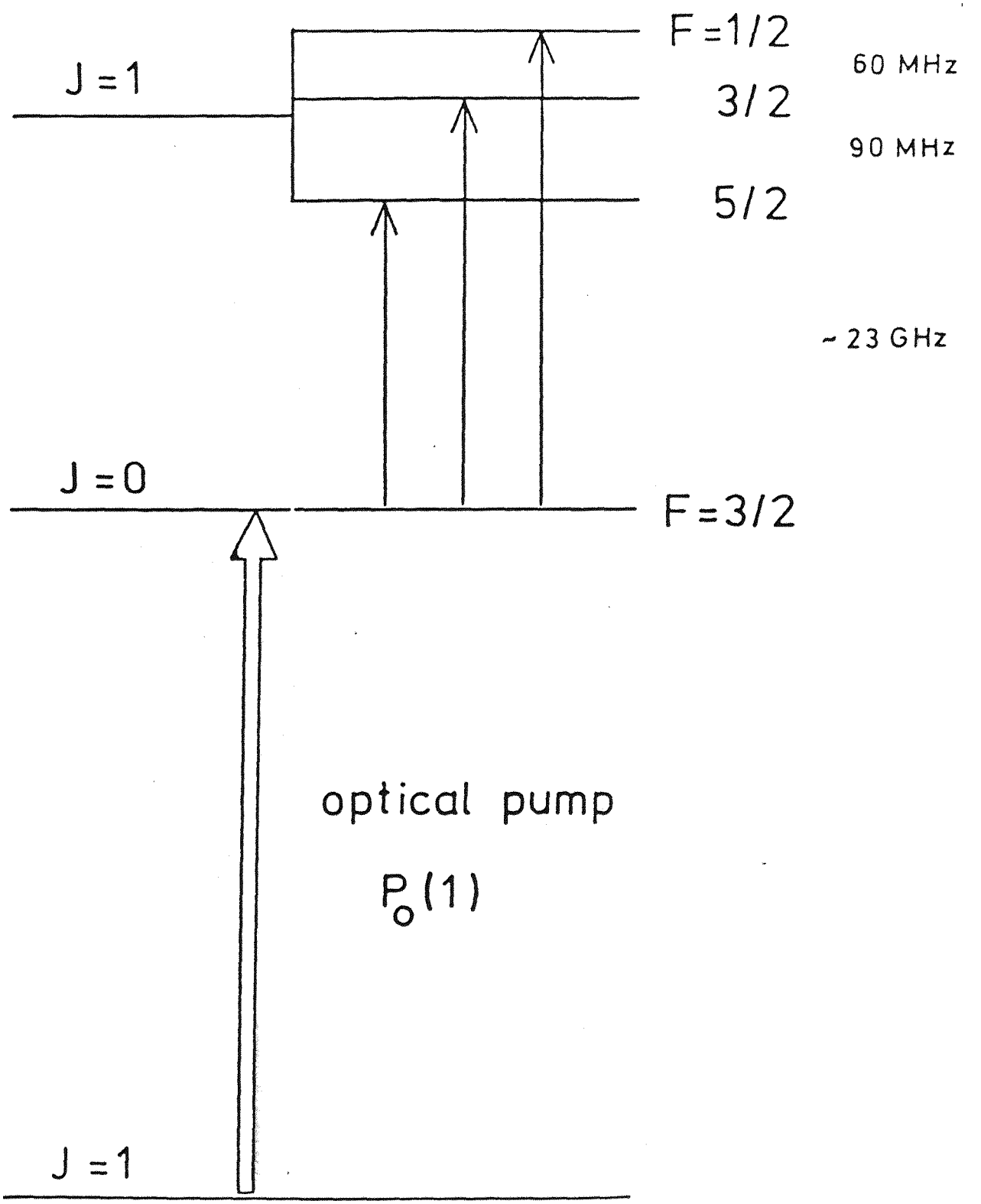
F =1/2
60 MHz
J =1
3/2
90 MHz
5/2
~ 23 GHz
J =0
F=3/2
optical pump
$P_o(1)$
J =1

Figure 11. Hyperfine structure on the J = 1 - 0 pure rotational transition in the v = 0 leve of CuF $b^3\Pi_{0+}$. The three components are due to interactions with the copper nucleus for the J = 1 level. No fluorine hyperfine splitting was observed even at this narrow linewidth of about 5 MHz.

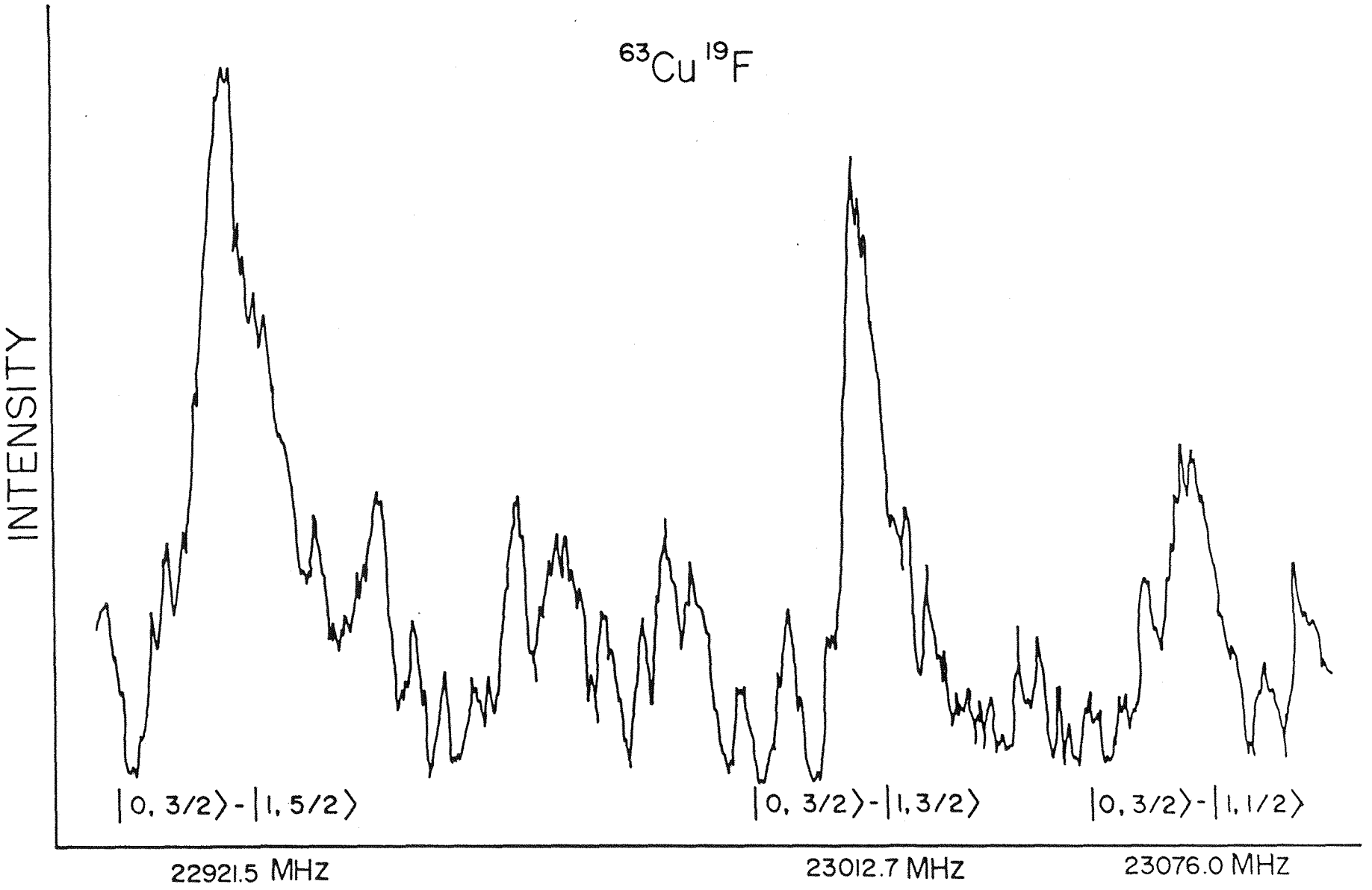
$^{63}Cu\,^{19}F$
INTENSITY
|0, 3/2⟩-|1, 5/2⟩
|0, 3/2⟩-|1, 3/2⟩
|0, 3/2⟩-|1, 1/2⟩
22921.5 MHz
23012.7 MHz
23076.0 MHz

$^3\Pi_{0^+}$ sub-level six lines were observed in three doublets, due to copper and then fluorine hyperfine effects. These lines were considerably weaker than those at 23 GHz with a signal to noise ratio of about 2:1 rather than 10 or 20:1. The most likely explanation for this is a greater rate of collisional relaxation, which was clearly shown to be a major problem by the fact that the lines were only visible at fairly low pressure (150 mTorr).

Although these $^3\Pi_{0^+}$ observations are important in determining the rotational constants they give little additional hyperfine information as the structure observed is merely a continuation of that seen in this sub-level at higher J. The low J lines in the $^3\Pi_1$ sub-level are expected to show quite considerable hyperfine structure but this is only poorly predicted from the visible spectra. This problem is compounded by the fact that when the search for these lines was made the upper state was thought to be $^3\Sigma^-$ and hence the predictions were highly inaccurate. The expected weakness of the lines, perhaps 2:1 coupled with the problem of scanning the wide frequency range necessary, meant that no definite observations were made. One probable line was seen with a signal to noise ratio of about 2:1, but this weakness makes it impossible to say with certainty that it is an MODR transition.

Finally a lambda doubling transition between the $\Omega = 1^+$ and 1^- components in the J=7 level at about 16 GHz was examined. This was expected to show four pairs of lines due to copper and fluorine hyperfine effects, but only one of the doublets was observed. Again this was mainly as a result of poor predictions based on the $^3\Sigma^-$ model for the upper state that was in use at the time. The two lines observed were only seen with good signal to noise, about 10:1, on one occasion when the crucible contents were just beginning to spit out into the path of the laser beam and thus cause large noise spikes, it proved impossible to obtain a repeat of these exact same conditions for the other measurements.

5.4 Fit of the Data

Initial attempts to fit the observations (7) were made using a $^3\Sigma^-$ Hamiltonian (17). The experimental data which consisted only of the LIF and IMF data for the $\Omega = 0^+$ and 1 components were reproduced to the estimated error of 0.007 cm^{-1} and there were no obvious systematic trends in the errors. Thus it was assumed that this was the correct model, however the observation of asymmetry in the hyperfine structure in the $\Omega = 1^-$ component was not readily explicable. Not only was there no asymmetry in the predicted structure, but the total splitting predicted of about 50 MHz at J=30 was much less than the observed value of about 2000 MHz. It was clear that this structure could not be explained by the main Fermi contact and spin dipolar magnetic hyperfine interactions. The most likely additional interaction would be the electric quadrupole term which has the essentially quadratic form necessary to produce asymmetric structure. However the ground state parameter of 21.95 MHz (15) is quite small and the upper state value was likely to be similar, and thus unlikely to account for the size of the splittings. When calculations were made with the quadrupole term included it was found that the size of splitting declined very rapidly with J, the exact opposite of the experimental observations. The only other term considered was the nuclear spin-rotation interaction C_1, but the ground state value for this was even smaller, 36 kHz (15). Calculations were performed with this interaction included but no asymmetry was produced nor did the size of splitting increase significantly with J.

Hence although all the other observations were adequately reproduced by the $^3\Sigma^-$ model the failure to obtain structure even remotely similar to the experimental splittings in the $\Omega = 1^-$ sub-band caused us to reconsider the model used to explain our observations. It was at this point that we learned of theoretical calculations by Schamps which predicted a $^3\Pi$ state at about the position of the yellow system and also showed that any 'p-complex' or $^3\Sigma^-$

levels would be likely to be at a much higher energy above the ground state. To check this possibility we fitted the observed transitions, with hyperfine structure neglected, using the 3 x 3 form of the Hamiltonian described in chapter 2. The unobserved $^3\Pi_2$ and $^3\Pi_{0^-}$ levels were constrained to their calculated positions and the rest of the data were found to fit to essentially the same precision as obtained with the $^3\Sigma^-$ model. As it turns out this is hardly surprising, as the unobserved $^3\Pi$ components are widely separated from the observed levels and hence have little effect on them, the $^3\Pi_{0^+}$ and $^3\Pi_1$ levels thus behave essentially as a $^3\Sigma^-$ state.

It was decided that the way to obtain a conclusive identification would be to observe transitions to one of the previously unobserved components. To see whether this was possible a calculation was made of the intensities of these possible transitions relative to those already observed. The model used was a second-order perturbation treatment (9,10) with two independent transition moments $\mu_{\parallel}$ and $\mu_{\perp}$. The calculation was performed using unfactorised basis states and thus the $^3\Pi$ Hamiltonian was 6 x 6 and the transition matrix between this and the 1 x 1 $^1\Sigma^+$ state was 6 x 1. The parameters obtained from the fit of the observed data to the $^3\Pi$ model were used as input for this calculation and the positions of the unobserved components varied to determine over what range transitions would be likely to be observable. The rotational temperature was varied to obtain a good reproduction of the existing measurements, the best value being about 600K. The values of $\mu_{\parallel}$ and $\mu_{\perp}$ were also varied but the existing structure seemed to be best fitted with both equal to 1. These calculations predicted that both $^3\Pi_{0^-}$ and $^3\Pi_2$ - $^1\Sigma^+$ transitions would be about three orders of magnitude weaker than the previous observations if situated within 100 or 200 cm^{-1} of the theoretical positions, this being the estimated error for those calculations. It was decided to search for the $^3\Pi_2$ component for two reasons, firstly because the laser power in this region is much higher, and secondly because the presence of three

branches increased the range over which transitions would be observable, and thus made the search easier.

The successful observation of transitions to the $^3\Pi_2$ branch meant that these frequencies could now be included in the fit. The full results of this calculation with hyperfine structure omitted were given in ref (11), but the essential details are in table 1. In order to reproduce the data to the estimated experimental error of 0.007 cm^{-1}, it was necessary to include centrifugal distortion corrections A_D and λ_D to the spin-orbit and spin-spin coupling respectively. As can be seen from table 1 all the parameters were determined satisfactorily but there was a very high degree of correlation (-1.0000) between the values of γ and p due to the absence of data on the $^3\Pi_0$- component. This problem was overcome by fitting to the combinations determinable from the data, γ+p and γ-p which are much less correlated. The γ-p combination was only very poorly determined, an added factor in this is that the states connected by γ-p are much further apart than those connected by γ+p and hence the effects produced are much smaller.

To fit all the observations, with hyperfine effects included, it was necessary to set up the full 24 x 24 Hamiltonian matrix for each possible value of F, that is from 0 to 74. The matrices were diagonalised and the eigenvectors used to determine which energies belonged to each basic state. Before any attempt to fit the hyperfine data, it was first required to make assignments for each of the transitions. Although it is often possible to predict the assignments from calculations of the hyperfine parameters, it is clearly better if these can be obtained by analysing the data. This was done by looking at the relative intensities of the components and comparing them with calculated values, these intensities depend very roughly on the value of F and hence the differences are greatest for the very low rotational lines where the ratio, of the difference in F between the lines, to J is greatest.

Table 1. Molecular parameters for ^{63}CuF in the v = 0 level of the $b^3\Pi$ state[a]

T = 17531.109(51)[b]	A = 413.065(26)	10^3A_D = 0.813(59)
λ = -18.653(37)	$10^3\lambda_D$ = -0.439(26)	$\gamma + p$ = 0.2878(29)
B = 0.374740(6)	10^6D = 0.5088(5)	o = 320.0[c]
	$\gamma - p$ = 0.540(97)	10^3q = 0.185(36)

The correlation matrix

	T	A	A_D	λ	λ_D	$\gamma+p$	B	D	$\gamma-p$	q
T	1.0000									
A	-0.9966	1.0000								
A_D	-0.9690	0.9730	1.0000							
λ	-0.9988	0.9973	0.9689	1.0000						
λ_D	-0.8028	0.7837	0.6320	0.8015	1.0000					
$\gamma+p$	0.8696	-0.8823	-0.9640	-0.8698	-0.4049	1.0000				
B	0.3634	-0.4030	-0.5742	-0.3737	0.2332	0.7593	1.0000			
D	-0.5006	0.4433	0.4122	0.4748	0.5587	-0.2847	0.2750	1.0000		
$\gamma-p$	0.9994	-0.9968	-0.9644	-0.9994	-0.8140	0.8604	0.3531	-0.4899	1.0000	
q	0.4933	-0.5168	-0.6914	-0.4932	0.1210	0.8574	0.9507	-0.0109	0.4767	1.0000

[a] The units for all the parameters are cm^{-1}.

[b] The numbers in parentheses represent one standard deviation of the least squares fit, in units of the last quoted decimal place.

[c] The value for o is constrained according to the calculated position of the $^3\Pi_{0^-}$ component.

Figure 12. Calculation of the relative intensities of the hyperfine components of the J = 1 - 0 transitions. The ratio of 3:2:1 is in good agreement with the experimental observations, this intensity variation allows definite assignment of F_1 quantum numbers and also determines the sign of the copper Fermi contact magnetic hyperfine parameter, which provides the main contribution to the splitting.

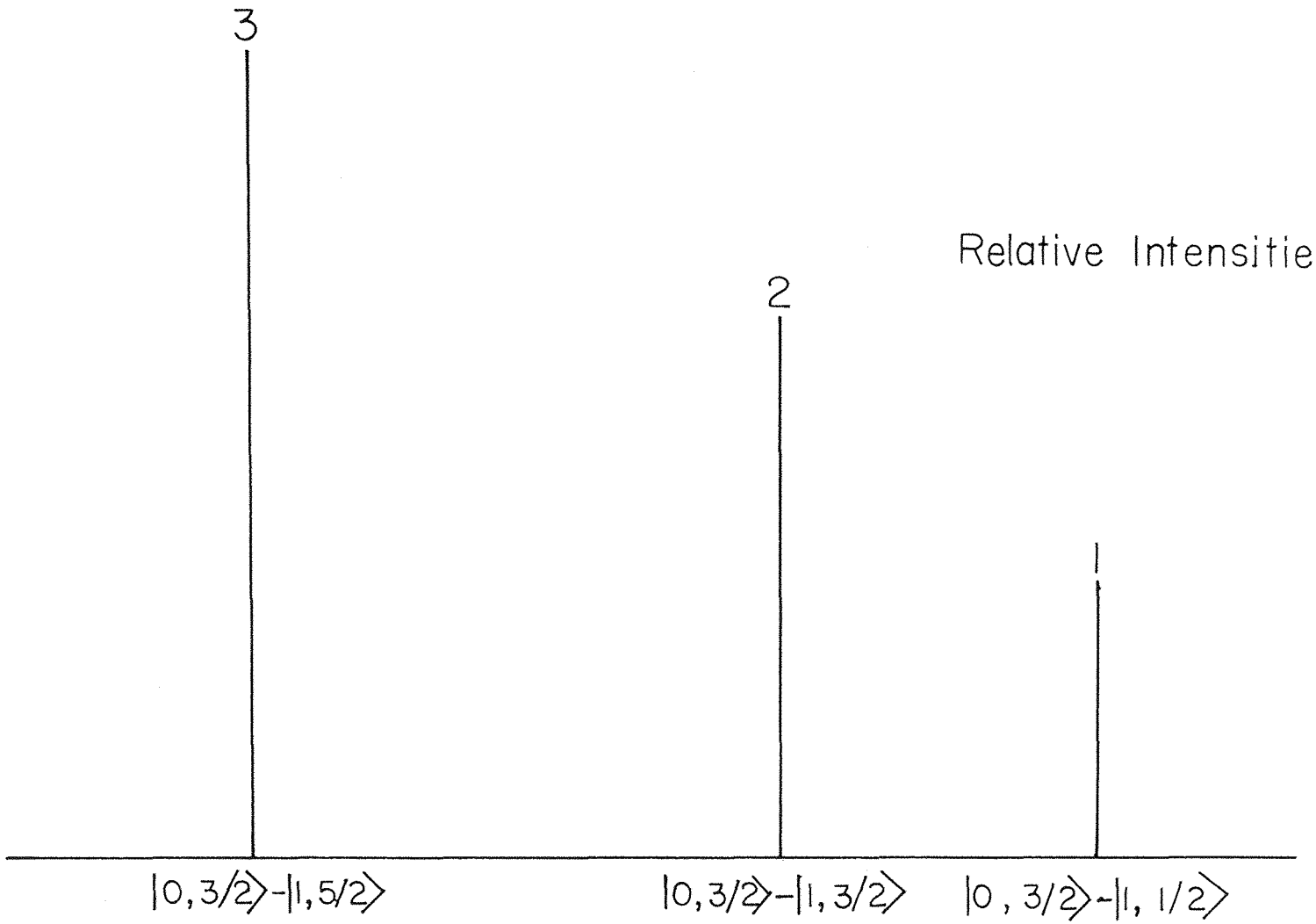
3
2
1
Relative Intensities
|0,3/2⟩-|1,5/2⟩
|0,3/2⟩-|1,3/2⟩
|0,3/2⟩-|1,1/2⟩

The relative intensities are given by the square of

$$\langle \eta\lambda;S\Sigma';J'\Omega';I_1F_1'I_2F'\|\mathfrak{D}^{1)}_{q}(\omega)^*\|\eta\lambda;S\Sigma;J\Omega;I_1F_1I_2F\rangle$$

$$= (-)^{F_1'+I_2+F+1}\begin{Bmatrix} I_2 & F_1' & F \\ 1 & F & F_1 \end{Bmatrix}[(2F'+1)(2F+1)]^{\frac{1}{2}}(-)^{J'+I_1+F_1+1}\begin{Bmatrix} I_1 & J' & F_1' \\ 1 & F_1 & J \end{Bmatrix}$$

$$[(2F_1'+1)(2F_1+1)]^{1/2}\langle \eta\lambda;S\Sigma';J'\Omega'\|\mathfrak{D}^{1)}_{q}(\omega)^*\|\eta\lambda;S\Sigma;J\Omega\rangle \quad 5.1$$

For the J=0 to J=1 MODR transition no fluorine hyperfine effects were observed and thus it is not necessary to include the terms for the second nucleus and they average out to the same when all of the possible components are considered. Evaluation of the above expression for the three possible transitions gives the relative intensities as shown in figure 12. Comparison of this result with the spectrum shown in figure 11 indicates that the lowest lying energy levels in the $\Omega = 0^+$ level are the ones with the highest F_1 quantum number. As the hyperfine structure in the $^3\Pi_{0^+}$ branch is determined by b+d this immediately gives the sign for this parameter combination. Examination of the J=1 to J=2 MODR transition for $\Omega = 0^+$ gives the assignment for the two fluorine components for each line, with again the lower lying level having the higher F quantum number. From these results it was possible to assign quantum numbers for all of the LIF and IMF transitions in the $^3\Pi_{0^+}$ and $^3\Pi_{1^+}$ branches where the structure at high J is determined by b+d for both the copper and fluorine nuclei.

The only problem remaining was the $^3\Pi_{1^-}$ branch with its asymmetric copper hyperfine. Initial calculations of the structure in this branch produced no asymmetry although it was possible to obtain much wider overall splittings of about 300 MHz. However this was still less than the observed structure and also got smaller with increasing J rather than expanding as observed. Variation of all four hyperfine parameters gave no sign of any asymmetry in the region of interest. Clearly additional parameters were required, and the first one considered was the copper quadrupole interaction. The eqoQ term again gave only small

effects at low J but for a $^3\Pi$ state an additional quadrupole parameter occurs eq_2Q which is essentially a lambda doubling term that moves Π^+ and Π^- levels equally in opposite directions. This provides a first order contribution to the energy levels and is esentially independent of J. Inclusion of this parameter resulted in asymmetry in the $^3\Pi_1$- component which reproduced the experimental results to within the estimated error. This interaction must also affect the $^3\Pi_{1+}$ component, but as the effects due to magnetic hyperfine are much greater in this case, the asymmetry produced is not readily observable.

Great differences exist in the accuracies of the various measurements made and it was necessary to use a weighted fit of the results to take account of this. The LIF data were arbitrarily assigned a weight of 1, and the accuracy of each of the IMF and MODR results was estimated, and the ratio of this to the LIF estimated error of 0.007 cm^{-1} calculated, the measurements were then weighted as $1/(\text{relative error})^2$. The IMF results were included as splittings rather than absolute frequencies due to the much smaller estimated error for the differences between the components. If the data were to be treated in a strictly correct manner then an additional measurement, the overall splitting between the first and last component should have been included so that every line would appear twice in the set of measurements (18). Additionally the weight matrix which was taken as being diagonal should have had off-diagonal elements between successive splittings to take account of the fact that the errors for each measurement are correlated to those for the preceeding and succeeding ones. However, this would have involved rewriting the fitting routine which only accepts a diagonal weight matrix, and as the changes produced were expected to be quite small (18) this was not thought necessary.

As the data used in the fit came from different experiments all of the results were required to be the true values and where lines were significantly overlapped it was necessary to deconvolute them. This was especially true of

the splittings observed at high J in the LIF spectra, where the components were only partially resolved. A program was written to obtain the true line positions for each of the four components in the partially resolved spectrum by successive approximation. The lines are broadened by the Doppler effect and the linewidth was estimated to be 1.02 GHz which is consistent with the rotational temperature determined from the branch intensity calculations

$$\Delta\nu = \nu/c(8\ln 2kT/m)^{1/2} \qquad 5.2$$

where ν is the frequency of the transition and m the mass of a $^{63}Cu^{19}F$ molecule. The true positions of the components were estimated from the observed positions and the spectrum calculated by adding a gaussian profile for each line using the formula

$$g(\nu) = 2(\ln 2/\pi)^{1/2}(1/\Delta\nu)\exp\{(-4\ln 2)(\nu-\nu_o)^2/(\Delta\nu^2)\} \qquad 5.3$$

Where ν_o is the centre of the line. The sum of the four gaussians was obtained and the positions of the peaks found. These were compared with the observed positions, if all of them agreed to within 0.0005 cm^{-1} then the values obtained were taken as being the true positions of the components, otherwise the positions were changed, according to the error, and the process repeated. If there was no convergence after ten cycles then the deconvolution was terminated and the results not included in the fit, this occurred for only two of the thirty two rotational lines. The original deconvoluted, and recalulated positions of the other thirty lines are shown in table 2.

The ground state constants were constrained to the values obtained from the microwave measurements (15,16) for B and D ie

$$B_o = 0.377788\ cm^{-1} \qquad D_o = 5.649 \times 10^{-7}\ cm^{-1}$$

Table 2. Deconvolution of LIF hyperfine structure

	Transitions		
	Observed	Recalculated	Deconvoluted
$R_0(28)$	63.3930[a]	63.3930	63.3918
	63.4279	63.4280	63.4282
	63.4691	63.4696	63.4658
	63.4909	63.4910	63.4956
$R_0(29)$	64.3748	64.3748	64.3725
	64.4056	64.4059	64.4055
	64.4390	64.4394	64.4381
	64.4647	64.4648	64.4687
$R_0(30)$	65.3529	65.3530	65.3513
	65.3875	65.3878	65.3859
	65.4183	65.4186	65.4171
	65.4414	65.4416	65.4466
$R_0(31)$	66.3305	66.3305	66.3289
	66.3639	66.3641	66.3639
	66.3998	66.4003	66.3986
	66.4267	66.4269	66.4301
$R_0(32)$	67.3066	67.3067	67.3054
	67.3412	67.3416	67.3410
	67.3758	67.3755	67.3750
	67.4053	67.4056	67.4079
$R_0(36)$	71.2528	71.2529	71.2522
	71.2926	71.2930	71.2916
	71.3260	71.3260	71.3256
	71.3568	71.3568	71.3589
$R_0(37)$	72.2449	72.2451	72.2443
	72.2833	72.2837	72.2832
	72.3206	72.3206	72.3200
	72.3527	72.3529	72.3545
$R_0(39)$	74.2439	74.2440	74.2428
	74.2785	74.2785	74.2788
	74.3170	74.3171	74.3165
	74.3504	74.3504	74.3518
$R_0(43)$	78.1779	78.1780	78.1776
	78.2202	78.2205	78.2200
	78.2587	78.2588	78.2585
	78.2946	78.2944	78.2954
$R_0(44)$	79.1613	79.1613	79.1608
	79.2011	79.2010	79.2013
	79.2509	79.2513	79.2490
	79.2794	79.2797	79.2819

	Observed	Recalculated	Deconvoluted
$R_0(45)$	80.1498	80.1500	80.1494
	80.1896	80.1896	80.1897
	80.2319	80.2323	80.2316
	80.2678	80.2677	80.2686
$P_0(32)$	17.8883	17.8883	17.8864
	17.9204	17.9206	17.9203
	17.9550	17.9554	17.9538
	17.9807	17.9809	17.9846
$P_0(34)$	16.8643	16.8644	16.8630
	16.8989	16.8991	16.8988
	16.9348	16.9351	16.9338
	16.9630	16.9632	16.9659
$P_0(35)$	16.3607	16.3608	16.3592
	16.3941	16.3945	16.3939
	16.4275	16.4273	16.4274
	16.4596	16.4596	16.4614
$P_0(36)$	15.8377	15.8377	15.8367
	15.8736	15.8737	15.8738
	15.9146	15.9150	15.9124
	15.9403	15.9404	15.9437
$P_0(37)$	15.3336	15.3338	15.3327
	15.3695	15.3697	15.3695
	15.4054	15.4051	15.4056
	15.4439	15.4437	15.4444
$P_0(38)$	14.8310	14.8310	14.8294
	14.8644	14.8646	14.8644
	14.9003	14.9008	14.8988
	14.9260	14.9262	14.9297
$P_0(48)$	9.8578	9.8580	9.8569
	9.8937	9.8940	9.8937
	9.9296	9.9295	9.9294
	9.9642	9.9641	9.9653
$P_0(50)$	8.8578	8.8576	8.8559
	8.8899	8.8897	8.8906
	8.9297	8.9296	8.9297
	8.9695	8.9694	8.9699
$P_1(36)$	-58.7489	-58.7488	-58.7521
	-58.7207	-58.7202	-58.7206
	-58.6886	-58.6882	-58.6897
	-58.6655	-58.6653	-58.6602
$P_1(45)$	-71.9421	-71.9421	-71.9433
	-71.9062	-71.9060	-71.9070
	-71.8728	-71.8724	-71.8737
	-71.8459	-71.8457	-71.8424

	Observed	Recalculated	Deconvoluted
$P_1(46)$	-73.4184	-73.4183	-73.4214
	-73.3915	-73.3911	-73.3898
	-73.3543	-73.3541	-73.3553
	-73.3261	-73.3260	-73.3232
$P_1(47)$	-74.9558	-74.9557	-74.9582
	-74.9263	-74.9261	-74.9254
	-74.8904	-74.8901	-74.8913
	-74.8622	-74.8621	-74.8593
$P_1(50)$	-79.5551	-79.5551	-79.5575
	-79.5256	-79.5254	-79.5248
	-79.4884	-79.4880	-79.4907
	-79.4652	-79.4651	-79.4607
$P_1(51)$	-81.1192	-81.1192	-81.1210
	-81.0871	-81.0870	-81.0864
	-81.0486	-81.0486	-81.0496
	-81.0178	-81.0176	-81.0157
$P_1(52)$	-82.7035	-82.7035	-82.7053
	-82.6714	-82.6713	-82.6709
	-82.6342	-82.6343	-82.6353
	-82.6047	-82.6044	-82.6022
$P_1(53)$	-84.2464	-84.2463	-84.2479
	-84.2130	-84.2127	-84.2129
	-84.1771	-84.1774	-84.1781
	-84.1476	-84.1473	-84.1450
$P_1(60)$	-95.4668	-95.4668	-95.4675
	-95.4283	-95.4282	-95.4284
	-95.3885	-95.3881	-95.3904
	-95.3616	-95.3615	-95.3586
$P_1(61)$	-97.0813	-97.0811	-97.0822
	-97.0454	-97.0453	-97.0452
	-97.0069	-97.0068	-97.0076
	-96.9748	-96.9745	-96.9730
$P_1(62)$	-98.7070	-98.7069	-98.7084
	-98.6736	-98.6736	-98.6731
	-98.6351	-98.6350	-98.6358
	-98.6030	-98.6027	-98.6012

[a] All the figures are in cm^{-1} and they correspond to transition energies - 17575 cm^{-1}. The correction due to recalibration of the etalon spacing has not been included and hence all spittings are too large by a factor of 2.5%.

The H value was calculated from the Dunham-Birge formula

$$H_o \approx H_e = 2/3D_e(12(B_e/\omega_e)^2-\alpha_e/\omega_e) \qquad 5.4$$
$$= -2.75 \times 10^{-13}\ cm^{-1}$$

A total of 22 parameters were used to describe the $^3\Pi$ state, 12 fine structure and 10 hyperfine structure constants. Of the fine structure values all except o were allowed to vary, o being constrained to 320 cm^{-1} which fixed the $^3\Pi_{o^-}$ state to the predicted position (8). The individual p and q parameters were used rather than the case a combinations p+2q and q because the large difference between the values of the two parameters meant that $p+2q \approx p$. No H value was included for either state initially, but it was found to be necessary in order to correctly reproduce the high J lines observed in the $^3\Pi_2$ state. Initially all the hyperfine parameters were allowed to vary, but it soon became apparent that insufficient data were available to determine all of them. Inspection of the Hamiltonian matrix (see Chapter 2) shows that the determinable combinations of parameters are as follows:

a from low J lines in $^3\Pi_1$
b+c from low J lines in $^3\Pi_2$
b+d from medium and high J lines in $^3\Pi_{o^+}$ and $^3\Pi_{1^+}$
b-d from medium and high J lines in $^3\Pi_{o^-}$ and $^3\Pi_{1^-}$

This is true for both the copper and fluorine hyperfine effects. No hyperfine structure was observed for low J lines in the $^3\Pi_2$ component hence the b+c combination could not be determined. As c was expected to be small compared to b for the copper nucleus, it was constrained to a calculated value. Sufficient data were available to determine all the other combinations for the copper nucleus. However for fluorine no structure was observed in the $^3\Pi_{1^-}$ component and hence b-d could not be determined. The values of c and d were both constrained and the parameter obtained was effectively $b_F = 1/3c+d$.

The results of the fit are shown in tables 3-6. The LIF measurements in table 3 include both split and unsplit lines, the estimated experimental accuracy for the absolute measurements is 0.007 cm^{-1} and the majority of measurements are within the 95% confidence limit of ± 0.014 cm^{-1}. Any lines which showed a significantly greater error were checked, and where there was a possibility of the laser having 'mode-hopped' or if the iodine reference line was overlapped, and hence not particularly accurate, the line was excluded from the fit, this was only necessary in a few cases. As the split lines were included in the form of absolute frequencies rather than splittings it was not possible to take account of the extra accuracy, with which the differences between the components were measured, in weighting the lines, hence these measurements may have been pushed slightly out by the more heavily weighted IMF lines.

The IMF measurements which were all included as splittings and weighted according to their estimated accuracy appear to fit as a group, with an average error approximately equivalent to the mean of the measurement inaccuracies. Table 4 shows the results of the final fit for the IMF lines, together with the weights. There was quite a high probability of a laser mode-hop in the copper splittings, giving either one extra or one less fringe from the Fabry-Perot interferometer than expected. Two of the splittings originally showed an error of about this magnitude and subsequent re-examination of the spectra showed that a jump of this type had probably ocurred and the results were adjusted accordingly. The weights for these lines were also reduced as the possible error was now clearly higher. The splittings for all of the ten rotational lines included in the fit are adequately reproduced by the calculated constants from the final fit.

Two of the components of the J=0 to J=1 MODR transition have slightly larger than expected errors but these are still just about within the acceptable error range. Some of the error may be due to the way the effects of fluorine hyperfine were included, the transition frequency being

Table 3. Measured transitions in the (0,0) $b^3\Pi - X^1\Sigma^+$ band of ^{63}CuF[a]

Branch	Observed	Obs-Calc	Branch	Observed	Obs-Calc
$R_0(0)$	17613.412	0.001	$R_2(37)$	17129.186	-0.005
$R_0(1)$	17614.189	-0.001	$R_2(38)$	17129.721	0.000
$R_0(2)$	17614.975	-0.003	$R_2(39)$	17130.238	-0.004
$R_0(3)$	17615.789	0.013	$R_2(40)$	17130.764	0.003
$R_0(12)$	17623.428	0.019	$R_2(41)$	17131.281	0.007
$R_0(13)$	17624.291	-0.011	$R_2(42)$	17131.781	-0.000
$P_0(1)$	17611.895	0.005	$R_2(43)$	17132.283	0.000
$P_0(2)$	17611.148	0.003	$R_2(44)$	17132.783	0.002
$P_0(3)$	17610.412	-0.001	$R_2(45)$	17133.277	0.004
$P_0(4)$	17609.689	-0.001	$R_2(46)$	17133.754	-0.006
$P_0(13)$	17603.635	-0.009	$R_2(47)$	17134.248	0.006
$P_0(14)$	17603.010	-0.009	$R_2(48)$	17134.723	0.003
$P_0(19)$	17600.014	-0.008	$R_2(49)$	17135.195	0.005
$P_0(20)$	17599.436	-0.008	$R_2(50)$	17135.662	0.004
$R_1(0)$	17557.205	0.007	$R_2(51)$	17136.117	-0.004
$R_1(1)$	17557.924	0.011	$R_2(52)$	17136.578	-0.001
$R_1(2)$	17558.609	0.008	$R_2(53)$	17137.027	-0.006
$R_1(3)$	17559.262	-0.004	$R_2(54)$	17137.477	-0.005
$R_1(9)$	17562.758	-0.004	$R_2(55)$	17137.939	0.014
$R_1(10)$	17563.258	-0.009	$R_2(56)$	17138.363	-0.001
$R_1(11)$	17563.752	0.001	$R_2(57)$	17138.801	0.000
$R_1(20)$	17567.188	0.004	$R_2(58)$	17139.221	-0.012
$R_1(21)$	17567.455	-0.015	$R_2(59)$	17139.645	-0.015
$R_1(22)$	17567.742	0.003	$R_2(60)$	17140.088	0.006
$R_1(23)$	17567.998	0.006	$R_2(61)$	17140.496	-0.004
$Q_1(10)$	17556.268	0.005	$R_2(62)$	17140.912	-0.003
$Q_1(11)$	17556.219	-0.000	$R_2(63)$	17141.344	0.018
$Q_1(12)$	17556.172	-0.001	$R_2(64)$	17141.713	-0.021
$Q_1(13)$	17556.123	0.002	$R_2(65)$	17142.123	-0.012
$Q_1(14)$	17556.070	0.004	$R_2(66)$	17142.538	0.003
$Q_1(15)$	17556.012	0.003	$R_2(67)$	17142.927	-0.004
$Q_1(16)$	17555.943	-0.003	$R_2(68)$	17143.330	0.006
$Q_1(17)$	17555.871	-0.009	$R_2(69)$	17143.711	-0.002
$Q_1(18)$	17555.807	-0.003	$Q_2(22)$	17103.367	-0.008
$Q_1(19)$	17555.738	0.002	$Q_2(23)$	17103.232	-0.009
$Q_1(20)$	17555.666	0.007	$Q_2(24)$	17103.098	-0.005
$Q_1(21)$	17555.590	0.012	$Q_2(25)$	17102.971	0.011
$Q_1(22)$	17555.506	0.013	$Q_2(26)$	17102.814	0.004
$Q_1(23)$	17555.406	0.002	$Q_2(27)$	17102.662	0.008
$Q_1(24)$	17555.313	-0.000	$Q_2(28)$	17102.492	-0.002
$Q_1(25)$	17555.215	-0.004	$Q_2(29)$	17102.322	-0.006
$Q_1(26)$	17555.115	-0.004	$Q_2(30)$	17102.152	-0.005

Branch	Observed	Obs-Calc	Branch	Observed	Obs-Calc
$Q_1(27)$	17555.006	-0.010	$Q_2(31)$	17101.973	-0.009
$Q_1(28)$	17554.902	-0.008	$Q_2(32)$	17101.787	-0.014
$Q_1(29)$	17554.799	-0.003	$Q_2(33)$	17101.609	-0.005
$Q_1(30)$	17554.684	-0.004	$Q_2(34)$	17101.430	0.008
$Q_1(31)$	17554.564	-0.007	$Q_2(35)$	17101.232	0.007
$Q_1(32)$	17554.455	0.003	$Q_2(36)$	17101.035	0.012
$Q_1(33)$	17554.314	-0.016	$Q_2(37)$	17100.818	0.001
$Q_1(34)$	17554.189	-0.015	$Q_2(38)$	17100.600	-0.005
$Q_1(35)$	17554.059	-0.016	$Q_2(39)$	17100.396	0.007
$Q_1(36)$	17553.930	-0.013	$Q_2(40)$	17100.168	-0.000
$Q_1(37)$	17553.799	-0.008	$Q_2(41)$	17099.926	-0.015
$Q_1(38)$	17553.670	0.002	$Q_2(42)$	17099.699	-0.010
$Q_1(39)$	17553.521	-0.005	$Q_2(43)$	17099.475	-0.001
$Q_1(40)$	17553.379	-0.005	$Q_2(44)$	17099.232	-0.003
$Q_1(41)$	17553.230	-0.005	$Q_2(45)$	17098.992	0.002
$Q_1(42)$	17553.088	0.002	$Q_2(46)$	17098.744	0.003
$Q_1(43)$	17552.949	0.017	$Q_2(47)$	17098.482	-0.005
$Q_1(44)$	17552.785	0.010	$Q_2(48)$	17098.236	0.006
$Q_1(45)$	17552.623	0.005	$Q_2(49)$	17097.963	-0.005
$Q_1(47)$	17552.297	0.004	$Q_2(50)$	17097.701	0.001
$Q_1(48)$	17552.129	0.002	$Q_2(51)$	17097.426	-0.005
$P_1(3)$	17554.127	-0.007	$Q_2(52)$	17097.148	-0.008
$P_1(4)$	17553.299	-0.014	$Q_2(53)$	17096.881	0.003
$P_1(5)$	17552.457	-0.009	$Q_2(54)$	17096.590	-0.007
$P_1(17)$	17540.572	0.014	$Q_2(55)$	17096.303	-0.008
$P_1(18)$	17539.439	0.007	$Q_2(56)$	17096.014	-0.006
$P_1(22)$	17534.744	0.006	$Q_2(57)$	17095.725	-0.003
$P_1(23)$	17533.520	-0.003	$Q_2(58)$	17095.434	0.003
$R_2(23)$	17121.219	0.006	$Q_2(59)$	17095.143	0.012
$R_2(24)$	17121.811	-0.008	$Q_2(60)$	17094.826	0.000
$R_2(25)$	17122.422	0.008	$Q_2(61)$	17094.516	-0.003
$R_2(26)$	17123.014	0.004	$Q_2(62)$	17094.205	-0.002
$R_2(27)$	17123.596	-0.005	$Q_2(63)$	17093.902	0.007
$R_2(28)$	17124.180	-0.006	$Q_2(64)$	17093.584	0.005
$R_2(29)$	17124.768	0.003	$Q_2(65)$	17093.270	0.011
$R_2(30)$	17125.350	0.013	$Q_2(66)$	17092.928	-0.010
$R_2(31)$	17125.914	0.011	$Q_2(67)$	17092.611	-0.001
$R_2(32)$	17126.463	-0.003	$Q_2(68)$	17092.297	0.011
$R_2(33)$	17127.027	0.005	$Q_2(69)$	17091.951	-0.002
$R_2(34)$	17127.578	0.007	$Q_2(70)$	17091.625	0.003
$R_2(35)$	17128.119	0.002	$Q_2(71)$	17091.293	0.006
$R_2(36)$	17128.652	-0.004	$Q_2(72)$	17090.961	0.010

Branch	F	Observed	Obs-Calc
$R_0(28)$	27.5	17638.495	0.004
$R_0(28)$	28.5	17638.465	0.006
$R_0(28)$	29.5	17638.429	0.001
$R_0(28)$	30.5	17638.393	-0.001
$R_0(29)$	28.5	17639.468	-0.001
$R_0(29)$	29.5	17639.438	0.001
$R_0(29)$	30.5	17639.406	0.001
$R_0(29)$	31.5	17639.374	0.003
$R_0(30)$	29.5	17640.446	-0.004
$R_0(30)$	30.5	17640.417	-0.000
$R_0(30)$	31.5	17640.386	0.003
$R_0(30)$	32.5	17640.353	0.003
$R_0(31)$	30.5	17641.429	-0.003
$R_0(31)$	31.5	17641.398	-0.001
$R_0(31)$	32.5	17641.364	-0.001
$R_0(31)$	33.5	17641.330	0.000
$R_0(32)$	31.5	17642.407	-0.009
$R_0(32)$	32.5	17642.375	-0.008
$R_0(32)$	33.5	17642.341	-0.007
$R_0(32)$	34.5	17642.307	-0.005
$R_0(36)$	35.5	17646.358	-0.009
$R_0(36)$	36.5	17646.325	-0.006
$R_0(36)$	37.5	17646.292	-0.002
$R_0(36)$	38.5	17646.254	-0.002
$R_0(37)$	36.5	17647.353	-0.004
$R_0(37)$	37.5	17647.320	-0.001
$R_0(37)$	38.5	17647.284	0.001
$R_0(37)$	39.5	17647.246	0.001
$R_0(39)$	38.5	17649.340	0.003
$R_0(39)$	39.5	17649.306	0.006
$R_0(39)$	40.5	17649.269	0.007
$R_0(39)$	41.5	17649.234	0.012
$R_0(43)$	42.5	17653.294	-0.004
$R_0(43)$	43.5	17653.258	-0.000
$R_0(43)$	44.5	17653.221	0.002
$R_0(43)$	45.5	17653.179	0.003
$R_0(44)$	43.5	17654.281	-0.006
$R_0(44)$	44.5	17654.249	0.002
$R_0(44)$	45.5	17654.202	-0.004
$R_0(44)$	46.5	17654.162	-0.001
$R_0(45)$	44.5	17655.267	-0.007
$R_0(45)$	45.5	17655.231	-0.003
$R_0(45)$	46.5	17655.190	-0.003
$R_0(45)$	47.5	17655.151	0.000

Branch	F	Observed	Obs-Calc
$P_0(32)$	29.5	17592.984	-0.006
$P_0(32)$	30.5	17592.953	-0.004
$P_0(32)$	31.5	17592.921	-0.003
$P_0(32)$	32.5	17592.888	-0.002
$P_0(34)$	31.5	17591.965	0.002
$P_0(34)$	32.5	17591.933	0.004
$P_0(34)$	33.5	17591.899	0.005
$P_0(34)$	34.5	17591.864	0.006
$P_0(35)$	32.5	17591.460	0.007
$P_0(35)$	33.5	17591.427	0.008
$P_0(35)$	34.5	17591.394	0.010
$P_0(35)$	35.5	17591.360	0.013
$P_0(36)$	33.5	17590.943	-0.003
$P_0(36)$	34.5	17590.912	0.001
$P_0(36)$	35.5	17590.874	-0.001
$P_0(36)$	36.5	17590.838	-0.000
$P_0(37)$	34.5	17590.443	0.002
$P_0(37)$	35.5	17590.405	-0.000
$P_0(37)$	36.5	17590.370	0.001
$P_0(37)$	37.5	17590.334	0.003
$P_0(38)$	35.5	17589.929	-0.009
$P_0(38)$	36.5	17589.898	-0.003
$P_0(38)$	37.5	17589.865	0.000
$P_0(38)$	38.5	17589.831	0.004
$P_0(48)$	45.5	17584.964	-0.003
$P_0(48)$	46.5	17584.929	0.003
$P_0(48)$	47.5	17584.894	0.009
$P_0(48)$	48.5	17584.858	0.017
$P_0(50)$	47.5	17583.969	-0.011
$P_0(50)$	48.5	17583.929	-0.009
$P_0(50)$	49.5	17583.891	-0.004
$P_0(50)$	50.5	17583.857	0.006
$P_1(36)$	33.5	17516.249	0.004
$P_1(36)$	34.5	17516.280	0.002
$P_1(36)$	35.5	17516.310	-0.001
$P_1(36)$	36.5	17516.339	-0.003
$P_1(45)$	42.5	17503.069	-0.003
$P_1(45)$	43.5	17503.105	-0.004
$P_1(45)$	44.5	17503.137	-0.007
$P_1(45)$	45.5	17503.168	-0.012
$P_1(46)$	43.5	17501.580	0.019
$P_1(46)$	44.5	17501.611	0.015
$P_1(46)$	45.5	17501.644	0.012
$P_1(46)$	46.5	17501.676	0.009

Branch	F	Observed	Obs-Calc
$P_1(47)$	44.5	17500.043	0.007
$P_1(47)$	45.5	17500.075	0.002
$P_1(47)$	46.5	17500.108	-0.001
$P_1(47)$	47.5	17500.139	-0.006
$P_1(50)$	47.5	17495.434	0.017
$P_1(50)$	48.5	17495.466	0.011
$P_1(50)$	49.5	17495.500	0.008
$P_1(50)$	50.5	17495.529	0.001
$P_1(51)$	48.5	17493.870	0.008
$P_1(51)$	49.5	17493.903	0.004
$P_1(51)$	50.5	17493.939	0.003
$P_1(51)$	51.5	17493.972	-0.001
$P_1(52)$	49.5	17492.296	-0.002
$P_1(52)$	50.5	17492.329	-0.006
$P_1(52)$	51.5	17492.364	-0.009
$P_1(52)$	52.5	17492.396	-0.014
$P_1(53)$	50.5	17490.744	0.017
$P_1(53)$	51.5	17490.778	0.013
$P_1(53)$	52.5	17490.812	0.009
$P_1(53)$	53.5	17490.844	0.005
$P_1(60)$	57.5	17479.534	-0.005
$P_1(60)$	58.5	17479.572	-0.007
$P_1(60)$	59.5	17479.609	-0.009
$P_1(60)$	60.5	17479.640	-0.016
$P_1(61)$	58.5	17477.919	0.003
$P_1(61)$	59.5	17477.955	-0.001
$P_1(61)$	60.5	17477.992	-0.003
$P_1(61)$	61.5	17478.026	-0.008
$P_1(62)$	59.5	17476.293	0.005
$P_1(62)$	60.5	17476.327	-0.001
$P_1(62)$	61.5	17476.364	-0.004
$P_1(62)$	62.5	17476.397	-0.008

[a] All energies are in cm^{-1}. Those transitions with unassigned F′ values have unresolved hyperfine splittings and are weighted four times greater than the resolved components.

Table 4. Hyperfine splittings in CuF $b^3\Pi$ from IMF data[a]

Splitting				Observed	Obs-Calc	Weight
F_1-1/2	F	F_1-1/2	F			
$R_0(11)$						
13	13	13	14	0.00191	-0.00009	400
12	13	13	13	0.01545	0.00037	583
12	12	12	13	0.00192	-0.00008	583
11	12	12	12	0.01446	0.00056	725
11	11	11	12	0.00214	0.00013	479
10	11	11	11	0.01269	0.00001	450
10	10	10	11	0.00224	0.00021	213
$R_0(18)$						
20	20	20	21	0.00294	-0.00002	725
19	20	20	20	0.02180	0.00013	926
19	19	19	20	0.00309	0.00012	1914
18	19	19	19	0.02149	0.00103	1235
18	18	18	19	0.00324	0.00027	1012
17	18	18	18	0.01941	0.00016	4900
17	17	17	18	0.00299	0.00000	1111
$R_0(20)$						
22	22	22	23	0.00331	0.00010	672
21	22	22	22	0.02414	0.00080	378
21	21	21	22	0.00350	0.00029	196
20	21	21	21	0.02181	-0.00032	306
20	20	20	21	0.00367	0.00045	358
19	19	19	20	0.00321	-0.00002	625
$R_0(28)$						
30	30	30	31	0.00421	0.00018	400
29	30	30	30	0.02708	-0.00204	291
29	29	29	30	0.00367	-0.00036	1012
28	29	29	29	0.02685	-0.00106	851
28	28	28	29	0.00376	-0.00028	544
27	28	28	28	0.02622	-0.00048	510
27	27	27	28	0.00391	-0.00014	725

Splitting				Observed	Obs-Calc	Weight
F_1-1/2	F	- F_1-1/2	F			
$P_1(17)$						
14	15	14	14	0.00304	0.00044	306
15	15	14	15	0.01849	0.00044	358
15	16	15	15	0.00301	0.00043	253
16	16	15	16	0.01782	0.00033	253
16	17	16	16	0.00253	-0.00005	242
17	17	16	17	0.01814	0.00159	213
$P_1(25)$						
22	23	22	22	0.00362	0.00006	544
23	23	22	23	0.02285	-0.00046	1357
23	24	23	23	0.00372	0.00017	784
24	24	23	24	0.02373	0.00109	213
24	25	24	24	0.00355	0.00000	672
25	26	25	25	0.00354	0.00012	400
F_1-1/2	-	F_1-1/2				
$Q_1(19)$						
18		19 & 20		0.00248	0.00040	784
17		18		0.00409	0.00007	784
$Q_1(21)$						
20		21 & 22		0.00326	0.00050	162
19		20		0.00444	-0.00003	71
$Q_1(27)$						
27		28		0.00157	-0.00025	2500
26		27		0.00359	-0.00027	1357
25		26		0.00545	-0.00026	672
$Q_1(33)$						
33		34		0.00284	0.00002	1357
32		33		0.00492	-0.00002	851
31		32		0.00680	-0.00006	510

[a] All measurements are in cm^{-1}. The transitions without F quantum numbers contain unresolved fluorine hyperfine structure.

Table 5. MODR transitions in the $b^3\Pi$ state of CuF

Upper State				Lower State				Observed (cm^{-1})	Obs-Calc (cm^{-1})	Weight
Ω	J	F_1	F	Ω	J	F_1	F			
0^+	1	2.5	3	0^+	0	1.5	2	0.76458	0.00016	16800
0^+	1	1.5	2	0^+	0	1.5	2	0.76762	0.00002	33900
0^+	1	0.5	1	0^+	0	1.5	2	0.76973	-0.00011	10300
0^+	2	3.5	4	0^+	1	2.5	3	1.53069	0.00003	1000
0^+	2	3.5	3	0^+	1	2.5	2	1.53086	0.00001	1000
0^+	2	2.5	3	0^+	1	1.5	2	1.53186	-0.00012	1000
0^+	2	2.5	2	0^+	1	1.5	1	1.53213	-0.00008	1000
0^+	2	1.5	2	0^+	1	0.5	1	1.53323	0.00011	1000
0^+	2	1.5	1	0^+	1	0.5	0	1.53359	0.00008	1000
1^-	7	5.5	5	1^+	7	5.5	5	0.55988	0.00030	1000
1^-	7	5.5	6	1^+	7	5.5	6	0.55879	0.00045	1000

Table 6. Parameters for ^{63}CuF in v=0 of the $b^3\Pi$ state[a]

TE	=	17531.304(20)[b]	γ	=	0.320(19)
A	=	-413.166(10)	B	=	0.374763(5
10^3 A_D	=	0.632(17)	10^6 D	=	0.5102(4)
λ	=	-18.799(15)	o	=	320.0[c]
10^3 λ_D	=	-0.534(17)	p	=	-0.600(19)
			10^3 q	=	0.317(27)

Copper hyperfine

a	=	0.0255(43)	d	=	-0.0556(67)
b_F	=	0.1304(67)	10^3 eq_0Q	=	-0.030(15)
c	=	0.0064[c]	eq_2Q	=	0.01615(81)

Fluorine hyperfine

a	=	0.005(3)	b + d	=	0.00928(19)

[a] The units for all parameters are cm^{-1}.

[b] The numbers in parentheses represent one standard deviation of the least squares fit, in units of the last quoted decimal place.

[c] The values for o and c are constrained in the least squares fit.

calculated by simply adding together the frequencies of the various transitions possible for each copper hyperfine component and weighting them according to the calculated strength for each fluorine component. To be strictly accurate a lineshape should have been added to each component and the peak of the convoluted line found, however as all the components were very close together the result of not including the convolution is likely to have been quite small. The reproduction of all the other lines included is fairly good, these were all assigned a weight of 1000 as the signal to noise of the measurements was poor and thus the accuracy hard to estimate. It was not possible to assign the one line which seemed to be reproducible in the $^3\Pi_1$+ J=1 to J=2 MODR spectrum.

The overall standard deviation of the fit relative to the experimental uncertainty was 1.15, which shows that the data were not reproduced as well as was expected, but the descrepancy is quite small and could well be due to over-estimating the accuracy of some of the experimental data. As can be seen from table 6 it proved possible to determine 18 parameters from the fit, although two of them eqoQ and a for the fluorine nucleus, are only just determined, due to a lack of data of sufficient accuracy concerning the levels where these parameters are most important. Table 6 also gives the correlation matrix, the problem of the very high correlation between γ and p is reduced somewhat by the inclusion of the hyperfine measurements, which are affected by the mixing of components caused by the spin-rotation and lambda doubling, although it is still quite high. The only other very large correlation is between b_F and d, this is because while b+d is well determined, there is only a small amount of data on b-d and hence this is only poorly determined.

5.5 Interpretation

Fine Structure

This investigation of the $b^3\Pi$-$X^1\Sigma^+$ system of CuF has involved only the $v' = 0 \leftarrow v'' = 0$ vibrational band and hence the constants determined for the upper state refer only to $v' = 0$. To obtain equilibrium values it would be necessary to fit some of the other vibrational bands using the $^3\Pi$ model. As these are much weaker than the (0,0) band it is unlikely that any transitions to the $^3\Pi_2$ component would be observable.

Approximate values, for the spin-orbit and spin-spin terms, may be calculated from a second order perturbation treatment of the atomic spin-orbit interactions between the different states arising from the ionic configuration, which provides the main contribution to the $^3\Pi$ state. The configuration involved

$$Cu^+(1s^2,2s^2,2p^6,3s^2,3p^6,3d^9,4s^1)F^-(1s^22s^22p^6\rangle$$

gives rise to six possible electronic states from the three different types of 3d orbital, each one forming a singlet and triplet combination with the 4s electron.

$Cu^+(3d[\delta^3\pi^4\sigma^2]4s[\sigma^1])$ $^3\Delta$ and $^1\Delta$
$Cu^+(3d[\delta^4\pi^3\sigma^2]4s[\sigma^1])$ $^3\Pi$ and $^1\Pi$
$Cu^+(3d[\delta^4\pi^4\sigma^1]4s[\sigma^1])$ $^3\Sigma^+$ and $^1\Sigma^+$

The calculations were performed using the spin-orbit Hamiltonian of Dufour et al (8), the off diagonal elements being

$$\langle {}^3\Sigma_0|\zeta|_{1,}.s_{1,}|{}^3\Pi_{0-}\rangle = \sqrt{(3/2}\ \zeta$$
$$\langle {}^1\Sigma_0|\zeta|_{1,}.s_{1,}|{}^3\Pi_{0+}\rangle = -\sqrt{(3/2}\ \zeta$$
$$\langle {}^1\Pi_1|\zeta|_{1,}.s_{1,}|{}^3\Pi_1\rangle = -\sqrt{(1/2}\ \zeta$$
$$\langle {}^3\Pi_1|\zeta|_{1,}.s_{1,}|{}^3\Delta_1\rangle = \sqrt{(1/2}\ \zeta$$

$\langle {}^3\Sigma_1|\zeta l_i.s_i|{}^3\Pi_1\rangle = 1/2\sqrt{(3}\ \zeta$

$\langle {}^3\Pi_2|\zeta l_i.s_i|{}^3\Delta_2\rangle = \sqrt{(1/2}\ \zeta$

$\langle {}^3\Pi_2|\zeta l_i.s_i|{}^1\Delta_2\rangle = \sqrt{(1/2}\ \zeta$

The origins of the states were taken to be the deperturbed term values of Dufour et al with the first order spin-orbit term for the $^3\Pi$ state included, ie $^3\Pi_0 = {}^3\Pi+\frac{1}{2}\zeta$, $^3\Pi_2 = {}^3\Pi-\frac{1}{2}\zeta$. The value for ζ the spin-orbit parameter for a Cu 3d electron was taken as 747.31 cm^{-1}, the value obtained by Dufour et al when fitting the band origins rather than the atomic value of 824 cm^{-1} the corrections to the energies of the $^3\Pi$ components are then given by second-order perturbation theory as

$$E^{(2)} = \langle \mathcal{H}so\rangle^2/(E\pi-Ep) \qquad 5.5$$

where Ep is the energy of the perturbing level. Thus lower lying levels will push the $^3\Pi$ components up and higher levels will push them down figure 1 shows the positions of the states involved relative to the $X^1\Sigma^+$ state. The positions of the $^3\Pi$ components are

$^3\Pi_{o+} = -A + 2/3\lambda - o$

$^3\Pi_{o-} = -A + 2/3\lambda + o$

$^3\Pi_1 = -4/3\lambda$

$^3\Pi_2 = A + 2/3\lambda$

which give

$A = {}^3\Pi_2 - 1/2({}^3\Pi_{o+}+{}^3\Pi_{o-})$

$\lambda = 3/8({}^3\Pi_{o+}+{}^3\Pi_{o-}) + 3/4{}^3\Pi_2$ or $-3/4{}^3\Pi_1$

$o = 1/2({}^3\Pi_{o-}-{}^3\Pi_{o+})$

Taking the combined effects of the seven terms gives the following values for the parameters (in cm^{-1}), including the first-order contribution to A.

$A = -345$
$\lambda = -221$
$o = 304$

This compares with the result of the final experimental fit.

$A = -413.16$
$\lambda = -18.79$
$o = 320$

These are not however the true experimental values, because the $^3\Pi_o$- state has not been observed, and it was chosen to consrain o to 320 cm^{-1}. The actual intervals determined are

$A + 2\lambda = -450.74$
$A - 2\lambda + o = -55.56$

and it is really only these intervals which can be compared, the calculated values being

$A + 2\lambda = -787$
$A - 2\lambda + o = 401$

Both values are some hundreds of wavenumbers out and it is clear that this is due to the value predicted for λ. The $^3\Pi_o$- sub-state is unlikely to be more than 200 cm^{-1} from its predicted position and this implies a maximum likely range for λ of between -44 and +6 cm^{-1}. Clearly the second order perturbation treatment is a very poor model for the spin-spin interaction, probably due to ignoring contributions which arise in third and higher order. The calculated value for A compares quite well with the current experimental result but this arises mainly from the first-order contribution the second-order terms virtually cancelling out. Once the $^3\Pi_o$- sub-band has been observed and the three parameters separated these values will be useful in more accurate calculations, as will the centrifugal distortion corrections A_D and λ_D which arise in third order in pertur-

bation theory.

It is also possible to make estimates of the two lambda doubling parameters determined p and q. To second order in perturbation theory there may be written as (19)

$$p = -4 \sum_{n'\lambda'\upsilon'} (E_{n\pi}-E_{n\Sigma})^{-1}(-)^{S}\langle\eta,\Lambda=1|BT_{+}^{1}(L)|\eta',\Lambda'=0\rangle \quad 5.6$$

$$\times\sum_{i}\langle\eta',\Lambda=0|T_{-}^{1}(a_i l_i)|\eta,\Lambda=1\rangle\langle S||T^{1}(s_i)||S\rangle[S(S+1)(2S+1)]^{-1/2}$$

$$q = 4 \sum_{n'\lambda'\upsilon'} (E_{n\pi}-E_{n\Sigma})^{-1}(-)^{S}|\langle\eta,\Lambda=1|BT_{+}^{1}(L)|\eta',\Lambda=0\rangle|^{2} \quad 5.7$$

The summations are performed over the vibrational levels υ' of $^3\Sigma$ electronic states (η') and s is even or odd for $^3\Sigma^+$ or $^3\Sigma^-$ states respectively. Although the experimentally determined parameters contain contributions from third and higher orders, it is expected that these terms provide the dominant contributions. Several approximations are required to make these expressions readily calculable. The averaging over all vibrational levels is unlikely to effect the result at the accuracy required, and the expectation values can be fairly simply represented using the pure precession model (29) for which either the total L or partial l orbital angular momentum is conserved. The only state producing lambda doubling is the $a^3\Sigma^+$ state and as the orbitals concerned have the n and l value as discussed above the expectation values reduce to

$$-2^{-1/2}B\langle\pi^3\sigma^2 4s\sigma^1|L_+|\pi^4\sigma^1 4s\sigma^1\rangle = -2^{-1/2}B(l(l+1))^{1/2}$$

as l = 2 for a 3d electron $= -\sqrt{3}B$

giving $q = 12B^2/(E_\pi-E_\Sigma) = 0.00057\ cm^{-1}$

The orbital terms for p also reduce to similar expressions and the reduced spin matrix element is given by Brown and Merer (19) as $(3/2)^{1/2}$ giving

$$p = -6aB/(E_\pi-E_\Sigma) = -0.572\ cm^{-1}$$

with $a = \zeta = 747.3\ cm^{-1}$ from Dufour et al (8). The experimental values with 95% confidence limit are

$$p = -0.59\ (4)\ cm^{-1} \qquad q = 0.00029\ (6)\ cm^{-1}$$

which compare quite well especially p. The experimental values although reasonably well determined are also quite highly correlated and thus it is possible to make changes to them provided compensating changes are made to the others, however it is unlikely that they are wrong by more than twice the error quoted above. Thus the discrepancy is probably due to the approximations made in the calculations together with the neglect of third and higher order contributions.

The spin-rotation interaction γ can also be calculated in a similar way and to second order has been shown by Brown and Merer (19) to be given by

$$\gamma = -\tfrac{1}{2}p \qquad 5.8$$

when the only perturbing state is $^3\Sigma^+$. This gives

$\gamma = 0.286$ compared with $\gamma = 0.31\ (4)\ cm^{-1}$ from experiment

Again this is in very good agreement and as the two experimental values agree with this formula, it shows that any third order terms which might cause deviation from this relationship must be small, it also shows that other electronic states do not make significant contributions to these terms.

Although the fine structure constants have provided some information on the nature of the orbitals involved in the $b^3\Pi$ state of CuF, the hyperfine effects which are a more precise probe of the nature of the electron distribution are of rather more importance. As has been said before the main contribution to the $^3\Pi$ state arises from the ionic configuration $Cu^+(3d^94s^1)F^-(2p^6)$ but there are also likely

to be important contributions from two possible atomic configurations

$$Cu[3d(\delta^4\pi^4\sigma^2)4s\sigma]F[2p(\pi^3\sigma^2)]$$
$$Cu[3d(\delta^4\pi^3\sigma^2)4s\sigma^2[F[2p(\pi^4\sigma)]$$

Of these the first is likely to be the most important as it comes from the same $Cu(3d^{10}4s^1)F(2p^5)$ configuration which contributes to the ground state. Dipole moment measurements (15) suggest a charge separation of 70% in the ground state using a simple Cu^+F^- model for the ionic molecule. The atomic configuration for the $X^1\Sigma^+$ state is quite strongly bonding however as both unpaired electrons lie in σ type orbitals, whereas in the excited state the unpaired electron on the fluorine atom must lie in a π type orbital. This configuration is non-bonding hence the ionic configuration will be relatively more important in the excited state.

Hyperfine structure for the copper nucleus arises from the following sources: the Fermi contact term b_F due to the unpaired electron in the 4s orbital; and the nuclear spin orbit term a, the spin dipolar term c and the lambda doubling spin-dipolar term d due to the unpaired electron in the $3d\pi$ orbital. As only the ionic configuration, of the two being considered, contains a $3d\pi$ electron, sufficiently accurate calculations should indicate the relative proportions of each involved.

The values of the parameters may be calculated from the following expressions (20,21)

$$a/cm^{-1} = \mu_o/4\pi hc \sum_i 2\mu_B g_N \mu_N \langle 1/r_i^3 \rangle \qquad 5.9$$

$$b_F/cm^{-1} = \mu_o/hc \sum_i (2/3) g_i \mu_B g_N \mu_N \langle \delta(r_i) \rangle \qquad 5.10$$

$$c/cm^{-1} = \mu_o/4\pi hc \sum_i (3/2) g_i \mu_B g_N \mu_N \langle (3\cos^2\theta_i - 1)/r^3 \rangle \qquad 5.11$$

$$d/cm^{-1} = \mu_o/4\pi hc \sum_i (3/2) g_i \mu_B g_N \mu_N \langle (\sin^2\theta_i)/r^3 \rangle \qquad 5.12$$

where μ_B and μ_N are the Bohr and nuclear magnetons respectively, g_N is the nuclear spin g factor, and g_i is the electron spin g factor for each open shell electron i, over which the summation is taken. μ_o is the permeability of free space and r_i and θ_i are the spherical polar coordinates of the unpaired electrons. For the above expressions to be of any use it is necessary to have reasonably accurate values for the expectaion values. An estimate of the unpaired spin density at the copper nucleus can be made from the results of experiments on the optical spectrum of the copper atom (22). In its ground state the Cu atom has one unpaired electron in the 4s orbital. This gives a $^2S_{1/2}$ state where the splitting of the two hyperfine components F=1 and F=2 is found to be 0.390 cm^{-1}. As the energies are given by $b_F/2(F(F+1)-J(J+1)-I(I+1))$ this is equal to $2b_F$ for the atom, resulting in b_F = 0.195 cm^{-1}. Since the single electron in the $4s\sigma$ orbital is responsible for only half the spin angular momentum in the $^3\Pi$ state, the parameter b_F is estimated to be 0.098 cm^{-1}.

To evaluate the other parameters it is necessary to have an estimate of $\langle 1/r^3 \rangle$ for a Cu 3d electron, this can again be made from the copper atom data. From Townes and Schawlow (23)

$$a_A \approx l(l+1)/j(j+1)a_M \qquad 5.13$$

where a_A is the nuclear-spin orbit term for the atom and a_M is the expression for the molecule given in equation 5.9. In the $^2D_{3/2}$ state the splitting between the F=3 and F=0 levels is 0.360 = $6a_A$ from the energy expression used previously, this gives a_M = 0.0375 cm^{-1}. In the $^2D_{5/2}$ state the splitting between the F=4 and F=1 levels is 0.198 = $9a_A$ giving a_M = 0.0321 cm^{-1}. Taking the mean of these gives the following value for the nuclear-spin orbit interaction for a Cu 3d electron

$$a = 0.035 \ cm^{-1}$$

As the 3dπ electron gives rise to all of the orbital angular momentum, it is not necessary in this case to divide by 2.

The angular expectation value for a 3d electron is given (24) by

$$\langle 3d\pi|3\cos^2\theta-1|3d\pi\rangle = 5/2\pi\iint C^*_{21}C_{20}C_{21}d\theta d\phi \qquad 5.14$$
$$= -5/2\pi\iint C_{21}C_{20}C_{21}d\theta d\phi$$

$$= 10\begin{pmatrix}2 & 2 & 2\\ 1 & 0 & -1\end{pmatrix}\begin{pmatrix}2 & 2 & 2\\ 0 & 0 & 0\end{pmatrix} = 2/7$$

This gives c = 0.015 cm^{-1}. But as this electron contributes only half of the spin in the molecule the value should be divided by 2 giving

$$c = 0.0075\ cm^{-1}.$$

The value for $\langle\sin^2\theta\rangle$ may be calculated in the same way to give $\langle\sin^2\theta\rangle = 4/7$. The calculated value for d should also be reduced by a factor of 2 giving

$$d = 0.015\ cm^{-1}.$$

It was not possible experimentally to determine all of the parameters as the combination b+c produces effects only in the $^3\Pi_2$ branch where no hyperfine structure was observed. Although the data were fitted to b_F with c constrained to an estimated value of 0.0064 cm^{-1}, the determinable parameter is b thus the three values found experimentally are

$$a = 0.027\ (9)$$
$$b = 0.131\ (14)$$
$$d = -0.059\ (14)$$

The nuclear spin orbit term which depends only on the expectation value of $1/r^3$ for the orbital motion of the electron, is likely to be fairly well characterised by the theoretical expression. Hence it can be used to obtain an approximate value for the amount of ionic character in the

Figure 13. Computer simulation of the copper and fluorine hyperfine structure in the $^3\pi_{0+}$ sub-state. The pattern was determined by evaluating the energy levels using the parameters from the final least squares fit of the experimental data, and then subtracting the energies which result from setting all the hyperfine parameters to zero. The splittings for both nuclei increase slowly from zero to reach a limiting value determined by b + d.

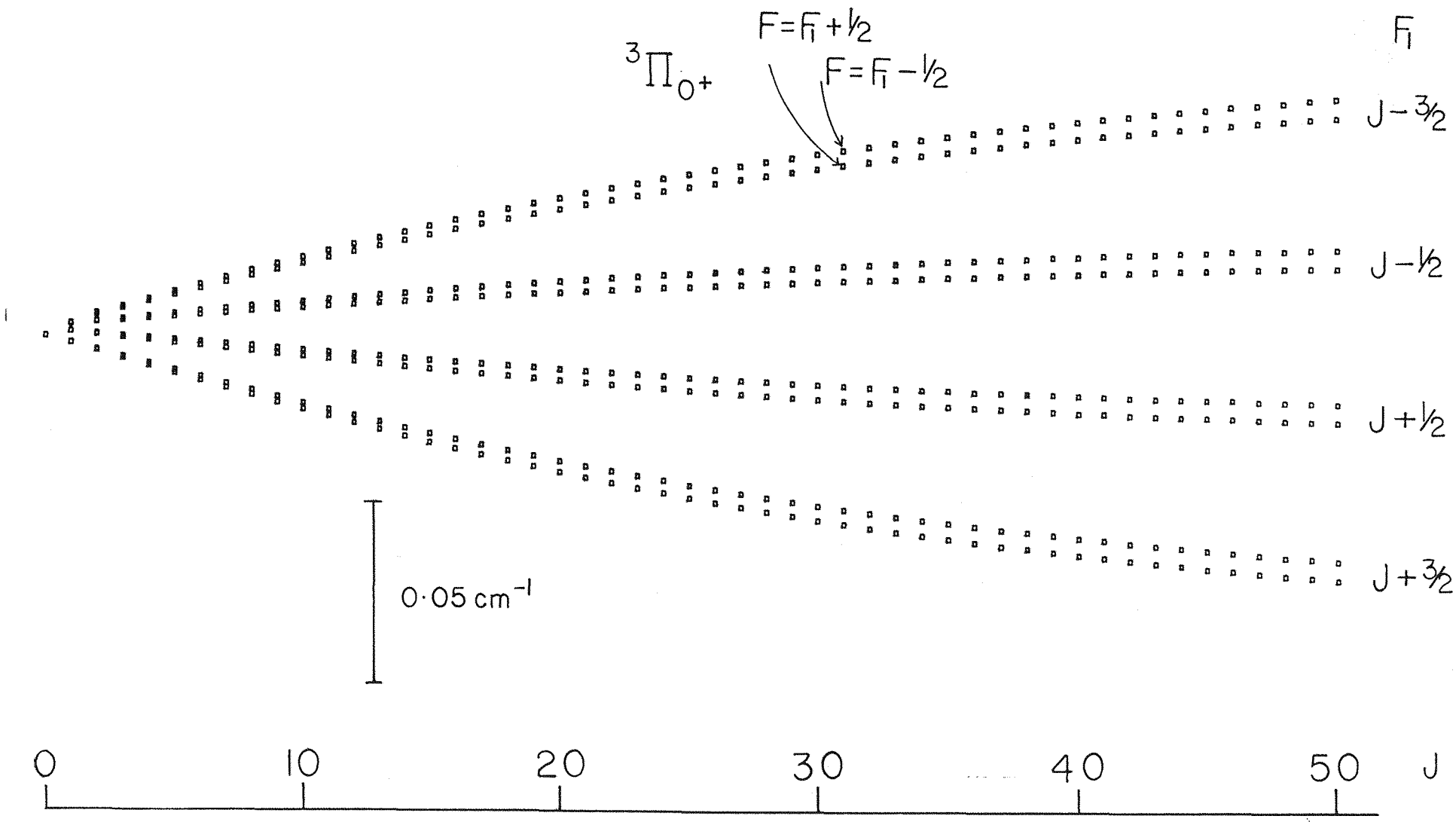
$^3\Pi_{0^+}$
$F = F_1 + 1/2$
$F = F_1 - 1/2$
F_1
$J - 3/2$
$J - 1/2$
$J + 1/2$
$J + 3/2$
0·05 cm^{-1}
0
10
20
30
40
50
J

Figure 14. Computer plot of the hyperfine structure in the $^3\Pi_{1+}$ sub-state. The splitting starts off large at low J, due to the nuclear spin-orbit term a, becomes smaller and then splits again due to b + d and b. The final splitting is slightly smaller than in the $^3\Pi_{0+}$ sub-state because of the term in b which couples the $^3\Pi_{1+}$ and $^3\Pi_{2+}$ sub-states.

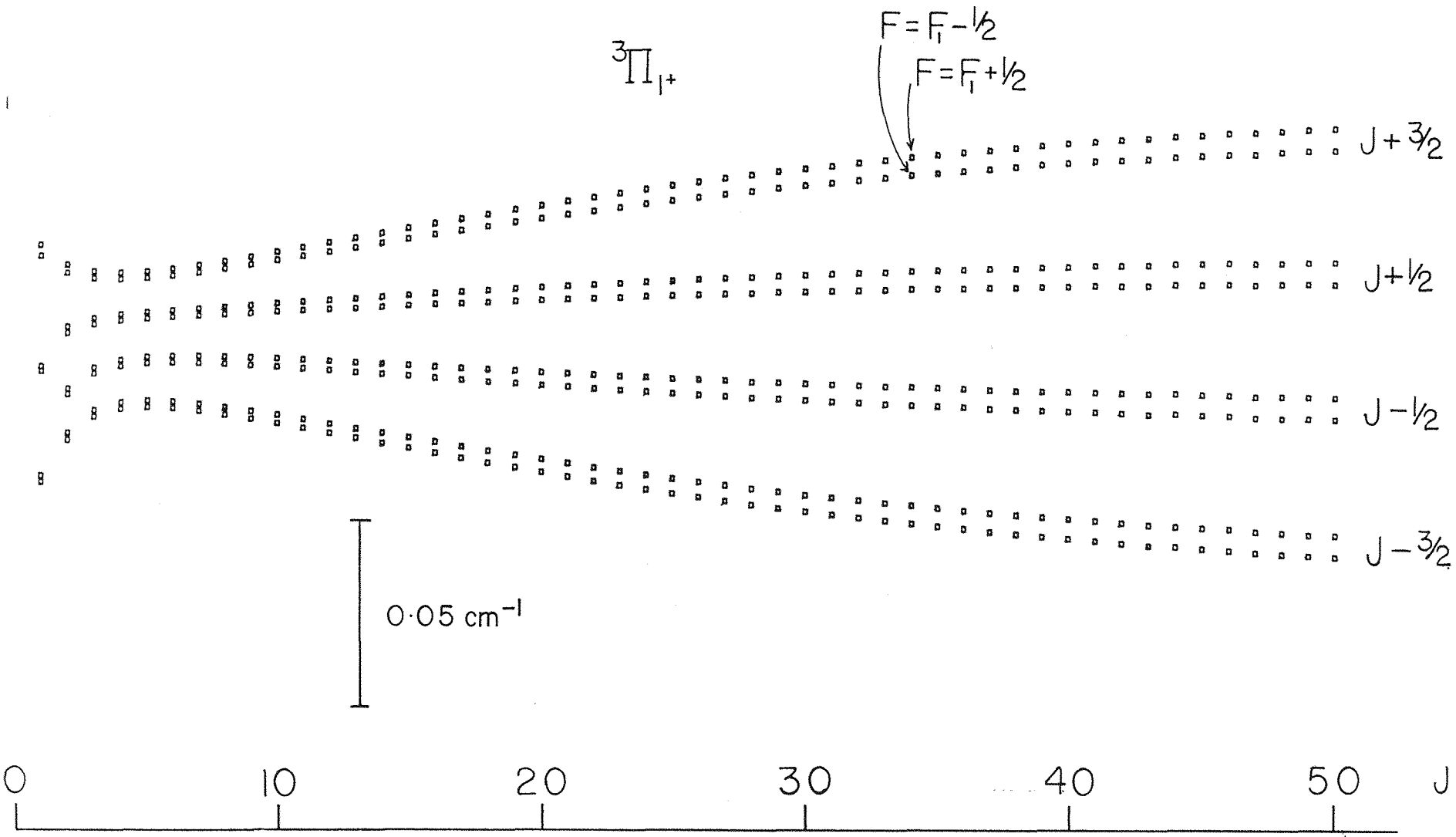
$^3\Pi_{1^+}$
$F = F_1 - 1/2$
$F = F_1 + 1/2$
J + 3/2
J + 1/2
J − 1/2
J − 3/2
0·05 cm^{-1}
0
10
20
30
40
50
J

Figure 15. Computer simulation of hyperfine structure in the $^3\Pi_{1-}$ sub-state. As no fluorine splittings were observed for this sub-state, the contributions due to the fluorine nucleus are not included. While such effects may be quite large at low J they decrease rapidly with increasing J as the fluorine nucleus has no electric quadrupole moment to give splittings similar to those seen for copper at high J. The four rotational lines observed are marked in and it can be seen that the asymmetry shown in figure 9 is correctly reproduced, together with the two overlapping components for $Q_1(19)$ and $Q_1(21)$.

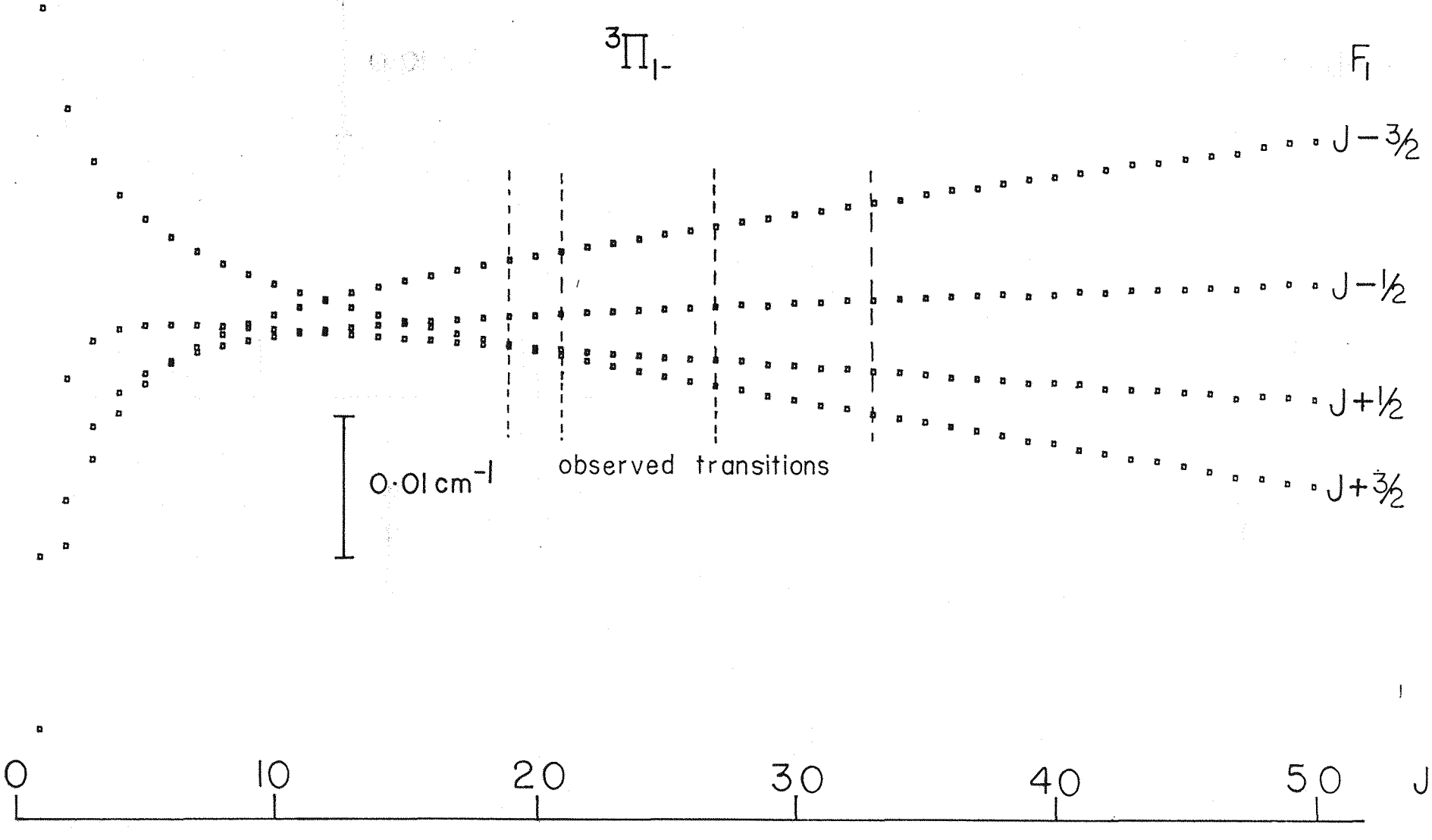
$^3\Pi_{1-}$
F_1
J−3/2
J−1/2
J+1/2
J+3/2
0·01 cm^{-1}
observed transitions
0
10
20
30
40
50
J

Figure 16. Hyperfine structure in the $^3\pi_{1-}$ sub-state when d for the copper nucleus is positive, b + d being kept fixed to the experimentally determined value. The observed transitions are marked in, and comparison with figure 9 shows that this simulation bears no similarity to the observed splittings.

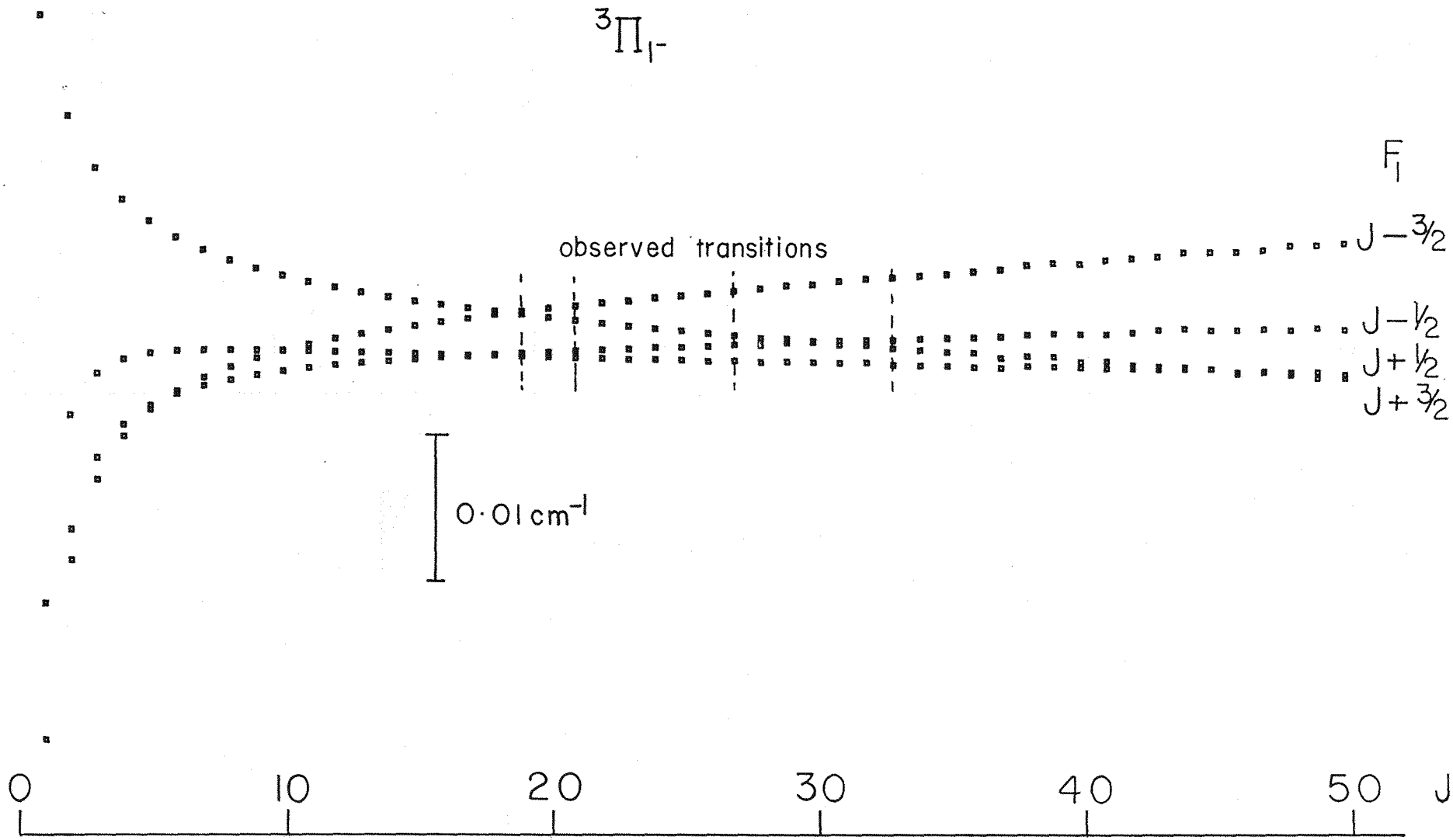
$^3\Pi_1$-
F_1
observed transitions
J − 3/2
J − 1/2
J + 1/2
J + 3/2
0·01 cm^{-1}
0
10
20
30
40
50
J

excited state as the predominant atomic configuration does not contribute to this term.

This gives the ionic contribution as 78% but the error is quite large due to the inaccuracy in the fitted value for a. As was explained earlier it seems likely that the ionic character of the excited state should be slightly greater than the ground state and this is consistent with the value found in the $a^3\Sigma^+$ state of 85% (6).

Assuming 70% ionic character the d parameter is calculated to be $0.012cm^{-1}$, but this is in total disagreement with the experimentally determined value of $-0.059\ cm^{-1}$. Initially it was thought that there must have been some mistake, and the matrix elements were checked carefully to make sure that the correct sign was being used in the expressions. The actual parameters determined are b+d and b-d, the former arising from the $^3\Pi_{0^+}$ and $^3\Pi_{1^+}$ results and the latter from the $^3\Pi_{1^-}$ data. Figure 13 shows the splitting of the hyperfine components in the $^3\Pi_{0^+}$ state with fluorine effects included, and figure 14 shows the structure in the $^3\Pi_{1^+}$ state. It was perfectly possible to reproduce the $^3\Pi_{0^+}$ and $^3\Pi_{1^+}$ splittings with d positive, simply by changing b, but this produced a large change in b-d from the fitted value which altered the structure in the $^3\Pi_{1^-}$ branch. The behaviour of the four copper hyperfine components, as J varies, is shown in figure 15. The strong asymmetry observed in the IMF spectra of this branch is clearly reproduced, as is the overlapping of the two lowest lying components at about J=20. This behaviour results from a combination of three effects; the nuclear spin orbit term which produces the low J splitting; and the eq_2Q and b-d terms which lead to the asymmetry and spreading out of the pattern of lines. If b-d is changed so as to give a positive d value then the behaviour is quite different principally because the crossover of the four components no longer occurs at low J. This is especially true of the $F = J + 3/2$ component which, as can be seen from figure 16 does not complete its crossing until after $J = 50$. All attempts at varying the value for eq_2Q and b-d with d small

and positive failed to give hyperfine structure which was in any way similar to the observed splittings in the IMF lines. Thus it must be assumed that the value determined is correct, but it is not easy to see how it can arise. The value of $\langle 1/r^3 \rangle_{spin}$ is likely to be fairly similar to $\langle 1/r^3 \rangle_{orbit}$ which gives a satisfactory value for a. Similarly the value of $\langle \sin^2\theta \rangle$ must be positive hence the expression for d cannot be a good representation of the interaction actually occurring. This formulation is based on a simple first order coupling between the nuclear and electron spins however effects mimicking this can arise in second order via spin-orbit coupling of the nuclear spin to the electron orbital motion then to the electron spin angular momentum. This leads to mixing with other electronic states arising from the $Cu^+(3d^94s^1)F^-(2p^6)$ configuration. The calculations by Dufour et al (8) have already shown that there is significant mixing between the different states. Unfortunately no calculations have been made of the effect of these terms on the hyperfine parameters. The contribution of these terms to d must be large as the calculated value is required to change from +0.012 to -0.059, ie they must be six times greater than the first order effects. While this result is not particularly satisfactory in terms of the simple model usually used to describe hyperfine effects, it is useful in showing the limitations of the model and should provide a good test of any calculations to higher order.

An experimental value for b_F can only be obtained by assuming a value for c, this was taken as 0.0064 cm^{-1}, while fitting the data. However, second order effects which contribute to d are also likely to have a significant effect on c, and this reduces the accuracy with which b_F may be estimated. Although no evidence of hyperfine structure was observed in the $^3\Pi_2$ branch while the recordings were being made, it can be seen from figure 17 that the hyperfine effects should produce some observable increase in linewidth. Most of the lines in the $^3\Pi_2 - {}^1\Sigma^+$ sub-system do not have sufficient signal to noise for the linewidth to be determined accurately however the sequence of lines shown in

Figure 17. Approximation of the, so far unobserved, hyperfine structure in the $^3\Pi_2$ sub-state. The high J splitting, which is determined by b for both nuclei is accurately predicted by the results for the other sub-states. The large splitting at low J in the simulation arises from b+c and while for copper this term is dominated by b, which is known, the fluorine splitting is based wholely on calculated parameters, and hence is highly speculative. It is unfortunate that lines below J of 20 were too weak to be observed for this sub-band , as they would probably show copper hyperfine structure, at Doppler-limited resolution, and hence give a value for the spin dipolar parameter c.

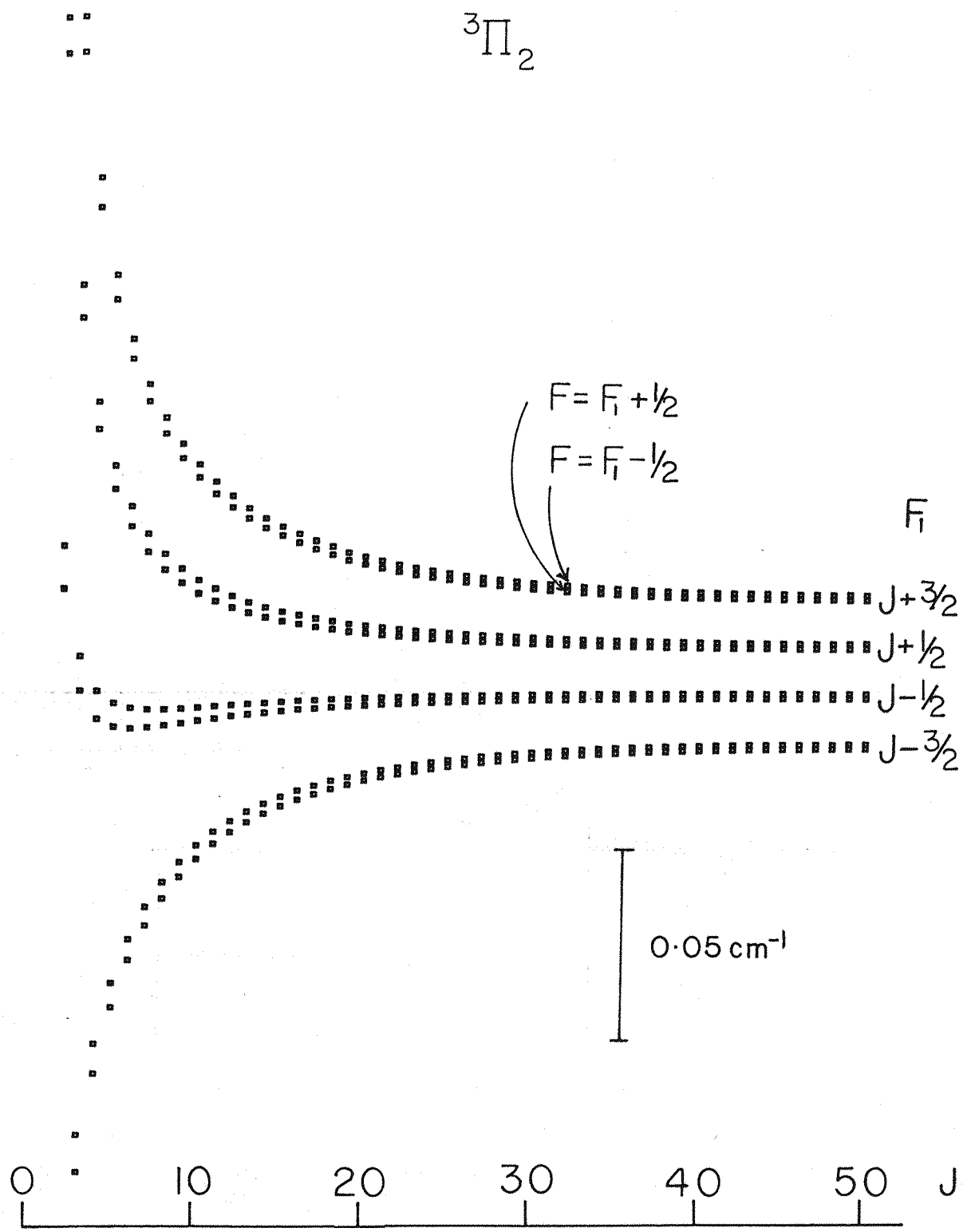
$^3\Pi_2$
$F = F_1 + 1/2$
$F = F_1 - 1/2$
F_1
$J+3/2$
$J+1/2$
$J-1/2$
$J-3/2$
0·05 cm^{-1}
0
10
20
30
40
50
J

figure 6 were sufficiently strong to allow a reasonable determination. The measured linewidths for selected lines in this region (in GHz) are

$Q_2(58)$	1.79
$Q_2(55)$	1.77
$Q_2(52)$	1.83
$Q_2(49)$	1.93
$Q_2(46)$	1.97

To obtain an accurate estimate of the variation of linewidth with b+c a program was written to convolute the components assuming a Gaussian lineshape with a Doppler FWHM of 1.02 GHz. The set of best fit parameters gave a FWHM for $Q_2(50)$ of 1.63 GHz, varying only slightly with J. A value of 0.19 cm^{-1} for b+c was required to produce a linewidth comparable to those determined from the spectra. However there is an additional contribution to the lineshape from the ^{65}CuF isotopic species. The lines from this must lie under the observed signals as they are not visible in the spectrum, and are probably the cause of the rather large variation in the measured linewidth with J, as their positions change relative to the main lines. Thus it is not possible to obtain an accurate value for b+c from these calculations but a range within which it must lie can be estimated. Taking the measured value of b = 0.131 cm^{-1}, c must be small and positive with a minimum of about 0.01 cm^{-1}, and a maximum of about 0.04 cm^{-1}. These values correspond to b_F = 0.135 cm^{-1} and 0.145 cm^{-1} respectively.

The calculated b_F for one electron in a copper atom 4s orbital is 0.095 cm^{-1}, but the value for CuF is likely to be somewhat greater as the main configuration is ionic, and the greater effective charge is likely to result in a higher spin density at the nucleus. A reasonable value is probably about 0.11 cm^{-1} which is in agreement with the result for the $a^3\Sigma^+$ state of 0.108 cm^{-1}, the discrepancy may result from the fairly poor accuracy with which b-d is determined from the $^3\Pi_1$- sub-band although this is unlikely to account

for all of the error.

The quadrupole constants are even harder to estimate accurately than the magnetic hyperfine parameters as they depend on all the electrons in the molecule not just the valence electrons. However the effects due to unpaired electrons very often predominate, and these are also somewhat easier to estimate. In the ground state of CuF the value of eq_0Q is 22 MHz (16) and as there are no unpaired electrons which can contribute to this, it provides a reasonable estimate of the effects due to the distortion of the closed shells of electrons around the nucleus, and the charge distribution due to the fluorine nucleus. The experimentally determined quadrupole constants in the $^3\Pi$ state are

$$eq_0Q = -9\ (9)\ \text{MHz}$$
$$eq_2Q = 445\ (43)\ \text{MHz}$$

The change in eq_0Q can be interpreted as due mainly to the presence of an unpaired $3d\pi$ electron, which assuming the other effects remain the same, a somewhat risky assumption as the effect of promoting an electron from the 3d orbital to the 4s is likely to change the shape of the electron distribution, should contribute about -30 MHz to eq_0Q. To a first approximation eq_0Q is given (23) by

$$eq_0Q = eQ(2l(l+1)/(2l-1)(2l+3))e\langle 1/r^3\rangle \qquad 5.15$$

Taking $Q = -0.18\times10^{-28}$ m^2 (25) and $\langle 1/r^3\rangle$ from the magnetic hyperfine calculations gives

$$eq_0Q = -180\ \text{MHz}$$

This is somewhat larger than expected but considering the approximations necessary is not unreasonable. Similar calculations for eq_2Q give

$$eq_2Q = -360\ \text{MHz}$$

which is in total disagreement. However this depends on $\langle \sin^2\theta \rangle$ and as has been seen for d, the calculated values dependent on this term for a $3d\pi$ electron are rather inaccurate. The fact that the same disagreement occurs for both of the values dependent on $\langle \sin^2\theta \rangle$ implies a common cause for the problem.

Interpretation of the F hyperfine parameters is somewhat difficult as experimentally only a and b+d could be determined, the values being

$$a = 0.005\ (6)\ cm^{-1}$$
$$b+d = 0.00926\ (40)\ cm^{-1}$$

Using the value for $\langle 1/r^3 \rangle$ from Ayscough (26) gives $a = 0.059\ cm^{-1}$ for a single electron in a $F(2p\pi)$ orbital. As only the atomic configuration contributes to this term, it suggests only about 10% covalent character, however the rather large error on this value means that it is not inconsistent with the previously estimated 22% covalent contribution. To obtain anything from the other parameter combination it is necessary to assume the calculated values for $\langle 3\cos^2\theta-1 \rangle$ and $\langle \sin^2\theta \rangle$ of -2/5 and 4/5 respectively. These give c and d as follows, assuming 22% covalent character

$$c = -0.007\ cm^{-1}$$
$$d = 0.014\ cm^{-1}$$

Taking these values gives b_F small and negative, but if say 10% covalent character were taken then b_F would be small and positive. Hence it is not possible to make any sensible estimate of the individual parameters making up b+d.

5.6 Conclusion

Despite the transition involved being singlet-triplet and thus quite strongly forbidden it has proved fairly easy to measure LIF transitions for CuF $^3\Pi - X^1\Sigma^+$ with very good signal to noise. It has also been possible to observe double resonance and saturation signals which require much stronger optical transitions. This is an indication of the very high sensitivity which can be achieved using fluorescence detection. The observation of the strongly forbidden $\Delta\Omega = 2$ $^3\Pi_2 - {}^1\Sigma^+$ sub-band has resulted in a conclusive assignment of this system. It has proved possible to reproduce all the observed structure in the spectra and obtain from this a set of effective Hamiltonian parameters. Unfortunately it has not been possible to interpret all of these in terms of the electronic configurations which may contribute to the $b^3\Pi$ state.

Although this study has been fairly extensive, covering both fine and hyperfine structure in five of the six sub-bands there still remains some work to do. All the measurements possible with the current laser system have been made and any further experiments would require the additional power available from a ring dye laser, about 1 Watt or greater in this frequency region. This would make observation of the $^3\Pi_{0^-} - {}^1\Sigma^+$ sub-band quite easy and would allow extension of the $^3\Pi_2$ measurements to lower rotational levels, possibly resulting in the resolution of copper hyperfine effects from under the Doppler profile. Double resonance and IMF experiments because of their requirement for at least partial saturation tend to increase in signal to noise at a rate, at least linear in laser power. This would make possible the observation of IMF signals at much lower J than before, yielding additional information on the hyperfine structure, and similarly MODR signals, previously observed with great difficulty or not at all, would become quite strong and allow the determination of both fluorine and copper hyperfine effects for the first rotational levels in the $\Omega = 1^+$ and 1^- sub-levels.

Together these results would lead to a full set of hyperfine parameters for both nuclei and would hopefully remove the ambiguities in the current measurements. More extensive theoretical calculations both on CuF and the nature of hyperfine effects are clearly required in order to explain fully the effects seen so far.

References

1. L.H.Woods, Phys. Rev. **64**, 259-264 (1943).
2. S.E.Johnson, P.B.Scott and G.Watson, J. Chem. Phys. **61**, 2834-2839 (1974).
3. R.E.Steele and H.P.Broida, J. Chem. Phys. 69, 2300-2305 (1978).
4. R.W.Schwenz and J.M.Parsen, J. Chem. Phys. 73, 259-267 (1980).
5. F.Ahmed, R.F.Barrow, A.H.Chojnicki, C.Dufour and J.Schamps, J. Phys. B, **15**, 3801-3818 (1982).
6. C.R.Brazier, J.M.Brown and M.Purnell, J. Mol. Spectrosc. **99**, 279-287 (1983).
7. T.C.Steimle, C.R.Brazier and J.M.Brown, J. Mol. Spectrosc. **91**, 137-149 (1982).
8. J.Schamps, private communication 1981 and C.Dufour, J.Schamps and R.F.Barrow, J. Phys. B, **15**, 3819-3828 (1982).
9. T.C.James, J. Mol. Spectrosc. **40**, 545-553 (1971).
10. S.W.Chalkley, Ph.D.Thesis, Southampton University, 1980.
11. C.R.Brazier, J.M.Brown and T.C.Steimle, J. Mol. Spectrosc. **97**, 449-453 (1983).
12. J.B.West, R.S.Bradford Jr, J.D.Eversole and C.R.Jones, Rev. Sci. Instrum. **46**, 164-167 (1975).
13. S.Gerstenkorn and P.Luc, "Atlas du spectrum d'absorption de la molecule d'iode", CNRS, Paris, 1978.
14. S.Gerstenkorn and P.Luc, Rev. Phys. Appl. **14**, 791-796 (1979).
15. J.Hoeft, F.J.Lovas, E.Tiemann and T.Torring, Z. Naturforsch, **25a**, 35-39 (1970).
16. R.Honerjager and R.Tischer, Z. Naturforsch, **29a**, 1919-1921 (1974).
17. J.M.Brown, I.Kopp, C.Malmberg and B.Rydh, Physica Scripta, **17**, 55-67 (1978).
18. R.M.Lees, J. Mol. Spectrosc. **47**, 286-296 (1973).
19. J.M.Brown and A.J.Merer, J. Mol. Spectrosc. **74**, 488-494 (1979).
20. R.A.Frosch and H.M.Foley, Phys. Rev. **88**, 1337-1349

(1952).
21. G.C.Doumanis, Phys. Rev. 17, 967-970 (1955).
22. R.Ritschel, Z. Phys. 71, 1-22 (1932).
23. C.H.Townes and A.L.Schawlow, "Microwave Spectroscopy", McCraw-Hill, New York, 1955.
24. D.M.Brink and G.R.Satchler, "Angular Momentum", Oxford University Press, 1968.
25. "Handbook of Chemistry and Physics", 51st edition, The Chemical Rubber Company, 1971.
26. P.B.Ayscough, "Electron Spin Resonance in Chemistry", Methuen, London, 1967, Appendix 3.

Chapter 6 The $X^2\Pi$ and $A^2\Delta$ states of CH

6.1 Introduction

There has been much interest in the CH free radical in recent years particularly in the nature of the lambda doubling and hyperfine effects in the ground $X^2\Pi$ state. Initially the only information available was the optical spectrum obtained at moderate resolution from grating spectrographic studies. The first measurements were by Gero (1) in 1941 of the $A^2\Delta - X^2\Pi$ band at 431.5 nm and although not particularly accurate they were useful in the present work as an indication of where to look for each line. Subsequent work was carried out by Keiss and Broida (2) on the (0,1) and (1,2) bands of the $A^2\Delta - X^2\Pi$ system and by Herzberg and Johns (3) on transitions involving the higher electronic states. The (0,0) band of the $A^2\Delta - X^2\Pi$ system was remeasured by Douglas and Elliott (4) in order to obtain improved ground state term values.

The main reason for this great interest was the possibility of detecting CH in astrophysical sources. The lambda doubling in the lowest F_2 $J=½$ level was estimated at about 3.4 GHz, a readily accessible frequency for interstellar microwave detection. The first direct ground state measurements in CH were made by Evenson et al (5) in 1971 using the technique of far infrared laser magnetic resonance but this involved excited rotational levels and thus gave little improvement in accuracy for the 3.4 GHz transition. However, before more direct laboratory measurements could be made, the three hyperfine components of the 3.4 GHz lambda doubling transition were observed in interstellar gas clouds (6,7). Subsequent attempts to observe rotationally excited CH have been unsuccessful, and further laboratory measurements of ground state transitions have been attempted, in order to obtain better predictions for the lambda doubling splittings in the higher levels. These astronomical observations are important as they would give valuable information on the extent of rotational excitation of the

molecule in different environments. All attempts to observe the direct microwave spectrum have proved unsuccessful but several additional far-infrared LMR transitions have been observed (8,9) covering most of the low rotational levels and these were used to obtain predictions for the lambda doubling frequencies (10), good to a few MHz.

Although previous attempts to measure the ground state microwave spectrum had proved unsuccessful it was hoped that the greatly increased sensitivity of microwave optical double resonance (MODR) would make these signals quite easy to record. The LMR experiments had shown that CH could be produced in quite high concentration from the reaction between fluorine atoms and methane, and this was the method used in the present study. The laser induced fluorescence spectrum was recorded at the 1 cm^{-1} resolution obtainable from the dye laser when operated without intracavity etalons and the fluorescence found to be very strong, easily visible by eye. When the strong lines were examined at Doppler-limited resolution (FWHM = 2.5 GHz) they were found to have an almost immeasurably high signal to noise of at least 10000 to 1. To obtain accurate measurement of the dye laser frequency a heated tellurium cell was constructed to use in relation to the published atlas.

Due to the very strong optical transitions we were able to make the first laboratory recordings of the ground state microwave spectrum reasonably easily. A total of 18 transitions (11) in the N = 2,3 and 4 rotational levels were observed and these measurements accurate to about 0.1 MHz should prove very useful in future astronomical searches as they provide an improvement of more than an order of magnitude in accuracy over the previous indirect predictions. This data together with the astronomical lines and the lambda doubling spectra of higher rotational levels obtained by Bogey et al (12) were fitted to an esixting $^2\Pi$ program and an improved set of lambda doubling and hyperfine constants obtained.

While the measurement of the microwave spectrum was the initial aim of this work, we were also interested in

obtaining information on the $A^2\Delta$ state, about which little was known. The optical spectrum was recorded using IMF in order to resolve the hyperfine structure obscured below the Doppler profile. The observed doublet splittings were used to obtain a set of excited state hyperfine constants which are interpreted in terms of the possible electronic configurations leading to a $^2\Delta$ state. The 75 MHz free spectral range etalon used for measuring splittings was recalibrated by comparing IMF measurements of the lowest lambda doublets with those obtained from MODR. This value assumes negligible (less than 5 MHz) contribution due to lambda doubling in the $^2\Delta$ state. Calculations showed that this was reasonable for the lowest rotational levels but that at higher N the splitting would tend to increase rapidly reaching about 100 MHz at N=10. The usual method of measuring LIF signals, by interpolating between lines in the reference spectrum was found to be of insufficient accuracy for the determination of this effect. A system of measurement using the 75 MHz fringes was developed with the data recorded using a computer. A program was written to record the data and display the spectrum on the screen. Once the peaks to be measured were selected the frequency was then calculated by the computer using the fringes and the supplied Te_2 frequency. This resulted in much more accurate values for the line positions typically ± 0.001 cm^{-1} rather than ± 0.005 cm^{-1}. As the upper state lambda doubling increases as N^4, the very highest lines observable were measured to produce the maximum effect. Fortunately the ground state microwave measurements went to sufficiently high N to allow the determination of both first and second centrifugal distortion corrections to p and q and thus allow an accurate calculation of the predominant ground state contribution. When these were removed a set of upper state values showing a just significant splitting were obtained. Fitting of this data gave a value for the q parameter but p was not determinable.

An MODR experiment in the excited state was also performed in the hope of observing effects due to the lambda doubling, this involved a spin rotation transition but unfortunately no significant effects were obtained.

The remainder of this chapter consists of the experimental details and then separate sections on the ground and excited state measurements and analysis.

While this chapter was being written we learned of the first astrophysical observations of rotationally excited CH (13), the measured frequencies agreed with our calculations to within 10 kHz which gives an indication of the very high precision of these calculations. This also implies that more high N CH lines should be seen in the near future yielding important information on the extent of rotational excitation of CH in interstellar sources.

Figure 1. Schematic of the apparatus used for production of CH. A mixture of 2% F_2/He was passed through a microwave discharge to produce fluorine atoms which yielded CH from methane by succesive abstraction of protons. The laser beam was passed down the centre of the quartz reaction tube entering and exiting through Brewster's angle windows, and 3mm diameter apertures to reduce the amount of scattered light.

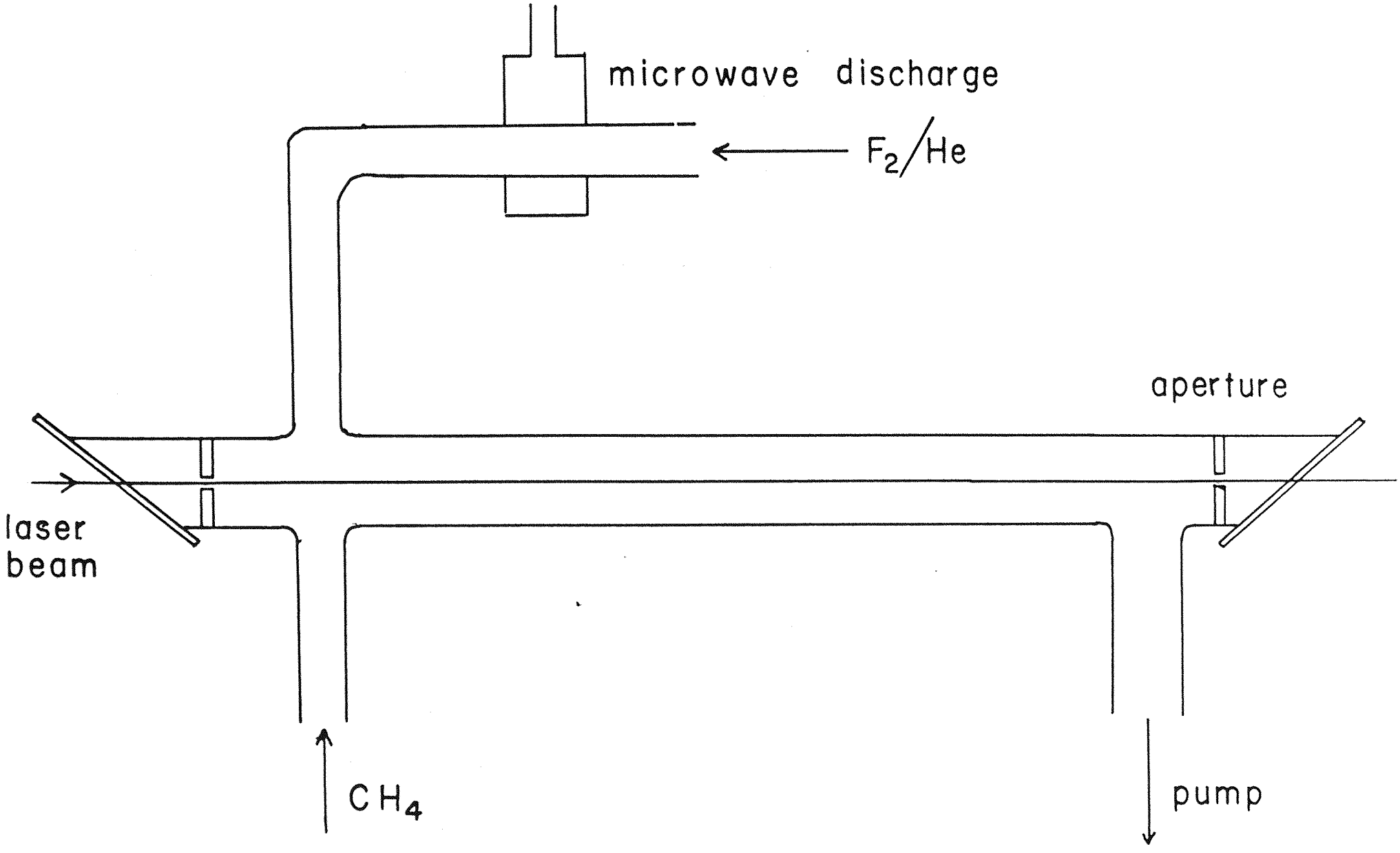
microwave discharge
F_2/He
aperture
laser beam
CH_4
pump

6.2 Experimental Details

The apparatus used in these experiments consists of a simple continuously pumped glass reaction cell and is shown in figure 1. Upto four gases may be mixed in the manifold before being passed through the microwave discharge, although for CH only one gas was used. This was usually 2% fluorine in helium although for some of the measurements CF_4 was used when no fluorine was available, the signal obtained was about the same in both cases, but F_2/He was preferable as the CF_4 discharge led to the production of other radicals with sprectra in the same region as CH. The best fluorine atom concentration was produced with a F_2/He pressure of about 400 mTorr and the microwave discharge operated at very low power. The fluorine atoms were passed into the cell, through a protective teflon tube to stop reactions with the grease on the joint, where they met the methane flowing from the opposite side arm. Two needle valves, one medium and one fine were used to reduce the flow of CH_4 to the very slow rate necessary for efficient production of CH. To start the reaction off initially, the F_2/He pressure was increased to about 1 Torr but after a few minutes this could be reduced to the pressure required. Once an LIF signal had been obtained the flow rates were adjusted to obtain the optimum amount of CH. When the reaction conditions were correct a milky blue chemilumenescence emanating primarily from excited CH was clearly visible.

The laser beam was passed along the centre of the reaction tube, entering and exiting via Brewster's angle windows with irises inside to reduce the amount of scattered laser light to a minimum. Two lenses were used to reduce the laser beam diameter to about 1 mm when it passed through the reaction region. When the laser was tuned to a CH transition a narrow rod of fluorescence was clearly visible where the laser beam passed through the chemilumenescence of the fluorine-methane reaction. The phototube was positioned perpendicular to the two inlet ports and a cylindrical lens was used to focus the fluorescence through a narrow slit and

Figure 2. Light collection scheme for the CH cell. Due to the large amount of chemilumenescence from the reaction, it was necessary to use a system of lenses and slits in order to preferentially image the laser induced fluorescence onto the detector. For MODR measurements the microwave radiation was emitted from a piece of waveguide butted against the side of the cell.

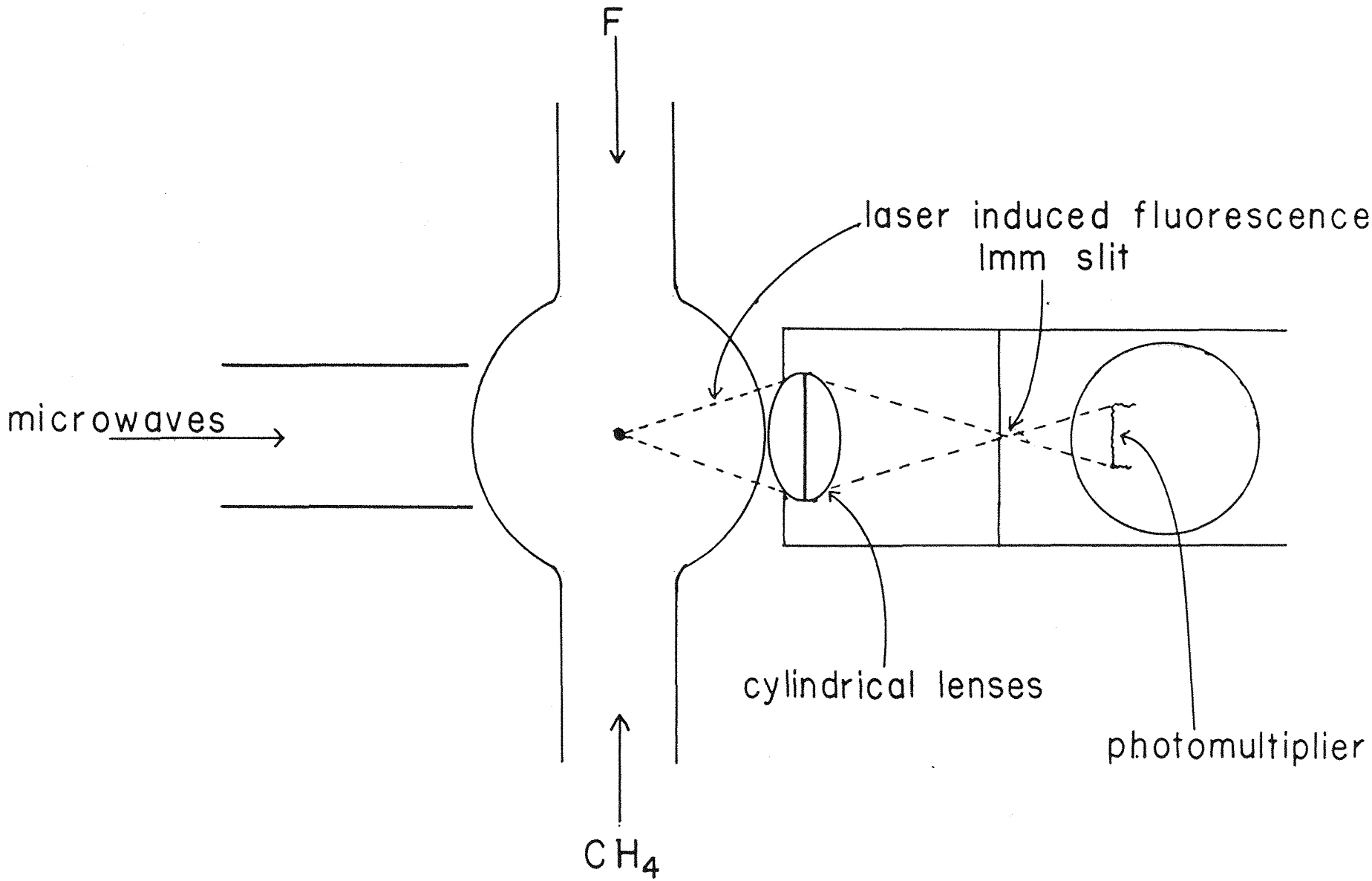
F
laser induced fluorescence
lmm slit
microwaves
cylindrical lenses
photomultiplier
CH_4

Figure 3. Schematic of the set-up for absolute frequency calibration by simultaneous recording of the spectrum of $^{130}Te_2$. The laser beam was split into two roughly equal components, one of which passed through the cell containing tellurium at 510°C. A differential amplifier was used to reduce effects due to laser power variation and the signal quality was also improved by chopping the laser beam and using a lock-in amplifier.

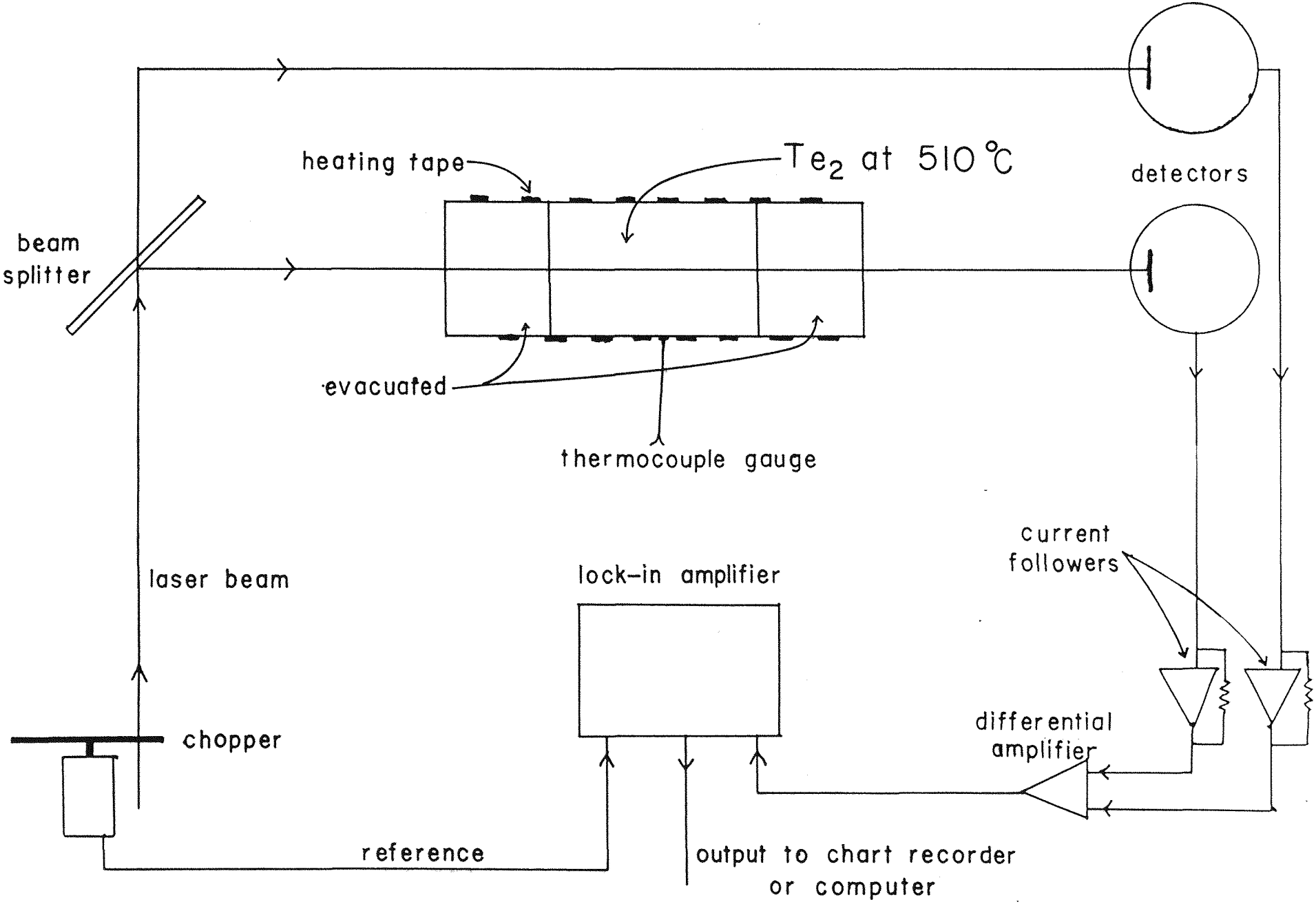
heating tape
Te_2 at 510 °C
detectors
beam splitter
evacuated
thermocouple gauge
laser beam
lock-in amplifier
current followers
chopper
differential amplifier
reference
output to chart recorder or computer

then, via a 70nm bandpass filter, centred at 450nm, onto the detector. A schematic of this arrangement is shown in figure 2.

The radiation source was a Coherent Radiation 599-21 standing wave dye laser pumped with 2 Watts all lines of the UV output of a Spectra-Physics 170 argon ion laser. The dye used was Stilbene 3 and the power obtained typically 40-60 mWatts, although the rate of decay was quite fast, necessitating dye changes about every 10 days, towards the end of the dye life only about 30 mWatts was obtained. It was possible to scan the laser over a range of about 30 GHz, although this was often reduced in order to obtain maximum power and stability. The single frequency jitter was somewhat greater than for the red dyes being about 4 MHz RMS but this was not a problem as the lowest signal linewidths achieved were 20 MHz FWHM. The laser radiation was amplitude modulated at about 900 Hz for the LIF measurements and a tuned lock-in amplifier used to improve the signal to noise.

In the red part of the visible spectrum the iodine atlas may be used for absolute frequency calibration, but this does not extend to the region of interest here, but an alternative atlas based on $^{130}Te_2$ (14) is available which covers the region from 17500 cm^{-1} to 23800 cm^{-1}. These spectra are recorded at a temperature of 500 ^{o}C or greater requiring a heated cell which makes recording the fluorescence more difficult. It has also been shown (15) that the fluorescence intensities do not match the absorption signals shown in the atlas particularly well, thus it was decided to record the spectra in absorption. In previous experiments with a heated iodine cell, we had experienced problems with deposition of the solid on the unheated end windows, which led to greatly increased noise due to scattering of the laser beam. It was therefore decided to use a three part cell with the two end sections evacuated completely and the centre one containing $^{130}Te_2$, this is shown in figure 3. Heating tape was wrapped around the cell and insulated with quartz wool, a thermocouple was placed under the heating tape so as to monitor the cell temper-

ature. The rate of heating could be varied by adjusting the voltage across the tape via a variac transformer, but once the correct temperature had been reached, it remained fairly steady without any electronic control of the heating through monitoring of the thermocouple.

To overcome the problem of laser power variation it was decided to use a difference amplifier and two laser beams, one passing through the cell, as shown in figure 3. The signal was monitored using photomultiplier tubes so only a very low power was required, this was about 50 μWatts in each beam, obtained by using the reflection off two successive glass plates, the radiation was passed through a beam splitter, and short focus lenses used to spread out the laser light before the detectors. Amplitude modulation and a lock-in amplifier were used to improve the signal to noise. The temperature, as measured by the thermocouple was varied until a good reproduction of the spectra in the atlas was obtained. Under these conditions signals with very little noise, and matching the atlas quite closely could be obtained.

When spectra with three tellurium lines were checked, it was found that the frequency sweep of the dye-laser was not particularly linear, this is a more serious problem when using the tellurium atlas as only 2 lines per cm^{-1} are measured compared with 4.5 lines per cm^{-1} for the iodine atlas. As a consequence only about two thirds of the lines in the CH spectrum could be measured by interpolation and for many of these the error was rather large as they lay some distance from tellerium lines, increasing the non-linearity error. Clearly the best way to overcome this problem would be to use the 75 MHz etalon to interpolate between the CH line and a tellerium line, also, as only one Te_2 line would be required per spectrum, virtually every line would be measurable. This method requires a three channel recorder and as the chart recorder was only two channel, it was decided to use the computer controlled data acquisition interface. A fairly rapid rate of recording was required in order to obtain a reasonable number, greater

than 10, of readings for each peak from the interferometer. A speed of about 1000 readings per second with the interferometer being recorded twice for each of the CH and Te_2 measurements, was found to be sufficient. To record a line the laser scan is adjusted to cover the required CH and Te_2 peaks and a single scan initiated at the same time as the data recording. The two spectra are then displayed on the computer screen.

Measurement of the position of the CH line is done by the computer. First the approximate peak of the signal is selected by moving the cursor onto it, from this the computer obtains a first estimate for the linewidth and intensity, as the baseline is not always zero it is necessary to select a sample of this in order to obtain a proper representation of the peak. The true line position is obtained by fitting the points on the top half of the peak to a Gaussian function, using a least squares routine. The top of the recalculated curve is taken as the peak centre, not the parameter for this returned from the fit. This is likely to give a more correct value, especially if the initial guess is not very good. The same procedure is then repeated to find the centre of the tellurium line. The fringes are counted by finding the turning points at the peaks of the lines, to avoid counting noise between the peaks the signal is only checked from just before where the top of the peak is expected. If the successive spacings do not agree to within about 15% then a laser 'mode-hop' is assumed to have occurred and the recording repeated. The frequency of the CH line is calculated knowing the fringe spacing and the tellurium frequency and if a hard copy is required the spectrum may be output on a plotter. A typical recording, with a CH rotational line, tellurium spectrum and fringes is shown in figure 4.

Spectra of the strongest lines for CH were recorded using intermodulated fluorescence, the experimental details of which were described in chapter 3. The signals were quite easy to record once good overlap of the laser beams had been obtained. Only the splittings between the lines

Figure 4. The $R_{2e}(6)$ line of the (0,0) band of the $A^2\Delta - X^2\Pi$ system of CH recorded by computer. The three channels are the CH signal which contains only one line $R_{2e}(6)$, the absolute frequency calibration spectrum of Te_2 which contains one measured line, and the 75 MHz fringes which make it possible to interpolate between the tellurium and CH spectra. This spectrum was measured by the computer and plotted out with the line centres marked as shown, together with the calculated frequency for the CH transition in cm^{-1}.

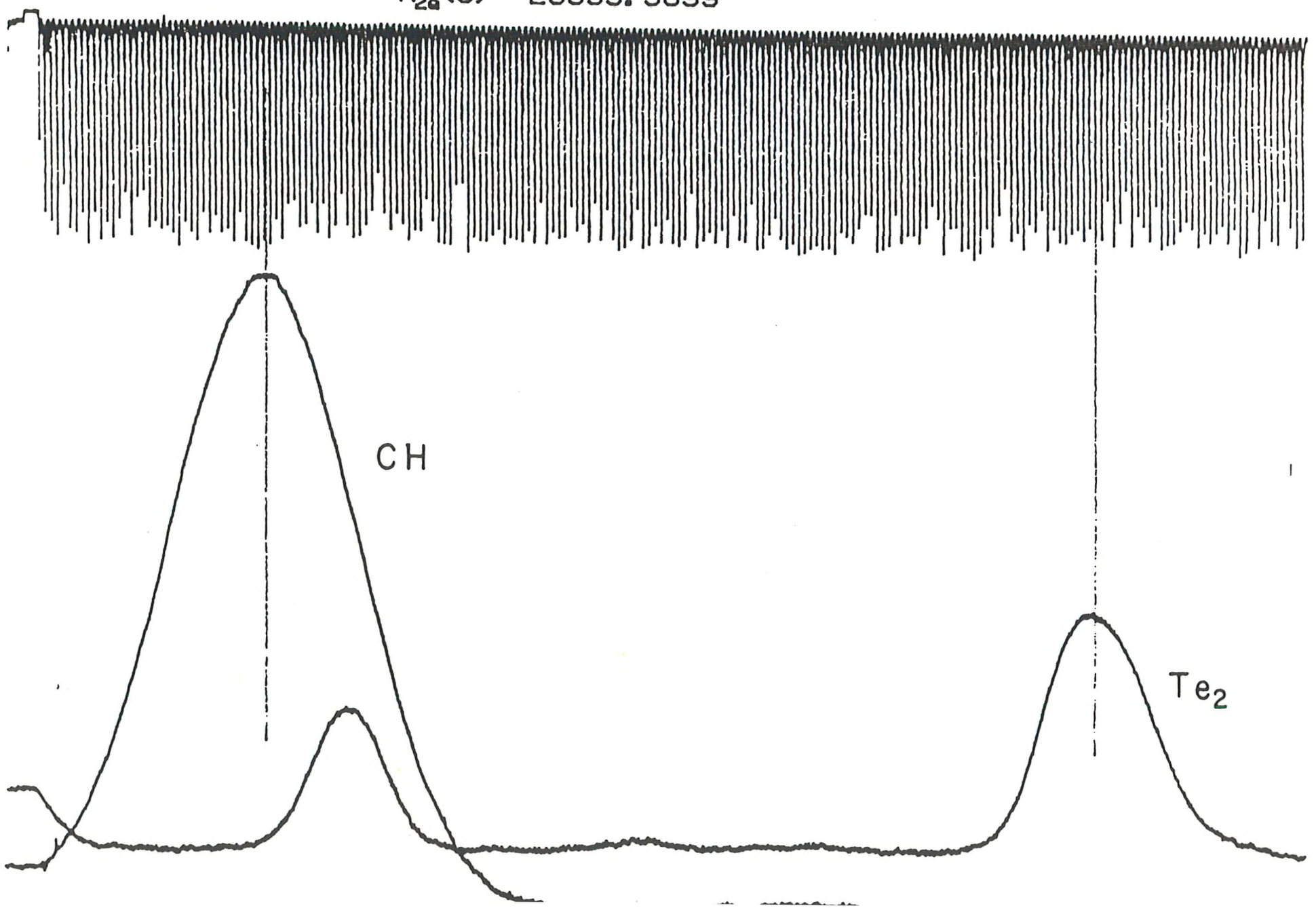
$R_{2a}(6)$ 23393.5699
CH
Te_2

were measured, no attempt being made to determine the absolute positions of the components. A total pressure of about 400 mTorr was used when recording IMF signals as above this the lines appeared to be broadened. These measurements gave information on the excited state hyperfine structure, no previous observations of which had been made.

Measurement of the ground state microwave spectrum was, accomplished by MODR. The laser beam was tuned to one of the components of the transition usually the higher energy one and the fluorescence monitored as the microwave frequency was swept across the region of interest. Amplitude modulation of the microwaves at about 2 kHz and phase-sensitive detection was used to improve the signal to noise. The pressure was kept somewhat lower than in the other measurements, at about 250 mTorr, above this the lines were significantly broadened due to collisional effects. Below this pressure the fluorescence signal died quite rapidly possibly due to the fact that the methane flow rate could not be reduced sufficiently to maintain efficient production of CH. The limiting linewidth due to the upper state fluorescent lifetime of 0.53 μs (16) corresponds to a FWHM of only 0.5 MHz, so it is clear that some residual collisional and saturation effects were increasing the linewidth.

Predictions of the two N=3 lambda doubling frequencies (10) were good to about 2 MHz and when the laser beam was tuned to one of the components in the N=3 J=2½ level, and the microwaves scanned manually across the range of interest very strong signals were found immediately. In this case the microwave power was supplied by a Hewlett-Packard BWO HP8695A amplified with a Hughes TWTA producing upto 10 Watts. The radiation was passed down waveguide to the cell where the end was butted against the side of the reaction cell opposite to the phototube. No horn was used to increase the amount of power coupled out, although a phase shifter was available to improve the matching of the cell and waveguide, and to reduce reflected power. Despite this crude arrangement for inputting the radiation, sufficient

power was available to readily saturate the signals and it was necessary to reduce this by about a factor of ten for the stronger lines which were easily power broadened.

The two N=2 lambda doubling transitions were also measured using a BWO and TWTA, provided by Dr. B.J. Howard of Oxford. In this case a problem was experienced with pick-up of the microwave radiation by the photomultiplier tube, and current follower connected to it. Although the apparent lines due to this were somewhat broader than the true signals they did present some problems due to variation in baseline. This was reduced by removing the current follower from the photo-tube housing and placing it in a position shielded from the microwave radiation. No attempt was made to observe the N=1 lines, one of which has been seen astronomically and measured to high precision, the other at about 780 MHz is below the region were our technique of launching the radiation from waveguide is applicable. The small splitting also means that the optical transitions are considerably overlapped making pumping of only one very difficult. The N=4 transitions lie above the range of available TWT amplifiers, but a klystron Oki 24V10A was available to measure the 24 GHz transition. This gave a power of about 200 mWatts, sufficient to allow the observation of the weak $\Delta F = \pm 1$ transitions.

Accurate measurements of the frequencies of the transitions were obtained by mixing a small portion of the radiation with a low frequency reference signal which was stabilised to 1 kHz using a Microwave Systems MOS-5 frequency stabiliser and counted, Hewlett-Packard HP-5245L. Beat signals at 30 MHz were detected with a Microwave Systems PLS-30 synchroniser. The reference frequency was adjusted so that one of the main peaks from the beat signal occured close to the centre of the transition of interest. A short time constant 0.3 sec together with a long scan 1000 sec were used to reduce the frequency shift to a minimum, however as the microwave frequency could only be tuned in one direction some small deviation probably still remained. The 24 GHz measurements, where scanning in both

Figure 5. Schematic of the set-up required for computer recording of MODR spectra. The radiation of interest is locked to a stabilised low frequency source by a synchroniser. The spectrum is recorded by driving the low frequency stabiliser using the D/A output from the computer interface. After each adjustment the frequency can be counted and a series of measurements from the lock-in amplifier taken.

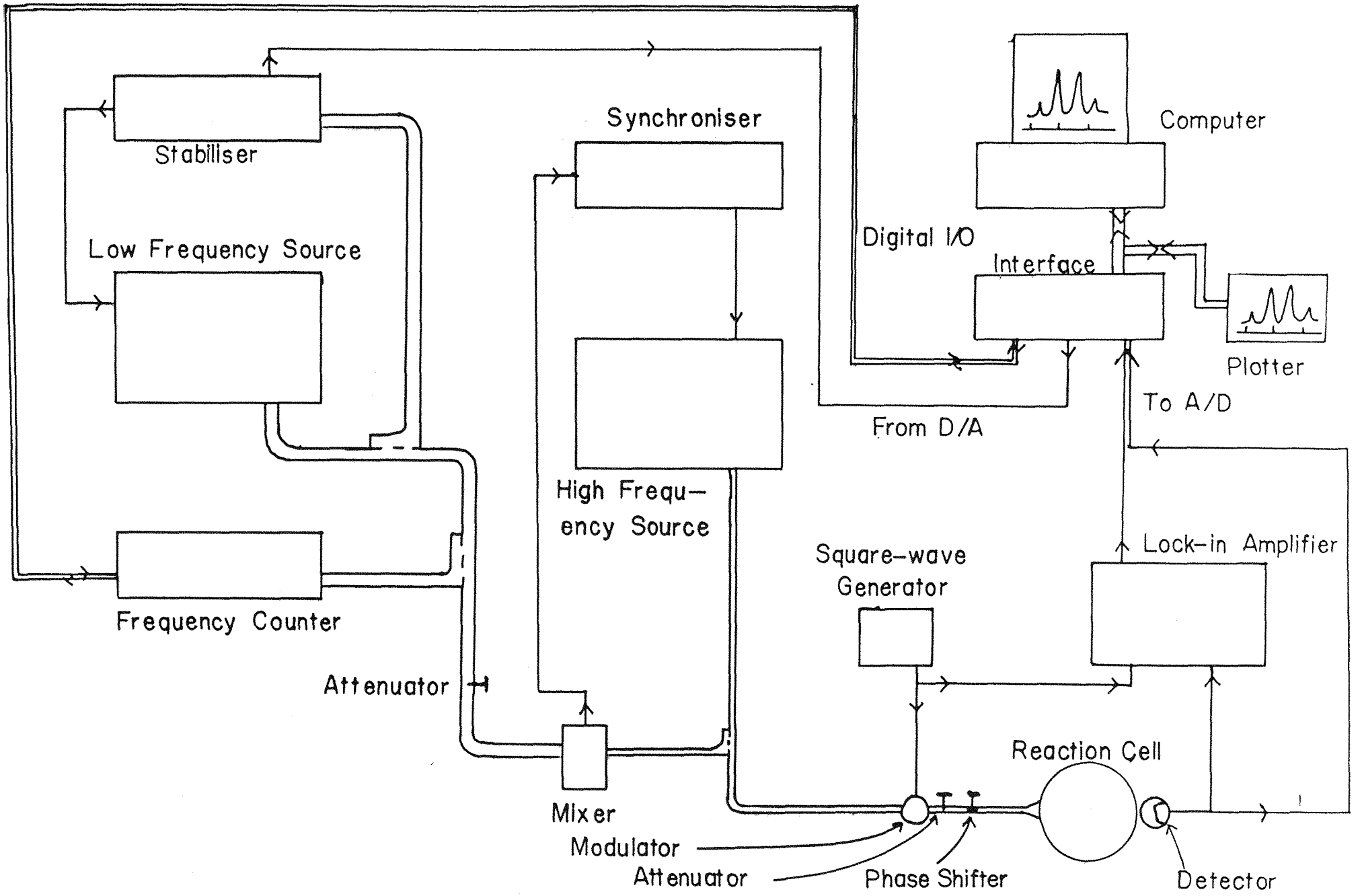
Stabiliser
Synchroniser
Computer
Low Frequency Source
Digital I/O
Interface
Plotter
To A/D
From D/A
High Frequency Source
Square-wave Generator
Lock-in Amplifier
Frequency Counter
Attenuator
Reaction Cell
Mixer
Modulator
Attenuator
Phase Shifter
Detector

directions was possible, and the 4 GHz signals, measured by hand-tuning the microwave frequency, showed this to be about 0.1 MHz. A correction of this size was made to the transitions measured with the frequency swept in one direction only.

The possibility of systematic errors of this type is clearly a major deficiency in measurements for which great accuracy is required. In this case it was necessary to double the error limit on the measurements and clearly the method described above is not the most accurate way to measure the line positions. Both of these problems may be overcome by a completely different method of recording, using computer control. Although the equipment for such measurements had been acquired, it was not available in time for the CH recordings. The basic set-up, shown in figure 5, involves synchronising the microwave radiation of interest to a stabilised reference frequency. This can then be varied in a step-wise fashion by the computer, a series of readings being taken at each point, the average of these being displayed directly on the screen. The microwave frequency for each measurement is obtained by the computer directly from the frequency counter. The result of this would probably be an improvement of upto one order of magnitude in the accuracy of the measurements.

Table 1. Etalon calibration

	No. of fringes	Splitting (MHz)	Etalon spacing (MHz)
$R_1(1)$			
$1^- - 1^+$	9.64(6)[a]	724.789	75.19(47)
$2^- - 2^+$	9.34(7)	701.677	75.10(56)
$R_2(1)$			
$1^- - 1^+$	44.39(8)	3335.481	75.14(14)
$0^- - 0^+$	43.68(8)	3277.506	75.03(14)

[a] The figures in parentheses are the estimated errors in units of the last quoted decimal place.

Weighted mean etalon spacing = 75.09(10) MHz

6.3 Calibration of the 75 MHz Etalon

A 1 m confocal elalon is used to obtain markers for LIF and IMF measurements. If this is to be of any use then it is important that it is calibrated as accurately as possible. When first constructed the etalon was calibrated by recording a set of fringes between two iodine lines and comparing them with the iodine atlas. This gave a fringe spacing of 76.9 MHz, which was assumed to be accurate to ±0.1 MHz. However when the two R(1) lines in the $A^2\Delta - X^2\Pi$ system of CH were recorded using IMF it was found that in both cases the splitting between the lambda doublets did not agree with the microwave measurements of these spacings. The discrepancy was quite large, of the order of 2%, which is much greater than the possible measurement errors, and thus it was considered necessary to recalibrate the etalon. The most likely cause of the original error is that a laser 'mode-hop' occurred during the scan and thus led to the wrong number of fringes being observed between the iodine lines. Such a large change could not have been produced by the effects of temperature and pressure change, or a slightly different alignment of the laser beam through the etalon, as the scope for changing the angle of the beam is very small and the temperature is regulated by a heater unit with a thermocouple positioned inside the etalon.

The calibration was performed by comparing the IMF measurements of the lambda doubling splittings in the $R_1(1)$ and $R_2(1)$ transitions with the pure ground state splittings obtained from the microwave measurements. The effects of upper state hyperfine were removed by using all of the observed splittings in the spectra, and the contribution from lambda doubling in the $^2\Delta$ state was assumed to be zero, as calculations based on the observed high N effects showed the splitting for N=1 to be less than 0.1 MHz. The results for $R_1(1)$ and $R_2(1)$ are shown in table 1, and when the different values are averaged together the etalon fringe spacing is found to be

75.09 (10) MHz

Figure 6. The N = 3, J = 5/2 lambda doubling transition of the CH radical. The proton hyperfine structure is labeled by the value of the quantum number F involved.

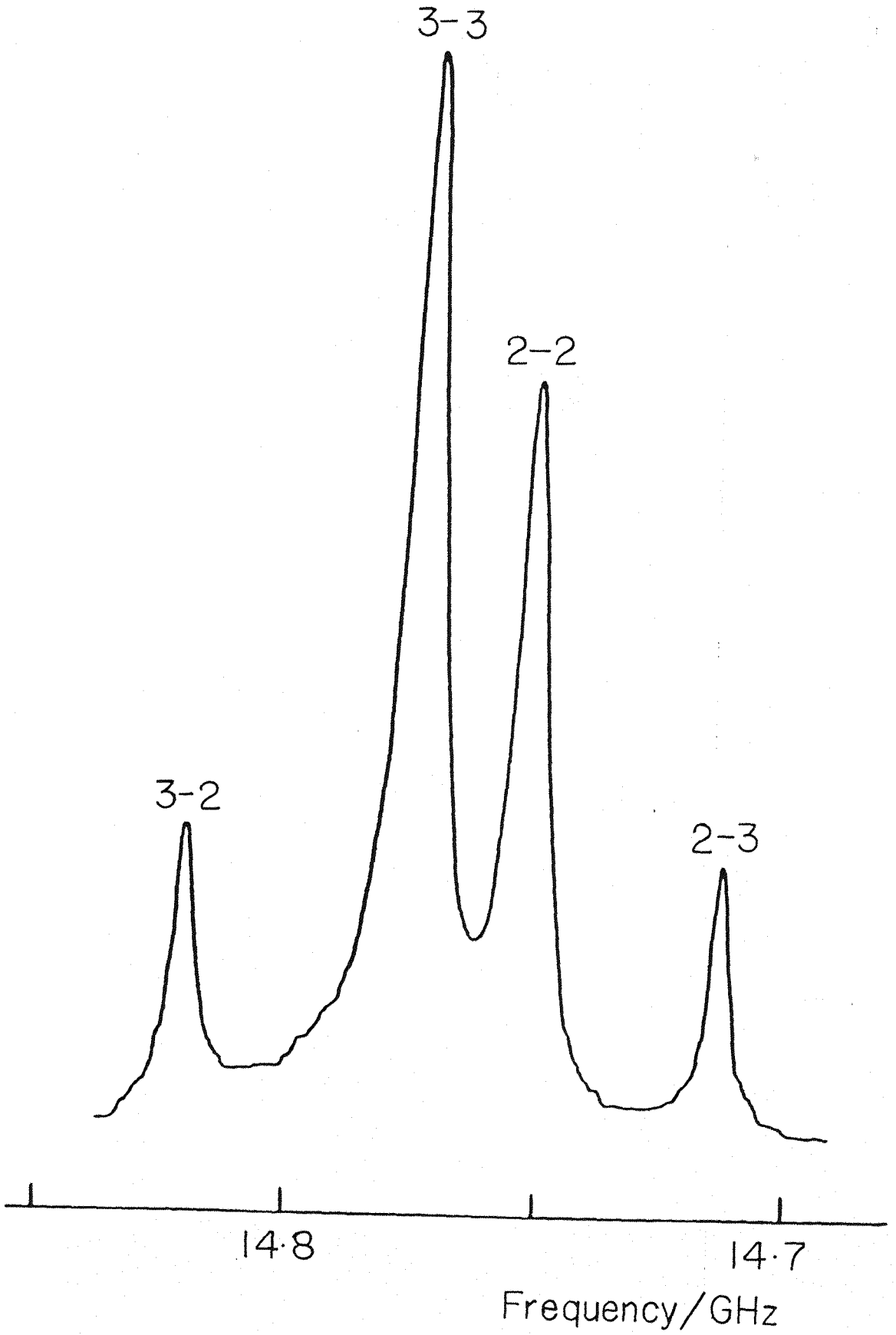
3-3
2-2
3-2
2-3
14·8
14·7
Frequency/GHz

6.4 The microwave spectrum of CH

Observations

Due to the very strong optical signal obtained we were confident of making the first laboratory observation of the ground state microwave spectrum of CH. When the laser was tuned to one of the N=3, J=3½ components and the microwaves scanned across the predicted frequency a very strong signal was immediately found. A total of 18 transitions between five pairs of lambda doublets in the N = 2,3 and 4 rotational levels of CH were measured. The spectrum usually consisted of four lines, two strong ones in the centre with weaker satellite lines on each side. This structure is due to proton (I = ½) hyperfine effects, the centre lines being the $\Delta F = 0$ components and the outer ones $\Delta F = \pm 1$. A typical example of this pattern for the F_2 levels is shown in figure 6. The weak lines appear much stronger, than expected relative to the centre pair. This is because high microwave power was needed to observe the satellite lines and this caused power broadening of the other transitions. The satellite lines were much closer in the F_1 spectra and for the N=2 level it was not possible to measure them. A list of the experimental measurements, together with their assignments, is given in table 2.

The signal to noise ratio for the observed transitions was very high, typically 100 to 1 or greater for the main components and at least 10 to 1 for the others. This meant that the centre of the line could be picked to quite high precision, increasing the accuracy of the results. All the transitions observed were immediately assigned as they were close to the positions predicted by Brown and Evenson (10). The F_2 N=4 lines were quite some way out however, probably due to a lack of data from the LMR measurements on these levels together with a since corrected misassignment in the spectra.

Table 2. Lambda doubling transition frequencies in CH $X^2\Pi$

Transition			Frequency (MHz)	Obs-Calc (kHz)
N	J	F		
1	3/2	$2^- - 2^+$	701.677(7)[ab]	0.9
		$1^- - 1^+$	724.789(7)[b]	-2.5
1	1/2	$0^- - 1^+$	3263.794(3)[c]	-0.1
		$1^- - 1^+$	3335.481(2)[c]	0.2
		$1^- - 0^+$	3349.193(3)[c]	-0.1
2	5/2	$3^+ - 3^-$	4847.84(20)	76.8
		$2^+ - 2^-$	4870.12(20)	59.1
2	3/2	$1^+ - 2^-$	7274.78(15)	-280
		$1^+ - 1^-$	7325.15(15)	-60.1
		$2^+ - 2^-$	7348.28(15)	-142
		$2^+ - 1^-$	7398.38(15)	-193
3	7/2	$4^- - 3^+$	11250.79(50)	-25.9
		$4^- - 4^+$	11265.21(15)	231
		$3^- - 3^+$	11287.05(15)	74.6
		$3^- - 4^+$	11301.22(20)	29.3
3	5/2	$2^- - 3^+$	14713.78(15)	91.6
		$2^- - 2^+$	14756.81(15)	129
		$3^- - 3^+$	14778.97(20)	-3.5
		$3^- - 2^+$	14821.88(15)	-85.6
4	7/2	$3^+ - 4^-$	24381.57(40)	246
		$3^+ - 3^-$	24420.65(10)	3.8
		$4^+ - 4^-$	24442.56(10)	-16.5
		$4^+ - 3^-$	24482.10(20)	202
6	13/2	$7^+ - 7^-$	43851.026(30)[e]	-10
		$6^+ - 6^-$	43872.591(30)[e]	-9.6
6	11/2	$5^+ - 5^-$	50299.750(20)[e]	1.8
		$6^+ - 6^-$	50321.276(20)[e]	-2.9
7	15/2	$8^- - 8^+$	58986.633(20)[e]	1.4
		$7^- - 7^+$	59008.076(20)[e]	6.6
7	13/2	$6^- - 6^+$	66400.098(30)[e]	-0.8
		$7^- - 7^+$	66421.466(30)[e]	1.6
8	17/2	$9^+ - 9^-$	76147.336(30)[e]	-1.7
		$8^+ - 8^-$	76168.632(50)[e]	-8.4

[a] The numbers in parentheses represent one standard error estimates, in units of the last quoted decimal place.

[b] Astronomical measurement by Ziurys (13).

[c] Astronomical measurement by Rydbeck et al (6).

[d] Partially resolved satellite line.

Fit of the Data

The observed transitions give information only on the lambda doubling and hyperfine parameters, and to fit them it was necessary to constrain the fine structure parameters, the values chosen were from the LMR measurements (9). While the data was being fitted, it was learned that several higher N, lambda doubling transitions had been measured by Bogey et al (12) and these were included in the fit, together with the astrophysically observed lines (6,7). The preferred N^2 version of the Hamiltonian (17) was used, this has been described in chapter 2. The $X^2\Pi$ state of CH is a very good example of Hund's case b coupling with $A \approx 2B$ and the energies are given by $BN(N+1)$ each level being split into a spin-rotation doublet with $J = N \pm \frac{1}{2}$. As a result of this it was decided to determine the parameter combinations appropriate for case b, that is p and q rather than the case a combinations $p + 2q$ and q. The data were weighted in the fit according to the inverse square of the experimental error, these values are given in table 2.

Initially the lambda doubling frequencies were fitted with the fine and rotational structure parameters constrained to the values given by Brown and Evenson (9). These numbers were changed slightly when a misassignment, which had resulted in a rather poor quality of fit for the LMR data, was corrected. As the lambda doubling and hyperfine parameters were determined to much greater precision from the microwave data, it was decided to refit the LMR results with these parameters constrained to the values from the microwave fit. Finally the lambda doubling measurements were refitted using the new LMR parameters, the changes were sufficiently small that it was not considered necessary to continue the process any further. The parameters from these final fits are shown in table 3. It was possible to determine most of the fine and rotational structure parameters, but the value for H had to be calculated as the measurements did not go to sufficiently high N to allow its evaluation. The expression used to

evaluate H was

$$H_o \approx H_e = 2/3D_e(12(B_e/\omega_e)^2-\alpha_e/\omega_e) \qquad 6.1$$

where the subscript e denotes an equilibrium value and ω_e and α_e are the harmonic vibrational frequency and the anharmonic correction to the rotational constant, respectively. The calculated g factors are explained in ref 9.

To correctly fit the lambda doubling measurements, it was necessary to include higher order hyperfine contributions. The origin of these terms in the molecular Hamiltonian has been described by Brown et al (18) when discussing the OH molecule. They give a total of five parameters C_1, C_1', c_D, c_6 and d_D of which only three are usually, separately determinable, in the case of OH it was decided to use C_1, C_1' and d_D. The first two are nuclear spin rotation interactions, C_1 being diagonal in Λ while C_1' is a lambda doubling type term. d_D is also lambda doubling and represents the centrifugal distortion correction to d. In the case of CH it was not possible to determine C_1, however the other two were both determinable, the inclusion of d_D gave a significant improvement in the fit. The value of d is determined by the splitting of the main components in each set of microwave transitions and hence is very accurately determined over a wide range of N values. In particular the astrophysical measurements, being of such great precision tend to tie down d and any variation from the splitting, given by this value, at higher N leads to the determination of higher order hyperfine contrbutions. Hence only the lambda-doubling higher order terms, C_1' and d_D, could be determined. A total of six lambda-doubling parameters (p, p_D, p_H, q, q_D, and q_H) were also required. The overall quality of fit for the LMR data of 0.94 was quite good while the microwave measurements were over determined slightly with a standard deviation for the fit of 0.79. The quality of fit relative to experimental error was about the same for each of the three sets of microwave data.

While this chapter was being written we learned of the

first astrophysical observations of rotationally excited CH (13). The two $\Delta F=0$ components of the N=1 J=1½ lambda doubling transition at about 780 MHz were seen and the assignment confirmed by reference to the frequencies calculated from the constants derived here. The discrepancies between the observed frequencies and the extrapolated ones were only 8 kHz and 3 kHz for the two lines, the estimated experimental precision being 7 kHz. The very good match achieved indicates that the frequencies for the other rotationally excited lambda doubling transitions should be accurate to about 10 kHz and this should lead to further interstellar observations of CH in its higher rotational levels. The new astrophysical frequencies were included in the final fit of the microwave measurements, but as they were so close to the predicted positions they made little difference to the constants, except for increasing the accuracies slightly.

Figure 15. The low lying states of CH. The $X^2\Pi$ ground state has a $\sigma^2\pi$ configuration and excitation of a σ electron to a π orbital gives rise to the first four excited states as shown. Interaction with the $B^2\Sigma^-$ and $C^2\Sigma^+$ states is the main cause of the lambda-doubling and spin-rotation effects in the $A^2\Delta$ and $X^2\Pi$ states. The positions are shown relative to v = 0 of the ground state. The energies for the a, B and C states are taken from Huber and Herzberg (19).

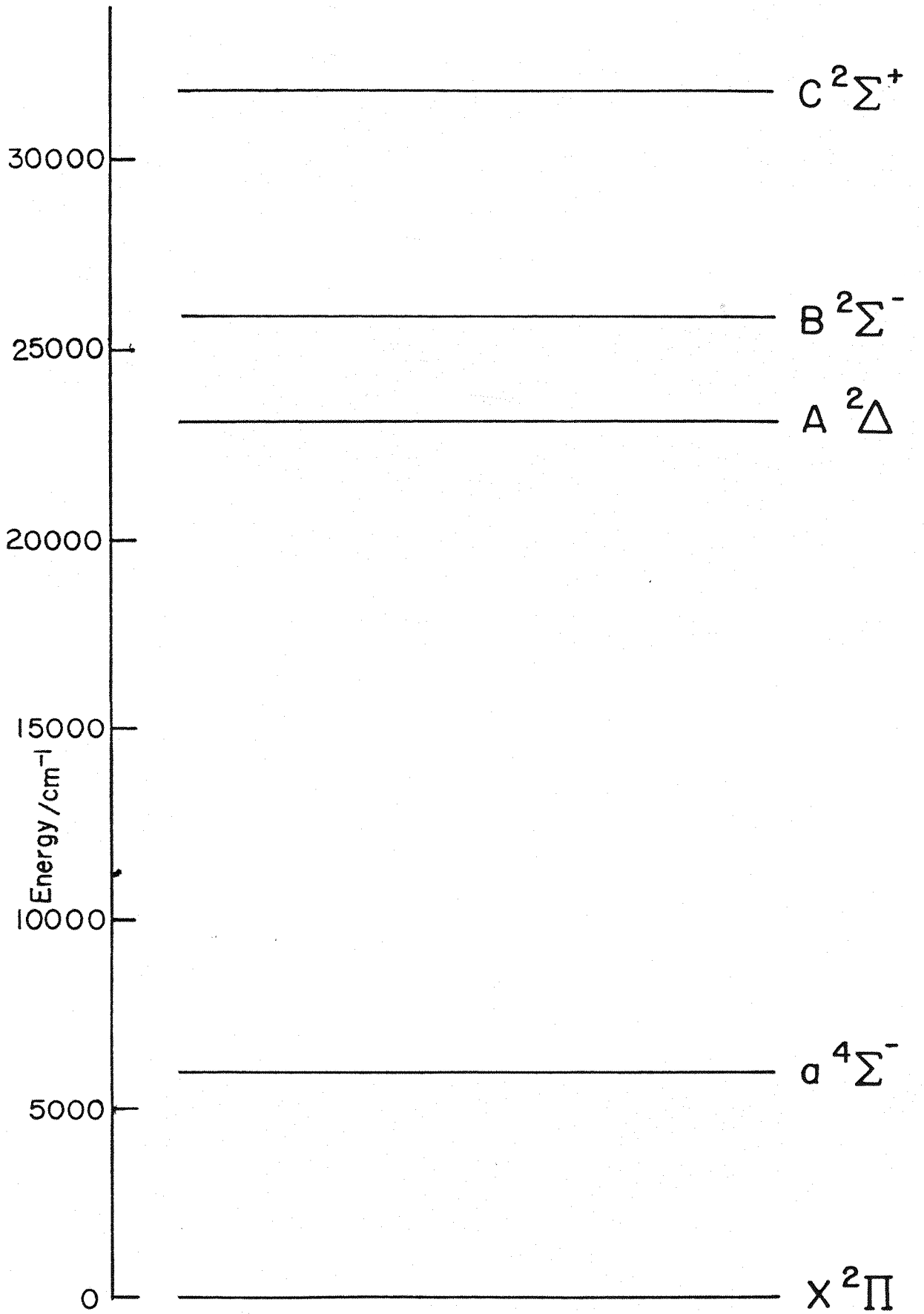
Energy /cm⁻¹
30000
25000
20000
15000
10000
5000
0
C ²Σ⁺
B ²Σ⁻
A ²Δ
a ⁴Σ⁻
X ²Π

6.5 Discussion

The values of the fine and rotational structure constants have been improved slightly by refitting the LMR data but as these constants were not determined from this investigation they will not be further discussed here. It has been possible to determine a total of six lambda doubling parameters in the fit (p, p_D, p_H, q, q_D and q_H). If the $^2\Pi$ state is perturbed only by a single $^2\Sigma$ state then, as was shown to occur for CuF in chapter 5, the value of p would equal -2γ but this is not the case. Examination of the low lying electronic states of CH shown in figure 15 indicates that the main contributions to the lambda doubling parameters come from the $B^2\Sigma^-$ and $C^2\Sigma^+$ states.

The electronic configuration of the $X^2\Pi$ state is

$$1\sigma^2 2\sigma^2 3\sigma^2 1\pi^1$$

This gives rise only to the ground $^2\Pi$ state, the low excited states are produced by promoting an electron from the 3σ orbital to the 1π giving

$$1\sigma^2 2\sigma^2 3\sigma^1 1\pi^2$$

This configuration leads to several excited states:

$$a^4\Sigma^- \quad A^2\Delta \quad B^2\Sigma^- \quad C^2\Sigma^+$$

all of which have been observed although little is known about the $a^4\Sigma^-$ state. The values of p and q may be calculated from the expressions (18)

$$p = 2 \Sigma (-)^s (E_\pi - E_\Sigma)^{-1} \langle ^2\Pi | AL_+ | ^2\Sigma \rangle \langle ^2\Pi | BL_+ | ^2\Sigma \rangle \qquad 6.2$$

$$q = 2 \Sigma (-)^s (E_\pi - E_\Sigma)^{-1} [\langle ^2\Pi | BL_+ | ^2\Sigma \rangle]^2 \qquad 6.3$$

where s is even for $^2\Sigma^+$ states and odd for $^2\Sigma^-$ states.

If pure precession between the $^2\Pi$ state and the $^2\Sigma$

states is assumed then the expectation values may be readily evaluated giving

$$\langle {}^2\Pi | L_+ | {}^2\Sigma \rangle = (l(l+1))^{1/2} = \sqrt{2} \quad \text{as } l=1$$

and thus

$$p = 4AB \sum (-)^S (E_\pi - E_\Sigma)^{-1} \qquad 6.4$$

$$q = 4B^2 \sum (-)^S (E_\pi - E_\Sigma)^{-1} \qquad 6.5$$

Putting in the appropriate values for A and B together with the energy separations between the $v = 0$ levels of the states (19)

$$\nu(0,0) \quad {}^2\Sigma^- - {}^2\Pi = 25698.2 \text{ cm}^{-1}$$

$$\nu(0,0) \quad {}^2\Sigma^+ - {}^2\Pi = 31778.1 \text{ cm}^{-1}$$

gives the following values

$$p = 324 \text{ MHz} \qquad q = 162 \text{ MHz}$$

These numbers are clearly in very poor agreement with the values measured experimentally. The most likely cause for this is that some of the assumptions made are not valid. The expressions given above for p and q are both general terms with the interactions between the $^2\Pi$ and $^2\Sigma$ states written as though they involve the whole state whereas only specific components should be considered. If this is done then p and q are given by the following expressions

$$p = 4 \sum (E_\pi - E_\Sigma)^{-1} \langle {}^2\Pi_{1/2} | \mathcal{H}_{so} | {}^2\Sigma_{1/2} \rangle \langle {}^2\Sigma_{1/2} | BL_+ | {}^2\Pi_{-1/2} \rangle \qquad 6.6$$

$$q = 2 \sum (-)^S (E_\pi - E_\Sigma)^{-1} [\langle {}^2\Pi_{3/2} | BL_+ | {}^2\Sigma_{1/2} \rangle]^2 \qquad 6.7$$

To evaluate these expressions it is necessary to deduce the explicit representations for all of the electrons in

unclosed shells in either the $^2\Pi$ or $^2\Sigma$ states. That is $3o^2 1\pi^1$ for the $^2\Pi$ state and $3o^1 1\pi^2$ for the $^2\Sigma$ states. The spin-orbitals which make up the components of these states are as follows :

$^2\Pi_{3/2}$ $\quad |\sigma\bar{\pi}+|$

$^2\Pi_{1/2}$ $\quad |o\bar{\sigma}\bar{\pi}+|$

$^2\Pi_{-1/2}$ $\quad |\sigma\bar{\sigma}\pi-|$

$^2\Pi_{-3/2}$ $\quad |o\bar{\sigma}\bar{\pi}-|$

$^2\Sigma^+_{1/2}$ $\quad 1/(\sqrt{2})\{|\sigma\pi+\bar{\pi}-| - |\sigma\bar{\pi}+\pi-|\}$

$^2\Sigma^+_{-1/2}$ $\quad 1/(\sqrt{2})\{|\acute{o}\bar{\pi}+\pi-| - |\check{o}\pi+\bar{\pi}-|\}$

$^2\Sigma^-_{1/2}$ $\quad 1/(\sqrt{6})\{2|\bar{o}\pi+\pi-| - |\sigma\bar{\pi}+\pi-| - |\sigma\pi+\bar{\pi}-|\}$

$^2\Sigma^-_{-1/2}$ $\quad 1/(\sqrt{6})\{2|o\bar{\pi}+\bar{\pi}-| - |\acute{o}\bar{\pi}+\pi-| - |\acute{o}\pi+\bar{\pi}-|\}$

Hence

$$\begin{aligned}\langle ^2\Pi_{1/2}|\mathcal{H}so|^2\Sigma^+_{1/2}\rangle &= -1/\sqrt{2}\{-\langle\bar{o}|\mathcal{H}so|\pi-\rangle\}\\ &= 1/(2\sqrt{2})\zeta\langle\bar{o}|1+|\bar{\pi}-\rangle\\ &= 1/2\ \zeta\end{aligned}$$

and similarly

$$\langle ^2\Pi_{1/2}|\mathcal{H}so|^2\Sigma^-_{1/2}\rangle = 1/(2\sqrt{3})\ \zeta$$

$$\langle ^2\Sigma^+_{1/2}|L+|^2\Pi_{-1/2}\rangle = -1$$

$$\langle ^2\Sigma^-_{1/2}|L+|^2\Pi_{-1/2}\rangle = -\sqrt{3}$$

$$\langle ^2\Pi_{3/2}|L+|^2\Sigma^+_{1/2}\rangle = -1$$

$$\langle ^2\Pi_{3/2}|L+|^2\Sigma^-_{1/2}\rangle = \sqrt{3}$$

Substituting in the expressions for the lambda doubling constants gives

$$p = 4\{-\tfrac{1}{2}\zeta B/(E\pi-E_{\Sigma+}) - \tfrac{1}{2}\zeta B/(E\pi-E_{\Sigma-})\} \qquad 6.8$$

$$q = 2\{B^2/(E\pi-E_{\Sigma+}) - 3B^2/(E\pi-E_{\Sigma-}) \qquad 6.9$$

Taking B = Bo for the $^2\Pi$ state and ζ = 27.5 cm^{-1} for a carbon 2p orbital (20) gives

$$p = 1654 \text{ MHz} \qquad q = 1030 \text{ MHz}$$

These values show much improvement on the previous calculation and clearly demonstrate that it is necessary to perform these calculations using the full spin orbital representations rather than simply using the overall representations. There is however still some discrepancy between these values and the experimentally determined results.

$$p = 1003.996\ (4) \text{ MHz} \qquad q = 1159.683\ (2) \text{ MHz}$$

Possible reasons for this are: that the matrix elements were evaluated assuming pure precession of the electrons which is not strictly true when many states may result from a given configuration as here; the neglect of contributions from higher vibrational levels in the $^2\Sigma^+$ and $^2\Sigma^-$ states; and neglect of contributions from other electronic states notably the $a^4\Sigma^-$ state which lies only 6000 cm^{-1} (19) above the $X^2\Pi$ state.

In order to overcome the problems mentioned above it is necessary to perform a full ab initio calculation of the lambda doubling parameters, this has been done by Richards et al (21). They performed several calculations including different factors and their best result was

$$p = 1037 \text{ MHz} \qquad q = 1136 \text{ MHz}$$

This is in quite good agreement with the experimentally determined values but clearly additional contributions must be included if such calculations are to come close to the accuracy with which these constants can be determined experimentally. Notably the observation by Richards et al (21) that their calculations are now comparable in accuracy to terrestrial experiments is only true in cases where the

constants have been determined from electronic spectra. If the more precise techniques of LMR and microwave spectroscopy are used then the experimentally determined values are far more accurate than the theoretical estimates and in the case of microwave measurements come close to the very high precision obtained by astrophysical observations.

It is also possible to make an estimate of γ using similar expressions and the relation $\gamma = -\frac{1}{2}p$ but it must be remembered that $^2\Delta$ states can also contribute to γ. Thus similar calculations to those so far performed must be made for the interaction between a $^2\Pi$ and a $^2\Delta$ state. These are of the form

$$(E\pi - E_\Delta)^{-1} \langle ^2\Pi_{3/2} | \mathcal{H}_{so} | ^2\Delta_{3/2} \rangle \langle ^2\Delta_{3/2} | BL_+ | ^2\Pi_{1/2} \rangle \qquad 6.10$$

The expectation values may be evaluated in the same way as before to give

$$\langle ^2\Pi_{3/2} | \mathcal{H}_{so} | ^2\Delta_{3/2} \rangle = 1/\sqrt{2}\zeta$$
$$\langle ^2\Delta_{3/2} | BL_+ | ^2\Pi_{1/2} \rangle = -\sqrt{2}B$$

Taking $E\pi - E_\Delta = -23217.5$ cm^{-1} gives the contribution to γ from the $^2\Delta$ state as

$$-1007 \text{ MHz}$$

The contributions from the $^2\Sigma$ states occur with opposite signs for γ and hence the original separate contributions must be used. As $\gamma = -\frac{1}{2}p$ for the $^2\Sigma^+$ state and $+\frac{1}{2}p$ for the $^2\Sigma^-$ state the respective contributions are as follows

$^2\Sigma^+$	-368 MHz
$^2\Sigma^-$	455 MHz

Adding together the three contributions gives the following calculated value for γ

$$\gamma = -920 \text{ MHz}$$

This is in quite good agreement with the experimental value

$$\gamma = -771.11\ (5)\ \text{MHz}$$

At first sight it might be thought that the lambda doubling and spin-rotation interactions both arose from mixing with a $^2\Sigma^+$ state as $\gamma \approx -\frac{1}{2}p$ but in fact the $^2\Sigma$ contributions virtually cancel out and γ is due mainly to the interaction with the $^2\Delta$ state.

The higher order lambda doubling terms are much more difficult to evaluate theoretically. The first order corrections p_D and q_D involve contributions in third order of perturbation theory from similar electronic interactions to those which give rise to p and q. There are also centrifugal distortion contributions which arise from mixing with neighbouring vibrational states. Veseth (22) gives approximate formulae for p_D and q_D

$$p_D = -2pD/B \qquad q_D = -4qD/B \qquad 6.11$$

Evaluation of these expressions gives p_D = -0.206 MHz and q_D = -0.476 MHz which compare reasonably well with the experimentally determined values -0.2735 MHz and -0.4575 MHz respectively. No similar formulae exist for p_H and q_H which arise from fourth order electronic contributions and third order vibrational effects.

The four first order hyperfine parameters have been determined in the fit of the microwave data. Levy and Hinze (23) calculated values for a,b (=b_F-1/3c) and c by ab initio methods while maintaining the only parameter then known, d, at the value determined by the astrophysical data. Their values are 58.5±4.5, -72±10 and 57±4 MHz respectively which are in close agreement with the experimentally determined values of 54.3 (3), -76.7 (5) and 57.2 (3) MHz. The Fermi contact parameter b_F is expected to be negative in a π radical like CH where the unpaired electron exists primarily in a carbon $2p_x$ or $2p_y$ orbital, and contributions to b_F arise by spin polarisation (20).

If it is assumed that $\langle \sin^2\theta \rangle = \langle 1-\cos^2\theta \rangle$ then the value for c/3+d should equal a. The values are 62.6 and 54.3 respectively. This equality assumes that $\langle 1/r^3 \rangle_{spin} = \langle 1/r^3 \rangle_{orbit}$ and thus the degree of discrepancy can be used to estimate the extent of variation between the two quantities. The result is that

$$\langle 1/r^3 \rangle_{spin} = 1.15 \langle 1/r^3 \rangle_{orbit}.$$

The fact that the parameter d_p, the centrifugal distortion correction to the hyperfine lambda doubling parameter d was required in order to adequately fit the data shows that higher-order hyperfine effects arise primarily from mixing with other vibrational states. This is because in the effective Hamiltonian used no electronic contributions occur to d_p upto second order (18). The values determined for the higher order corrections d_p = -0.016 MHz and C_1' = 0.006 MHz are quite similar to the values determined for OH of -0.0228 and 0.0065 MHz respectively.

Figure 7. The (0,0) band of the $A^2\Delta - X^2\Pi$ system of CH recorded by operating the dye-laser broadband and tuning the birefringent filter, the resolution is about 1 cm^{-1}. The sloping baseline is caused by scattered light, which falls off as the edge of the laser gain curve is reached at the high frequency end of the spectrum.

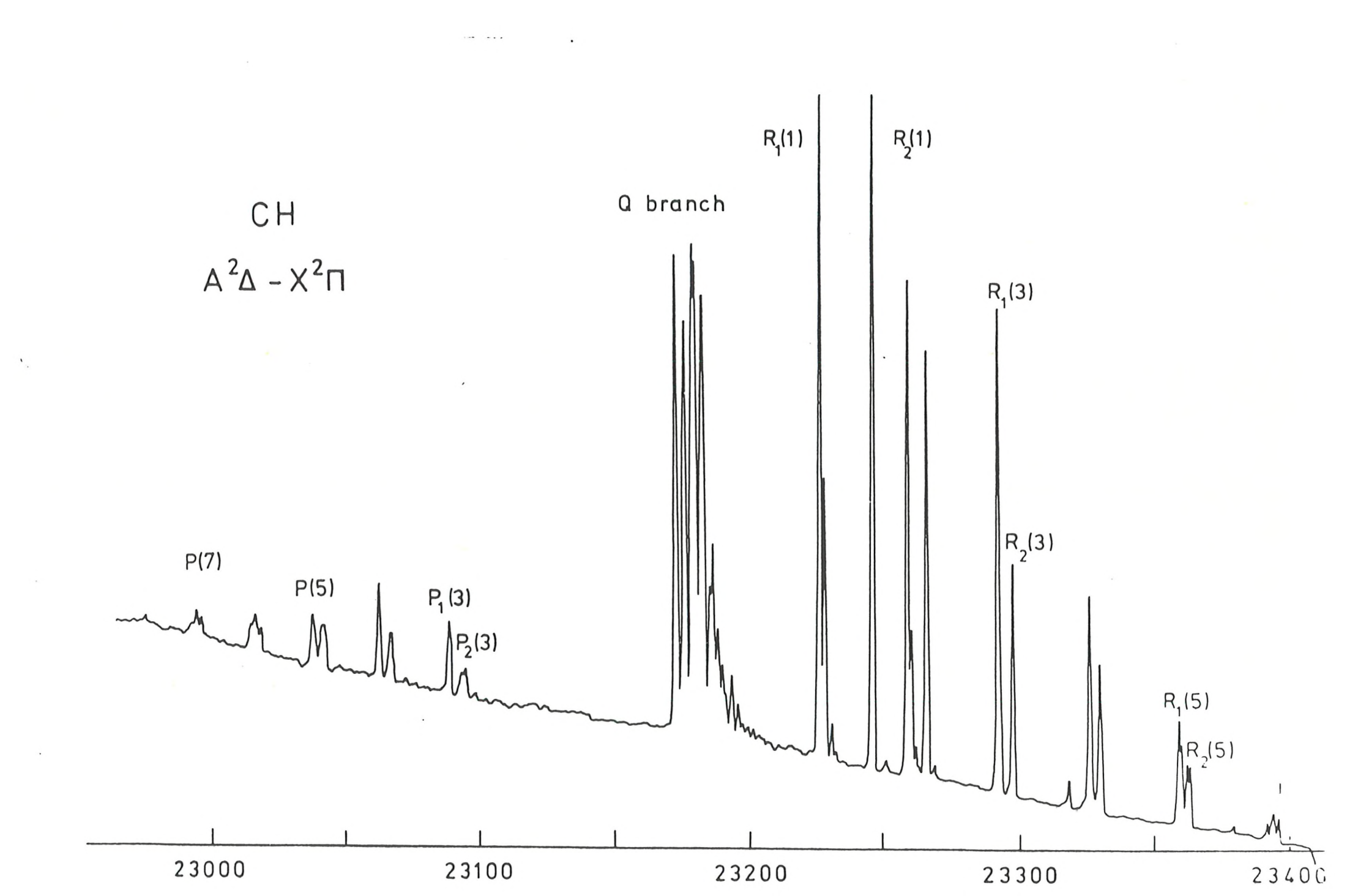
CH
$A^2\Delta - X^2\Pi$
Q branch
$R_1(1)$
$R_2(1)$
$R_1(3)$
$R_2(3)$
$R_1(5)$
$R_2(5)$
P(7)
P(5)
$P_1(3)$
$P_2(3)$
23000
23100
23200
23300
23400

6.6 The $A^2\Delta$ State of CH

Observations

Both the $X^2\Pi$ and $A^2\Delta$ states of CH are close to the Hund's case b coupling scheme that is $A \approx 2B$. As a result the energy levels in both molecules are well represented by the formula $BN(N+1)$ where N can take the values Λ, $\Lambda+1$,... , thus the $X^2\Pi$ state begins at N=1 and the $A^2\Delta$ state at N=2. The rotational levels are in each case split in two by spin-rotation mixing, each of these levels then exhibiting a lambda doubling splitting also. The result of this is a fairly simple spectrum, as can be seen from figure 7, which was recorded by scanning the dye-laser broadband, the linewidth being about 1 cm^{-1}. The pattern consists of P, Q and R branches with each N rotational transition split into four by the spin-rotation and lambda doubling interactions. A few weak transitions at low N for which $\Delta N \simeq \Delta J$ can be seen near the beginning of the R branch, similar lines occur near the beginning of the Q branch but are obscured by the strong $\Delta N = \Delta J$ structure. The R branch is by far the strongest with the P branch very weak. When observed at Doppler-limited resolution the width of the lines (FWHM) is 2.5 GHz and this corresponds to a translational temperature for the molecules of 320 K. The rotational constant for CH at 14 cm^{-1} is quite high and thus the strongest lines occur at very low N, the intensity falling off very rapidly, so that lines beyond N=7 for the ground state are not visible in the low resolution spectrum. The sloping baseline is due to the fall-off in laser scatter noise as the output power of the dye laser dropped, this makes the change in intensity with N in the R branch appear somewhat greater than it really is, lasing having stopped completely after R(6), with the result that the higher N lines could not be seen. This spectrum was recorded with a set of laser mirrors designed for operation at the green end of Stilbene 3 dye, a set of optics for use in the violet part of the output from the dye were acquired later so that the higher R branch lines could

be observed.

With the dye laser operating single frequency the (0,0) band of the $A^2\Delta$ - $X^2\Pi$ system was recorded at Doppler-limited resolution (FWHM = 2.5 GHz). This was done by interpolation between pairs of tellurium lines with the result that only about two thirds of the rotational lines could be recorded. With the improved signal to noise in these recordings, it was possible to record transitions involving upto N=10 in the ground state. While these measurements were good enough to give much improved fine structure and rotational constants for the $A^2\Delta$ state, the average measurement error of 0.005 cm^{-1} = 150 MHz was not sufficient for the other main purpose, determining the extent of lambda doubling in the excited state. This had been predicted to reach about 100 MHz by N=10 requiring a measurement accuracy of about 50 MHz for the determination to be significant, the computer recording method was designed to overcome this problem. All of the observable lines with N=7 or greater in the excited state were recorded at this improved accuracy, the measurement error being about 30 MHz. A total of 40 lines, spread throughout the different branches, were recorded by this method. Two overlapped lines $Q_{1f}(7)$ and $Q_{2f}(7)$ were deconvoluted by fitting to a Gaussian function for each, the resulting frequencies agree well with the other measurements. The frequencies of the Doppler-limited observations are given in table 4, the estimated errors are also included.

Those rotational lines which were sufficiently intense were recorded using IMF, these were the first four N levels in the Q and R branches giving a possible total of 32 lines of which 28 were actually measured. Table 5 shows the observed IMF splittings in MHz together with the estimated measurement errors, the final column shows the effect of subtracting off the ground state contribution. For the higher rotational levels the spectra consisted of just two

Table 4. Measured wavenumbers (cm^{-1}) of lines in the (0,0) band of the $A^2\Delta$-$X^2\Pi$ transition of the CH radical

N	R_1	Q_1	P_1	$^QP_{21}$	R_2	Q_2	P_2
2		23172.5906(40)[a]		23174.3274(49)		23180.7045(70)	
		72.7510(25)		74.4868(49)		80.4524(25)	
3	23292.0212(221)	175.6447(49)			23297.3986(16)		23094.4423(12)
		76.0310(157)					93.9492(10)
4	324.1864(49)		23062.7220(90)		328.6211(35)		
	24.8482(18)	179.7608(70)			27.8018(25)	182.9436(84)	66.9023(70)
5			037.9541(35)			187.2452(12)	042.3722(84)
					359.5473(49)		41.1560(159)
6	389.6871(16)	187.6680(57)	013.9958(70)		393.5699(10)		18.1694(10)
	91.1492(16)	89.1262(90)	15.4468(22)		91.8959(16)		
7	423.0037(10)	192.8744(10)	2990.8519(90)		426.9718(10)	196.9543(22)	995.0562(18)
		94.8437(10)				94.7395(10)	
8	456.6589(16)		968.5961(10)		460.8645(16)	203.0270(16)	
	59.1977(16)	201.2612(10)	71.1357(16)		58.0461(22)	00.2038(10)	970.1884(10)
9	490.6015(16)	205.1863(31)			495.1753(16)	209.8431(10)	952.0061(22)
	93.7838(16)	08.3689(10)			91.6882(22)	06.3515(16)	
10	524.7944(22)	212.2623(16)			529.8336(16)	217.3760(16)	
	28.6671(16)	16.1436(22)				13.1593(10)	
11		219.9219(22)				225.5899(16)	
		24.5558(10)				20.5765(10)	

[a] The figures in parentheses are the estimated errors of measurement, in units of the last quoted decimal place.

Table 5. Hyperfine splittings for CH $A^2\Delta - X^2\Pi$ from IMF measurements

Line	Measured splitting	Observed value (MHz)	Observed-Ground state
$R_{1e}(1)$	$(3^+ - 2^-) - (2^+ - 1^-)$	463.8(10)[a]	443.3
$R_{1f}(1)$	$(3^- - 2^+) - (2^- - 1^+)$	441.6(30)	444.2
$R_{1e}(2)$	$(4^- - 3^+) - (3^- - 2^+)$	406.5(19)	397.5
$R_{1e}(3)$	$(5^+ - 4^-) - (4^+ - 3^-)$	404.7(30)	368.6
$R_{1f}(3)$	$(5^- - 4^+) - (4^- - 3^+)$	383.8(15)	369.8
$R_{1e}(4)$	$(6^- - 5^+) - (5^- - 4^+)$	394.9(15)	356.0
$R_{1f}(4)$	$(6^+ - 5^-) - (5^+ - 4^-)$	376.1(23)	359.2
$Q_{1e}(2)$	$(3^- - 3^+) - (2^- - 2^+)$	480.8(12)	449.3
$Q_{1f}(2)$	$(3^+ - 3^-) - (2^+ - 2^-)$	464.3(12)	455.3
$Q_{1e}(3)$	$(4^+ - 4^-) - (3^+ - 3^-)$	437.5(14)	401.4
$Q_{1f}(3)$	$(4^- - 4^+) - (3^- - 3^+)$	415.4(20)	401.4
$Q_{1f}(5)$	$(6^- - 6^+) - (5^- - 5^+)$	381.3(20)	362.5
$R_{2e}(1)$	$(1^- - 0^+) - (2^- - 1^+)$	173.9(40)	160.2
$R_{2f}(1)$	$(1^+ - 0^-) - (2^+ - 1^-)$	226.9(40)	155.2
$R_{2e}(2)$	$(2^+ - 1^-) - (3^+ - 2^-)$	232.3(14)	182.2
$R_{2f}(2)$	$(2^- - 1^+) - (3^- - 2^+)$	257.2(14)	183.8
$R_{2e}(3)$	$(3^- - 2^+) - (4^- - 3^+)$	247.7(11)	204.8
$R_{2f}(3)$	$(3^+ - 2^-) - (4^+ - 3^-)$	267.9(24)	202.6
$R_{2e}(4)$	$(4^+ - 3^-) - (5^+ - 4^-)$	257.6(23)	218.4
$R_{2f}(4)$	$(4^- - 3^+) - (5^- - 4^+)$	277.2(22)	215.9
$Q_{2e}(2)$	$(1^+ - 1^-) - (2^+ - 2^-)$	209.5(40)	159.4
$Q_{2f}(2)$	$(1^- - 1^+) - (2^- - 2^+)$	236.8(50)	163.4
$Q_{2e}(3)$	$(2^- - 2^+) - (3^- - 3^+)$	229.0(25)	186.1
$Q_{2f}(3)$	$(2^+ - 2^-) - (3^+ - 3^-)$	247.7(30)	182.4
$Q_{2e}(4)$	$(3^+ - 3^-) - (4^+ - 4^-)$	242.7(17)	203.5
$Q_{2f}(4)$	$(3^- - 3^+) - (4^- - 4^+)$	264.3(22)	203.0
$Q_{2e}(5)$	$(4^- - 4^+) - (5^- - 5^+)$	252.5(30)	215.6
$Q_{2f}(5)$	$(4^+ - 4^-) - (5^+ - 5^-)$	275.7(30)	216.8

a Figures in parentheses represent the estimated measurement error, in units of the last quoted decimal place.

Figure 8. Hyperfine structure on the $Q_{1f}(3)$ line of CH, recorded by the technique of intermodulated fluorescence. The transitions are labeled by the values of the quantum numbers F and F′. The splitting arises primarily from proton hyperfine structure in the $A^2\Delta$ state but also contains a small ground state contribution.

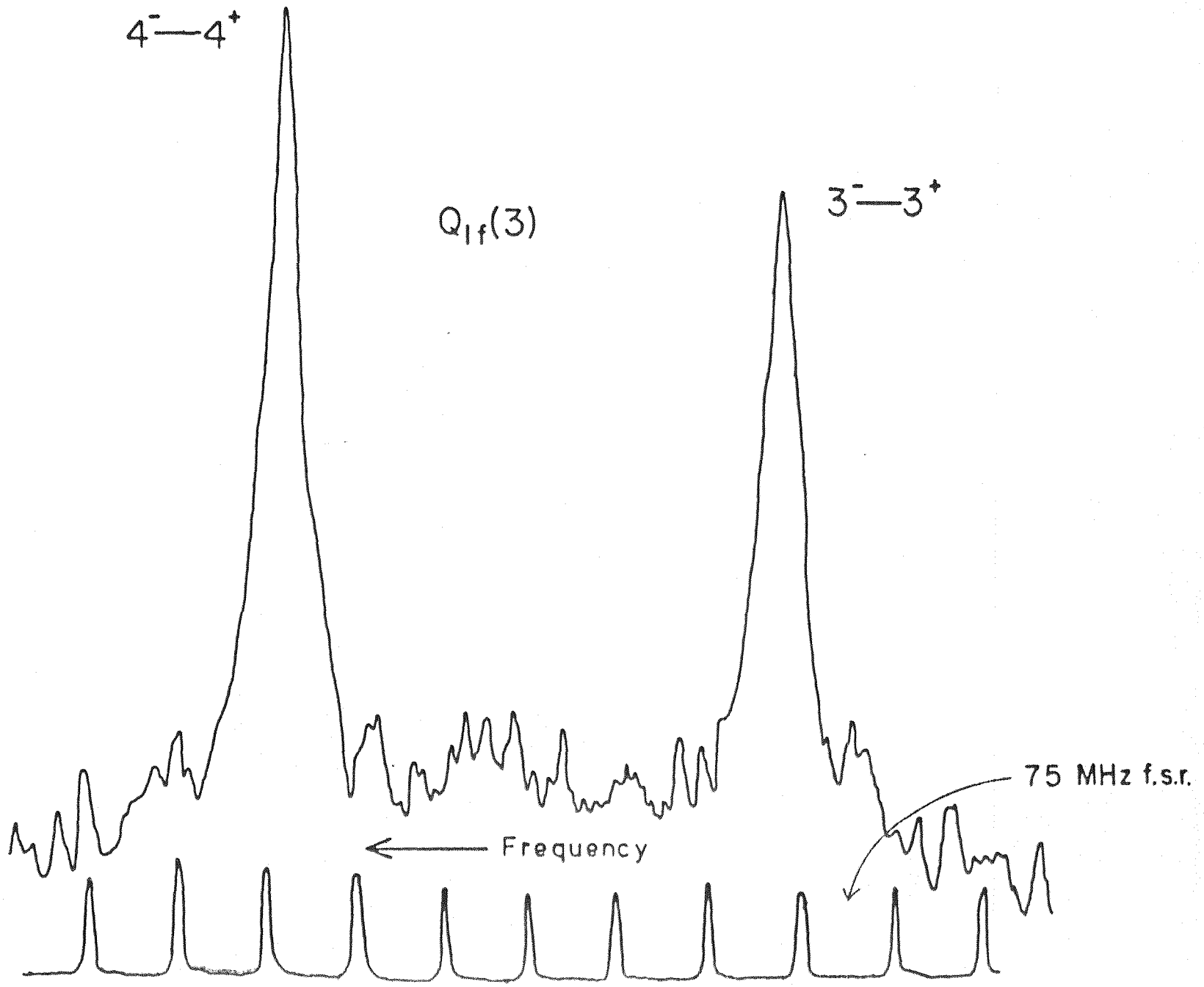
4⁻—4⁺
Q1f(3)
3⁻—3⁺
75 MHz f.s.r.
Frequency

lines split by the proton hyperfine interaction, this is a combination of the ground and excited state hyperfine splittings, a typical example is shown in figure 8. However as the ground state hyperfine structure has been well characterised by the microwave and LMR measurements it is possible to subtract this contribution to produce pure excited state splittings. These begin quite large in the F_1 component at about 450 MHz dropping to 350 MHz by N=5, for the F_2 component the initial splitting is only 150 MHz rising to about 220 MHz. This is sufficient data to determine all three hyperfine parameters, a, b and c. The splittings in the e and f components of the $^2\Delta$ energy levels are the same to within experimental error, the differences varying in a purely random fashion. The signal to noise for the transitions was never particular high, reaching about 50:1 for the strongest rotational lines, the weakest recordings were made with a signal to noise of about 5:1, it was not considered worthwhile to try to measure any of the other still weaker lines. A time constant of 1 sec was used for the recordings, this was limited by the fact that very long scans could not be made due to instability of the laser. The width of the lines depended to some extent on the pressure at which the recordings were made, the lowest value obtained was a FWHM of 20 MHz but some transitions were recorded with a linewidth of about 50 MHz. This still represented a dramatic improvement of about two orders of magnitude on the Doppler limited recordings.

The first two R_2 branch lines show strong cross-over transitions as well as the main components. For these low rotational levels the $\Delta F = 0$ transitions have significant intensity and where two transitions both from the same level occur, a cross-over signal can be produced between the main components, the intensity being the geometric mean of the signals giving rise to it. Figure 9 shows the $R_2(1)$ lines where this type of effect occurs. In the $R_{2f}(1)$ component the $F = 1 \leftarrow 1$ transition can be seen as a weak feature between the other components, for the $R_{2e}(1)$ line this transition is overlapped by the stronger components. In both cases the

Figure 9. Cross-over signals observed for the $R_2(1)$ lines of the $A^2\Delta - X^2\Pi$ system of CH. The main components 1 - 0 and 2 - 1 show the normal intensity variation for very low F transitions, which makes determination of the sign of the hyperfine constants possible. For $R_{2f}(1)$ the weak satellite 1 - 1 line is also visible, this line is overlapped for $R_{2e}(1)$. The cross-over signals are marked with asterisks.

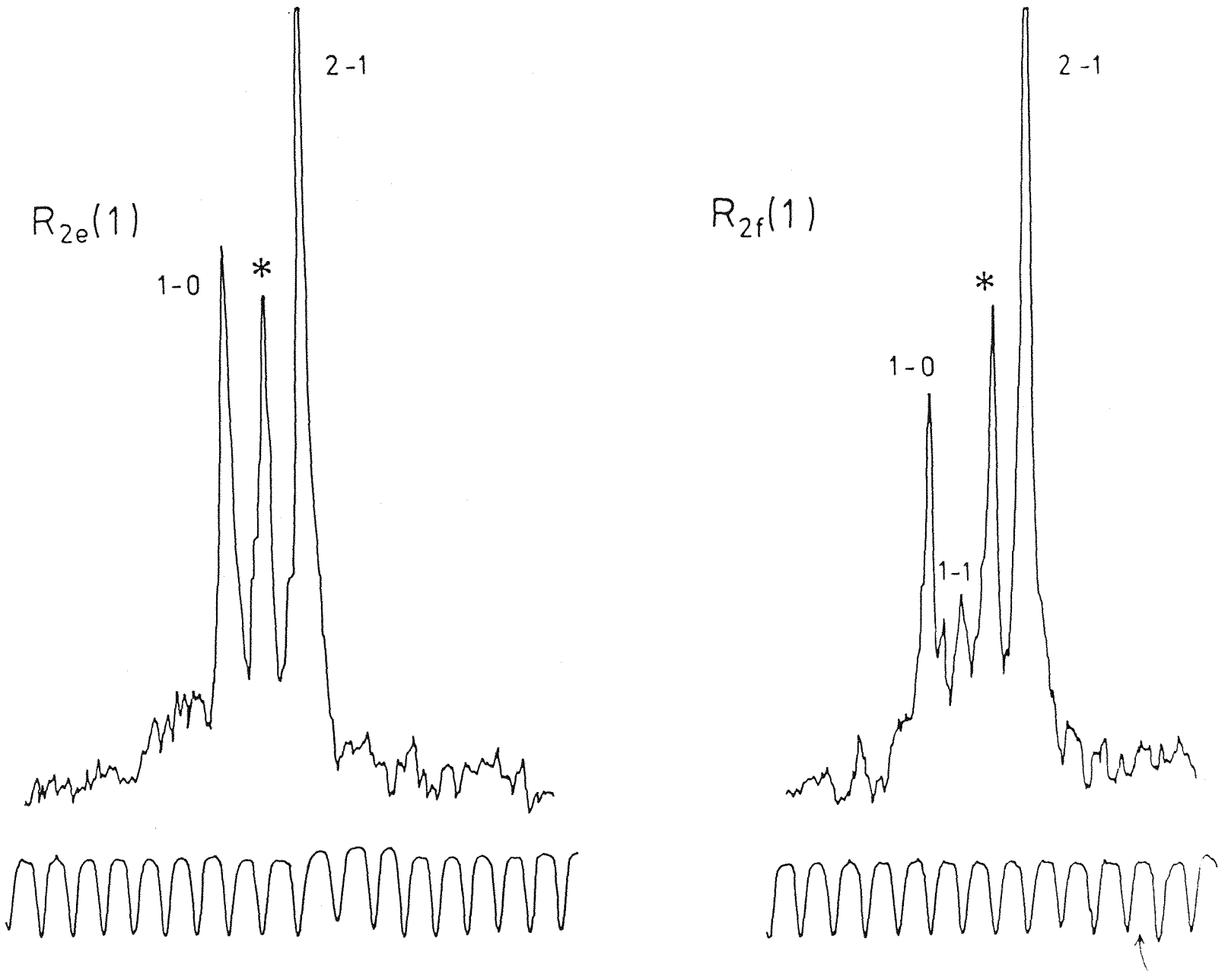
$R_{2e}(1)$
2-1
1-0
*
$R_{2f}(1)$
2-1
*
1-0
1-1

Figure 10. Energy level diagram, showing the hyperfine components which give rise to the cross-over signal for the $R_{2f}(1)$ line. The extra line, marked with an asterisk, lies midway between two transitions which originate from the same ground state level. It has an intensity which is the geometric mean of the other two lines.

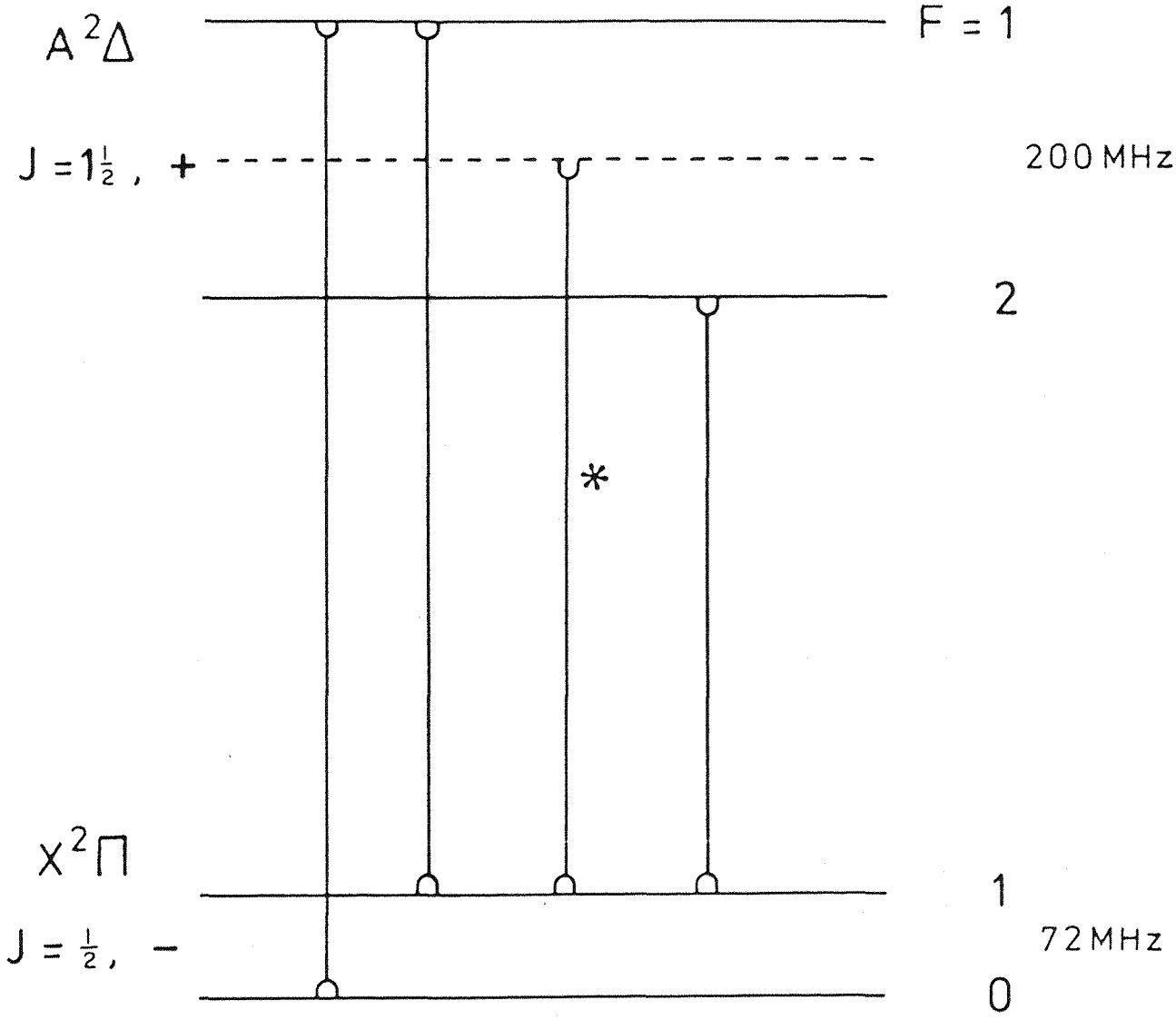

$R_{2f}(1)$ saturation spectrum

Figure 11. Unusual triplet structure on the hyperfine components of $R_{1f}(1)$ and $R_{1e}(1)$ which on subsequent re-examination was not reproducible. This structure has not so far been explained.

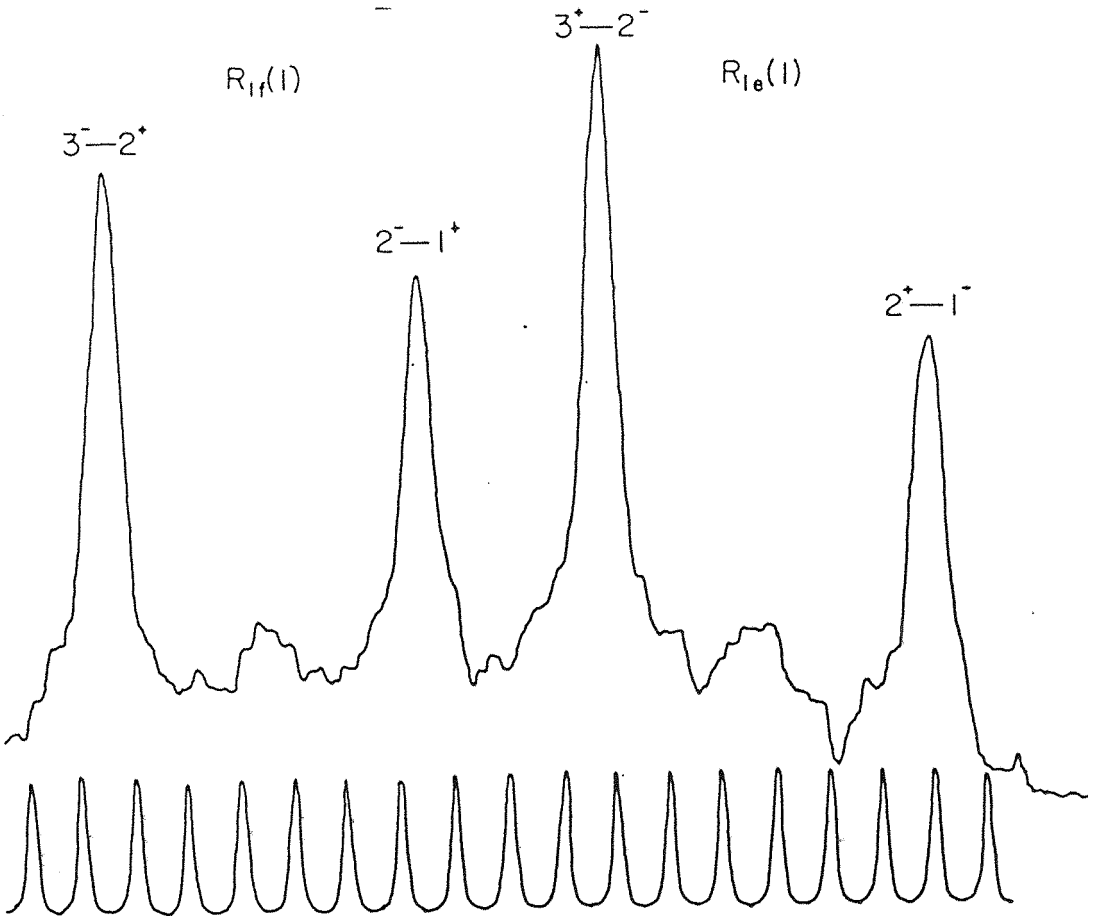
$R_{1f}(1)$
$R_{1e}(1)$
$3^- - 2^+$
$2^- - 1^+$
$3^+ - 2^-$
$2^+ - 1^-$

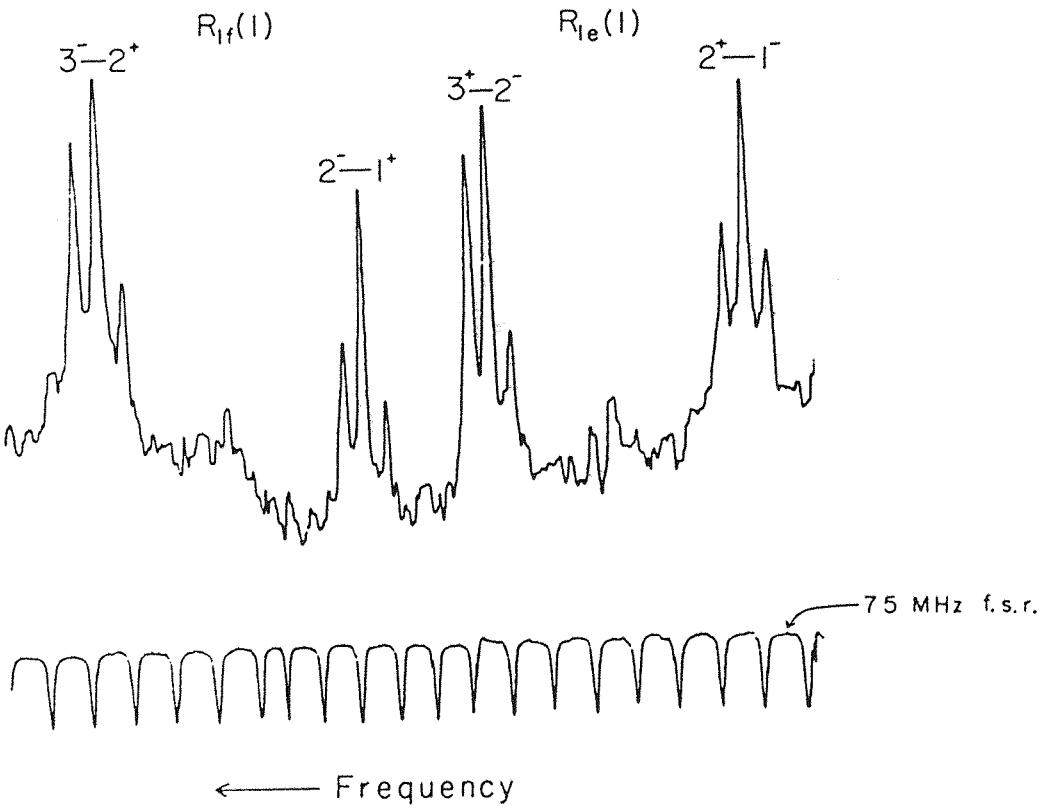
$R_{1f}(1)$
$R_{1e}(1)$
$3^- - 2^+$
$2^- - 1^+$
$3^+ - 2^-$
$2^+ - 1^-$
75 MHz f.s.r.
Frequency

cross-over transition between the 1←1 line and the strong 2←1 component is clearly visible, and is marked with an asterisk. Figure 10 shows the energy level pattern corresponding to the $R_{2f}(1)$ transitions with the hyperfine expanded greatly relative to the electronic energy difference. The cross-over transition going from the F=1 level in the $^2\Pi$ state apparently to a level lying midway between the F=1 and F=2 levels in the $^2\Delta$ state is marked with an asterisk. An explanation of how cross-over signals arise, using density matrix theory, is given by Brown et al (24). The great difference in intensity between the 2←1 and the 1←0 transitions allowed easy assignment and established the signs of the upper state hyperfine constants.

The structure of the first lines in the R_1 branch is rather more unusual. For the $R_1(1)$ transition the lambda doubling is only 780 MHz and thus at Doppler-limited resolution the $R_{1e}(1)$ and $R_{1f}(1)$ transitions are not resolved. The expected pattern, shown in figure 11a consists of four lines due to the lambda doubling and hyperfine splittings. The difference in intensity between the 3←2 and 2←1 components which allows assignment of the quantum numbers is clearly visible. Figure 11b shows the same transition recorded under slightly different conditions. Now each line from the previous spectrum shows a triplet structure with a splitting between the centre component and either of the satellites of 40 MHz. The origin of this is not easy to explain. These spectra were recorded some months apart and on each occasion were reproducible. The pressure in both cases was about 400 mTorr although it was probably slightly higher for the singlet observations. The laser power was rather different however being about 50 mWatts for the singlet observations and only 30 mWatts for the triplets. The linewidth of the singlet transitions (FWHM = 45 MHz) is somewhat greater than the triplets (FWHM = 21 MHz). This is not sufficient to obscure triplet structure as strong as shown in figure 11b, but if due to other effects the relative intensity of the centre line to the others were to change by about a factor of three, the triplet structure

would be obscured. The $R_1(2)$ transition also shows extra structure although this time only one line on the low frequency side of the main components was observed, the splitting being slightly less at 30 MHz. As before these extra lines were not seen in the later measurement. The extra lines appear to be a function of the CH molecule but they do not correspond to energy levels in CH nor are they normal cross-over transitions, these can be seen as weak features in both figures 11a and 11b.

An MODR experiment on the excited state of CH was also performed. The rotational splittings are far too large for microwave measurements while the lambda doublings are in the radio-frequency region, however as the coupling is close to the case b limit the two J levels corresponding to each N are quite close together. Observation of microwave transitions, as well as improving the excited state fine and rotational structure constants could give important information on possible lambda-doubling effects. The energy level scheme for N=6 is shown in figure 12, with the spin-rotation transitions drawn in. If there is no significant lambda doubling then each hyperfine component consists of a degenerate pair of levels one with positive and one negative parity. The lambda doubling in the ground state is large and hence it is possible to pump just one of the components in the excited state. If the optical pumping transition is switched to the other component then the microwave transition frequency should change by an amount corresponding to the sum of the lambda doublings in the two spin-rotation levels. Thus observation of these transitions should provide a fairly sensitive measure of the upper state lambda doubling. Figure 13 shows the $^2\Delta$ energy levels and the frequencies of the spin-rotation transitions are marked in. The low N frequencies are accessible using klystrons but the predictions available when the experiments were being carried out were less reliable than those now available and thus a transition for which a BWO could be used was preferable. As the N=5 transition was originally predicted to lie above the 18 GHz upper frequency limit it was decided to

Figure 12. Pumping scheme for a spin-rotation transition in N = 6 of the $A^2\Delta$ state of CH. Due to the large ground state lambda doubling it is possible to selectively pump just one of the upper state components. Hence a change in the excitation transition could lead to a change in the microwave frequency as shown.

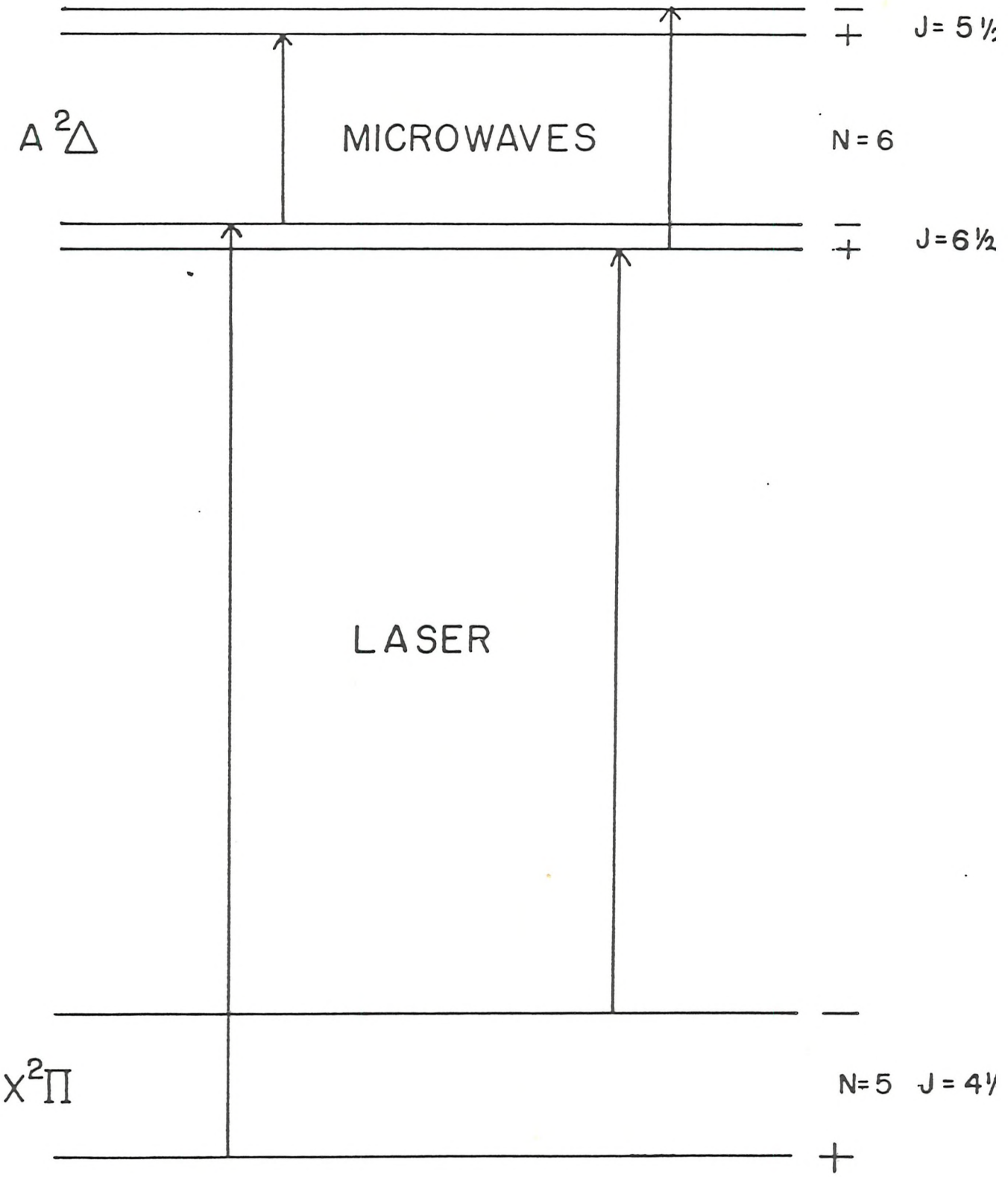
A $^2\Delta$
MICROWAVES
N = 6
J = 5½
J = 6½
LASER
$X^2\Pi$
N = 5
J = 4½

Figure 13. Energy level diagram for the $A^2\Delta$ state of CH with the possible spin-rotation transitions drawn in. Each of the J levels shown has two levels split by lambda doubling, each of these being split again by the proton hyperfine interaction.

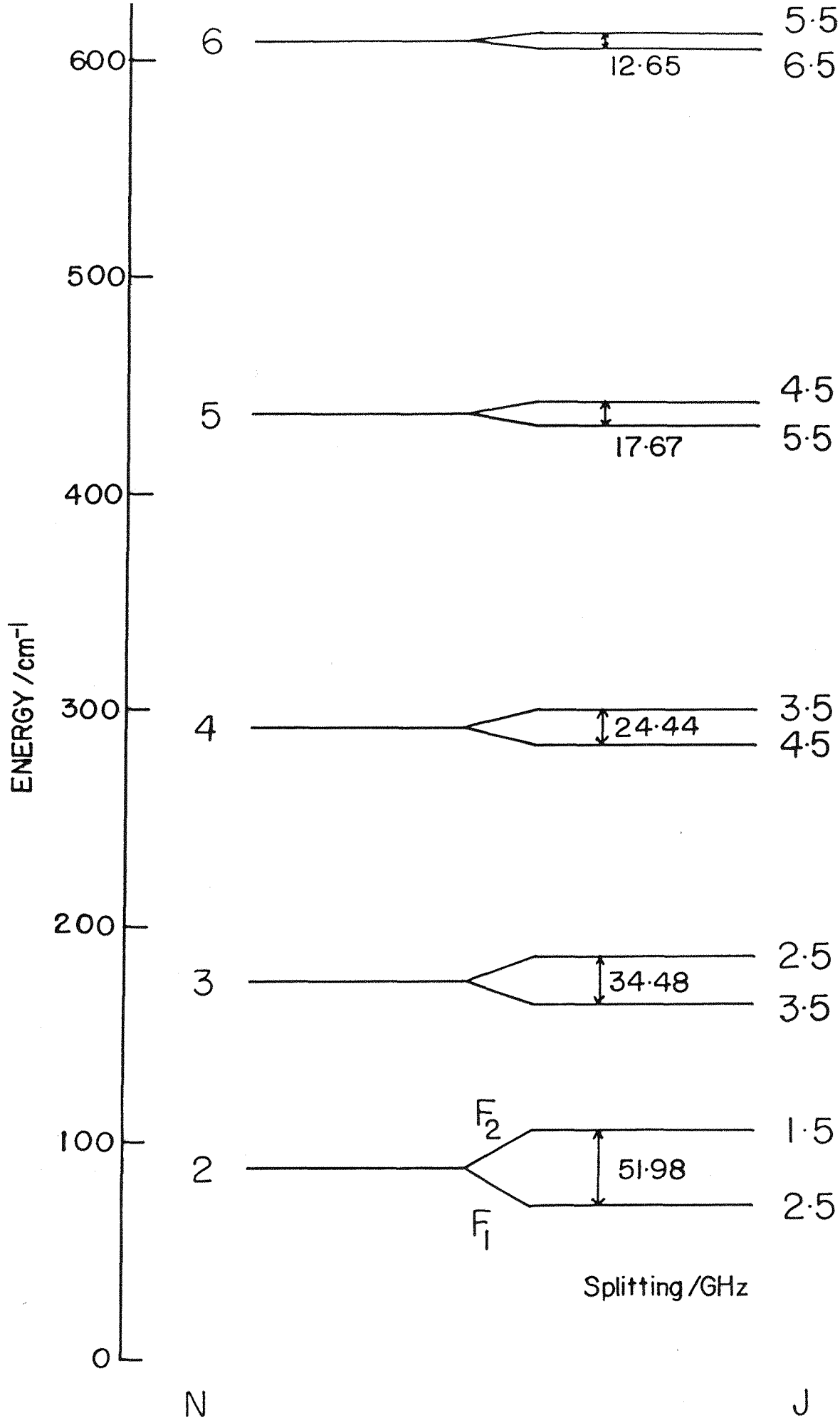
ENERGY /cm⁻¹
600
500
400
300
200
100
0
6
5
4
3
2
12·65
17·67
24·44
34·48
51·98
F2
F1
5·5
6·5
4·5
5·5
3·5
4·5
2·5
3·5
1·5
2·5
Splitting /GHz
N
J

Figure 14. Observed MODR signal in the $A^2\Delta$ state of CH. There is one line predicted near this frequency with the other main hyperfine component 570 MHz away. Either one or the other of the lines is spurious, this is not unreasonable as many times direct pick-up of the microwave radiation by the detection system led to "signals" being observed.

CH $A^2\Delta$

$N = 6,\ J = 5\frac{1}{2} \leftarrow 6\frac{1}{2},\ - \leftarrow +$

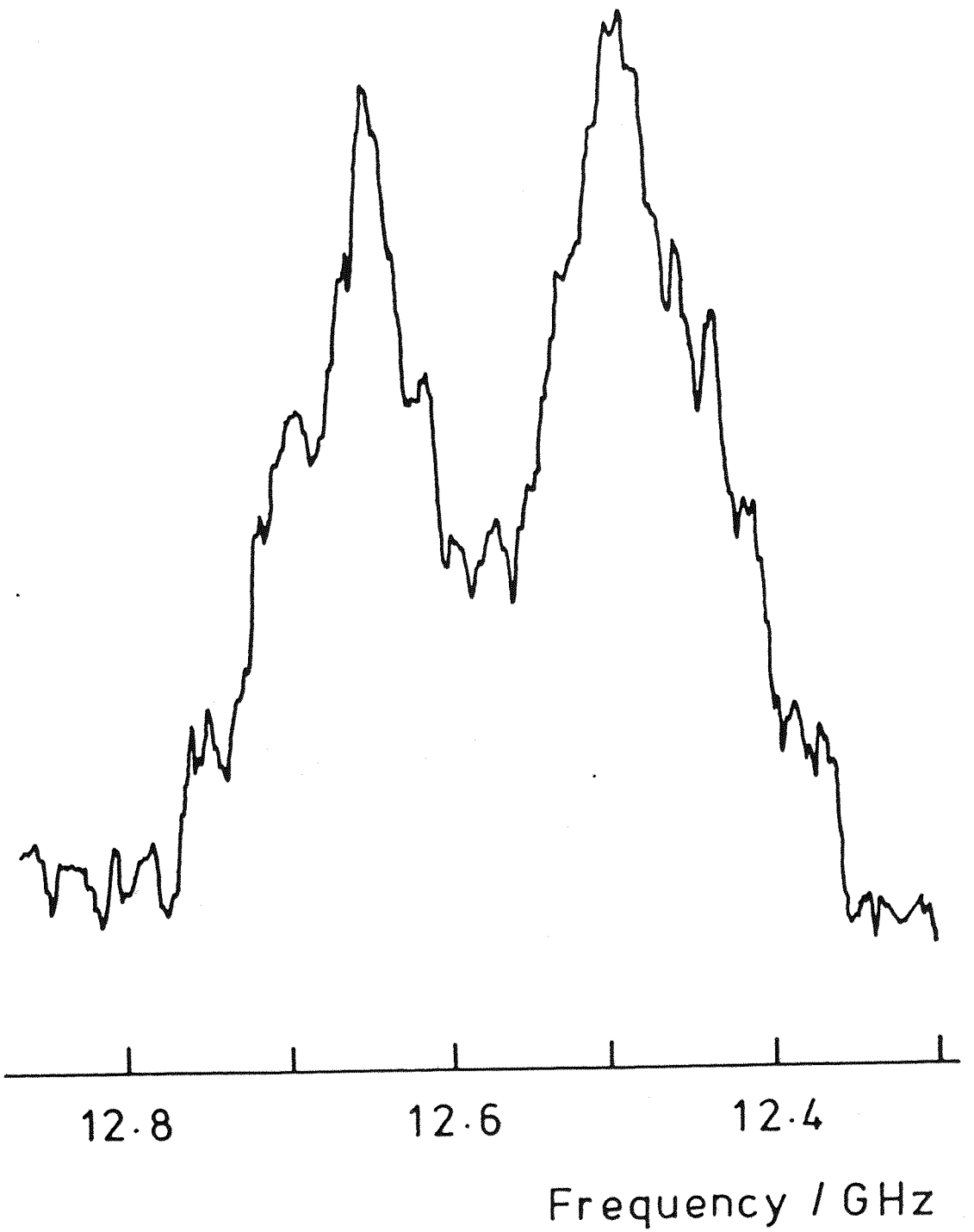

search for the N=6 transition. The hyperfine splittings in the excited state were also not very well understood and in particular the ordering of the components was not known for sure. The hyperfine splitting was estimated at 120 MHz and when two lines were observed close to the predicted position with a splitting of about this magnitude they were assumed to be the two components required. The lines observed, shown in figure 14 were very broad one about 70 MHz FWHM and the other 100 MHz. On changing the optical pump to the alternative lambda doubling component only a small shift in position, less then the measurement accuracy, was observed.

Subsequent analysis of the hyperfine structure in the excited state showed that the splittings in the two spin-rotation components went in opposite directions and thus that the expected hyperfine splitting for the observed MODR transition is 570 MHz. Hence either one or both of the signals observed was not real. During the recording of the transitions a considerable problem of direct microwave pickup by the phototube and its associated electronics was encountered giving rise to laser independent signals. Although a check was made on these observations, by blocking the laser beam, it is possible that when one component was found to be real the other was not checked. Another possibility is that the signal in figure 14 is just one transition with the same one with opposite phase due to different relaxation processes superimposed on it, features of this type have been observed before in the excited state of NO_2 by Steimle (25) and by Takami (26). It is unfortunate that the upper state MODR observations were not properly obtained, as they would give important information on the fine and rotational structure as well as the lambda doubling and hyperfine effects.

Fit of the Data

Due to the great accuracy with which the ground $^2\Pi$ state parameters have been determined for CH, it was possible to reduce the various A-X transitions observed to

pure excited state values. The Doppler-limited data were fitted as transitions however, as it was easier for the program to calculate the $^2\Pi$ energies each time, than to evaluate the $^2\Delta$ term values. A computer program was written to calculate the $A^2\Delta - X^2\Pi$ transition frequencies and to fit the upper state constants by the least squares method. The ground state constants were constrained to the values determined from the LMR and microwave fits as these were considered to be more accurate than any values which could be found by fitting them. No hyperfine effects were included in either state, for the ground state all of the constants from the previous fits were used, while for the excited state A, B, D, H, γ, γ_D, p and q were included, together with the (0,0) transition frequency. There are great variations in the accuracies of the measured frequencies and hence a weighted fit was required, each line being weighted according to the inverse square of its overall measurement error as given in table 4. Previous fits of $A^2\Delta - X^2\Pi$ data had resulted in approximate values for A,B and D and these were used as initial estimates. Initially only A, B, D and γ were allowed to vary, the result was quite good but many of the high N lines which were the most accurately measured, were not fitted to the precision expected. The inclusion of higher order terms γ_D and H gave quite a considerable improvement, the standard deviation of fit being 1.28.

The only remaining question was whether the lambda doubling parameters for the excited state could be determined. As a check on this the computer scanned measurements were used to produce a set of lambda doubling frequencies, with each splitting due almost entirely to the ground state, but fortunately the microwave measurements had been made to quite high N and it was possible to extrapolate them to the rotational levels required,upto N=11. Table 6 shows the measured splittings and also the effect of subtracting the ground state lambda doubling to leave pure $^2\Delta$ splittings. While the values show rather wild fluctuations, as they are only just larger than the measurement

Table 6. Lambda doubling in the $A^2\Delta$ state of CH

Transition	Measured splitting (GHz)	Ground state contribution (GHz)	Upper state splitting (MHz)	Upper state level
$P_1(8)$	76.135	76.158	23	F_1 7
$Q_1(7)$	59.038	58.997	41	F_1 7
$R_1(6)$	43.833	43.862	29	F_1 7
$Q_1(8)$	76.294	76.158	136	F_1 8
$R_1(7)$	58.858	58.997	139	F_1 8
$Q_1(9)$	95.412	95.263	149	F_1 9
$R_1(8)$	76.111	76.158	47	F_1 9
$Q_1(10)$	116.358	116.223	135	F_1 10
$R_1(9)$	95.253	95.263	10	F_1 10
$Q_1(11)$	138.921	138.941	-20	F_1 11
$R_1(10)$	116.101	116.223	122	F_1 11
$P_2(8)$	84.365	84.524	159	F_2 7
$Q_2(7)$	66.398	66.411	-13	F_2 7
$R_2(6)$	50.185	50.311	126	F_2 7
$P_2(9)$	104.451	104.568	117	F_2 8
$Q_2(8)$	84.682	84.524	158	F_2 8
$R_2(7)$	66.461	66.411	-50	F_2 8
$Q_2(9)$	104.676	104.568	108	F_2 9
$R_2(8)$	84.494	84.524	30	F_2 9
$Q_2(10)$	126.413	126.451	-38	F_2 10
$R_2(9)$	104.541	104.568	27	F_2 10
$Q_2(11)$	150.298	150.076	222	F_2 11

Table 7. Fit of $^2\Delta$ lambda doubling splittings

Level	Splittings / MHz		
	Observed	Calculated	Obs-Calc
F_1 N = 7	29	21	8
F_1 N = 8	141	39	102
F_1 N = 9	104	54	50
F_1 N = 10	84	89	-5
F_1 N = 11	70	128	-58
F_2 N = 7	90	30	60
F_2 N = 8	76	51	25
F_2 N = 9	71	83	-12
F_2 N = 10	-3	114	-117
F_2 N = 11	245	169	76

Lambda doubling parameters

$p + 4q = 0.06(5)$ MHz

$q = 0.009(2)$ MHz

Table 8. Fit of the (0,0) band of the $A^2\Delta - X^2\Pi$ transition of CH

Line	Observed cm^{-1}	Obs-Calc cm^{-1}	Line	Observed cm^{-1}	Obs-Calc cm^{-1}
$R_{1e}(3)$	23292.0212	.0143	$R_{2e}(3)$	23297.3986	.0012
$R_{1e}(4)$	23324.1864	.0015	$R_{2e}(4)$	23328.6211	-.0036
$R_{1f}(4)$	23324.8482	-.0018	$R_{2f}(4)$	23327.8018	-.0080
$R_{1e}(6)$	23389.6871	.0018	$R_{2f}(5)$	23359.5473	.0074
$R_{1f}(6)$	23391.1492	.0013	$R_{2e}(6)$	23393.5699	-.0015
$R_{1e}(7)$	23423.0037	.0003	$R_{2f}(6)$	23391.8959	.0023
$R_{1e}(8)$	23456.6589	.0005	$R_{2e}(7)$	23426.9718	.0003
$R_{1f}(8)$	23459.1977	.0002	$R_{2e}(8)$	23460.8645	.0002
$R_{1e}(9)$	23490.6015	-.0042	$R_{2f}(8)$	23458.0461	.0002
$R_{1f}(9)$	23493.7838	.0022	$R_{2e}(9)$	23495.1753	.0005
$R_{1e}(10)$	23524.7944	-.0008	$R_{2f}(9)$	23491.6882	-.0002
$R_{1f}(10)$	23528.6671	-.0023	$R_{2e}(10)$	23529.8336	.0008
$Q_{1e}(2)$	23172.5906	.0013	$Q_{2e}(2)$	23180.7045	.0065
$Q_{1f}(2)$	23172.7510	-.0003	$Q_{2f}(2)$	23180.4524	-.0008
$Q_{1e}(3)$	23175.6447	.0020	$Q_{2f}(4)$	23182.9436	.0126
$Q_{1f}(3)$	23176.0310	.0122	$Q_{2e}(5)$	23187.2452	.0009
$Q_{1f}(4)$	23179.7608	.0153	$Q_{2e}(7)$	23196.9543	-.0004
$Q_{1e}(6)$	23187.6680	.0111	$Q_{2f}(7)$	23194.7395	.0005
$Q_{1f}(6)$	23189.1262	.0060	$Q_{2e}(8)$	23203.0270	.0023
$Q_{1e}(7)$	23192.8744	-.0010	$Q_{2f}(8)$	23200.2038	-.0007
$Q_{1f}(7)$	23194.8437	-.0001	$Q_{2e}(9)$	23209.8431	-.0016
$Q_{1f}(8)$	23201.2612	-.0026	$Q_{2f}(9)$	23206.3515	-.0041
$Q_{1e}(9)$	23205.1863	-.0040	$Q_{2e}(10)$	23217.3760	-.0019
$Q_{1f}(9)$	23208.3689	-.0002	$Q_{2f}(10)$	23213.1593	.0010
$Q_{1e}(10)$	23212.2623	-.0003	$Q_{2e}(11)$	23225.5899	.0017
$Q_{1f}(10)$	23216.1436	.0025	$Q_{2f}(11)$	23220.5765	-.0034
$Q_{1e}(11)$	23219.9219	.0030	$P_{2e}(3)$	23094.4423	.0000
$Q_{1f}(11)$	23224.5558	-.0001	$P_{2f}(3)$	23093.9492	-.0004
$P_{1e}(4)$	23062.7220	.0060	$P_{2f}(4)$	23066.9023	.0002
$P_{1e}(5)$	23037.9541	-.0067	$P_{2e}(5)$	23042.3722	.0068
$P_{1e}(6)$	23013.9958	.0126	$P_{2f}(5)$	23041.1560	.0013
$P_{1f}(6)$	23015.4468	.0007	$P_{2e}(6)$	23018.1694	-.0006
$P_{1e}(7)$	22990.8519	.0041	$P_{2e}(7)$	22995.0562	-.0029
$P_{1e}(8)$	22968.5961	.0001	$P_{2f}(8)$	22970.1884	.0007
$P_{1f}(8)$	22971.1357	-.0002	$P_{2e}(9)$	22952.0061	.0028
$^{Q}P_{21e}(2)$	23174.3274	.0039	$^{Q}P_{21f}(2)$	23174.4868	.0012

Parameters for the v=0 level of $A^2\Delta$ CH

TE	=	23173.458(1)	$\tilde{\gamma}$	=	0.024228(22)
$\tilde{A}$	=	-1.0993(14)	$10^4\ \gamma_D$	=	-0.146(19)
B	=	14.579175(67)	10^6 p	=	-0.1(10)
10^2 D	=	0.15673(10)	10^6 q	=	0.143(49)
10^6 H	=	0.1019(46)			

[a] Numbers in parentheses represent one standard deviation error estimates, in units of the last quoted decimal place.

Correlation matrix

	TE	A	B	D	H	γ	γ_D	p	q
TE	1.000	.786	-.909	-.787	-.685	-.526	.354	-.046	.029
A		1.000	-.669	-.553	-.473	-.780	.591	-.035	.017
B			1.000	.968	.916	.505	-.367	.063	-.035
D				1.000	.986	.448	-.343	.059	-.033
H					1.000	.404	-.322	.061	-.031
γ						1.000	-.937	.035	-.002
γ_D							1.000	-.032	-.064
p								1.000	-.025
q									1.000

errors, it is clear that a significant residual effect remains. The splittings are about the same for values from the P, Q and R branches. If the ground state splittings had not been correct then some variation between the results from the different branches would be expected. The upper state splittings should show a quite rapid increase with N, but this is masked somewhat by the large random variations. The splittings for F_1 and F_2 are also quite similar, this was expected from estimates of the parameters. The $^2\Delta$ lambda doublings were reduced to a set of ten splittings by averaging the results from the different branches, these were then fitted to p and q with all of the other upper state parameters constrained to the previously determined values. The results of this calculation together with the parameters determined are given in table 7. The standard deviation of fit 71 MHz, was about as expected, considering the lack of precision for the data. The value of q is fairly well determined, this contributes to the overall lambda doubling in both F_1 and F_2 while p, which contributes only to the difference in the two, which can be seen from table 7 to be small, is not quite determined.

To further check the upper state lambda-doubling the values of p and q were allowed to vary in the overall $^2\Delta$ fit, this led to a slightly improved standard deviation of 1.23. The results of this fit were given in table 4 and the parameters determined are shown in table 8. The values for p and q agree with those from the previous fit to within one standard devition. The overall quality of fit is slightly above the expected value but is clearly acceptable as the errors on the measurements could not be estimated all that accurately. A few lines with very large errors were removed from the fit, but this had little effect as their weights were fairly low. The quality of fit for the other remaining measurements was good with only a few being out by more than twice their measurement error, however this is to be expected on a purely statistical basis and it was not thought proper to exclude them from the fit. All of the parameters, except for p, were well determined and as can be

Table 9. Fit of the hyperfine data for $A^2\Delta$ CH

Level	Splittings in MHz		
	Observed	Calculated	Obs-Calc
F_1 N = 2	448.0	449.6	-1.6
F_1 N = 3	401.4	399.6	1.8
F_1 N = 4	369.2	372.4	-3.2
F_1 N = 5	359.2	355.3	3.9
F_2 N = 2	159.6	158.4	1.2
F_2 N = 3	183.6	185.4	-1.8
F_2 N = 4	203.5	203.9	-0.4
F_2 N = 5	216.7	216.7	0.0

Parameters determined

a = 57.26(85)

b = 563.6(34)

c = 61.4(80)

Standard deviation of fit = 2.7 MHz

seen from table 8 no unacceptable correlations between parameters were found.

The IMF hyperfine measurements were fitted independently of the Doppler-limited data and with the fine and rotational structure constants constrained to their previously determined values. The observed splittings given in table 5 were reduced to a set of eight splittings from N=2 to N=5 for the F_1 and F_2 components, by combining the different measurements, these are given in table 9a. The splittings in upper state e and f levels are also given and it is clear that there is no significant difference between the two sets of numbers. Any difference would correspond to a lambda doubling type hyperfine splitting, this is expected to be very small for a $^2\Delta$ state, the lack of any noticable effect puts an upper limit on the lambda doubling type hyperfine of about 2 MHz. Due to the different intensities of the hyperfine components at low N it was possible to assign the correct F quantum numbers for them, the higher N lines have been assigned by following the clear trends in the splittings, from low N. The result of this is definite signs for the hyperfine parameters, in particular b which determines the high N splitting is defined and once this is known a and c which contribute to the change in structure at lower N are defined. The eight splittings were input to a least squares computer program together with trial values for a, b and c, the results of the fit are shown in table 9a while 9b gives the parameters determined. The overall unweighted standard deviation of fit is 2.7 MHz which agrees well with the estimated measurement errors given in tables 5 and 9a. All three hyperfine parameters are well determined although the error for c is quite large. Inspection of the correlation matrix shows that none of the parameters are highly correlated to each other. Clearly sufficient information was available in the measured splittings, although further measurements at higher N would have given slightly more acccurate parameters as would successful recording of the upper state MODR spectrum.

6.7 Discussion

A total of eleven effective Hamiltonian parameters were used to describe the $A^2\Delta$ state of CH together with a value for the (0,0) energy separation between the $A^2\Delta$ and $X^2\Pi$ states. Of these all but p were determined. The spin-orbit constant A for the $^2\Delta$ state at $-1.1\ cm^{-1}$ is extremely small when compared with the ground state value of $28\ cm^{-1}$. This is because in the $^2\Delta$ state there are two electrons in the $p\pi$ orbital which constitutes a half filled shell. The effects due to spin-orbit coupling with the two electrons thus almost cancel out and the value of A is close to zero. This effect is fairly general for $^2\Delta$ states where the orbital angular momentum is provided by $p\pi$ electrons for example

	A_o/cm^{-1}
CH	-1.1
NH^+	-3.6
SiH	3.6
PH^+	1.4

All values except for CH are taken from ref 19.

A total of three rotational constants B, D and H were required to describe the observed transitions. However only the values for $v = 0$ were determined and thus equilibrium values and anharmonicity corrections cannot be evaluated. The calculated value for H is $0.77 \times 10^{-7}\ cm^{-1}$ compared with the experimental value of $1.01 \times 10^{-7}\ cm^{-1}$. This discrepancy contains the combined effects of deviation from the calculated values in both the $X^2\Pi$ and $A^2\Delta$ states as the calculated ground state value has been used throughout this analysis. The difference is not sufficiently large however to render the assumed calculated value for the ground state invalid.

Whilst the determination of improved fine and rotational structure constants for the $A^2\Delta$ state is of some importance, the main object of the LIF measurement was to determine the size of the lambda doubling in the $^2\Delta$ state.

Unfortunately it was only possible to determine one parameter, q, as the data were of just sufficient accuracy to show the lambda doubling effects. The lambda doubling in the $^2\Delta$ state is very small as it only arises in the fourth order of perturbation theory. The splittings are produced by interactions with $^2\Sigma$ states which can only occur via an intermediate $^2\Pi$ state which is in this case assumed to be the ground state. It is possible to estimate the size of the lambda doubling by theoretical calculations, the values for p and q being given by the following expressions

$$p = -4 \sum (E_\Delta - E_\Pi)^{-2}(E_\Delta - E_\Sigma)^{-1}\langle {}^2\Delta_{3/2}|\mathcal{H}_{so}|{}^2\Pi_{3/2}\rangle \qquad 6.12$$
$$\langle {}^2\Pi_{3/2}|BL_+|{}^2\Sigma_{1/2}\rangle\langle {}^2\Sigma_{1/2}|BL_+|{}^2\Pi_{-1/2}\rangle\langle {}^2\Pi_{-1/2}|BL_+|{}^2\Delta_{-3/2}\rangle$$
$$-4 \sum (E_\Delta - E_\Pi)^{-2}(E_\Delta - E_\Sigma)^{-1}\langle {}^2\Delta_{3/2}|BL_+|{}^2\Pi_{1/2}\rangle$$
$$\langle {}^2\Pi_{1/2}|\mathcal{H}_{so}|{}^2\Sigma_{1/2}\rangle\langle {}^2\Sigma_{1/2}|BL_+|{}^2\Pi_{-1/2}\rangle\langle {}^2\Pi_{-1/2}|BL_+|{}^2\Delta_{-3/2}\rangle$$

$$q = 2 \sum (E_\Delta - E_\Pi)^{-2}(E_\Delta - E_\Sigma)^{-1}\langle {}^2\Delta_{5/2}|BL_+|{}^2\Pi_{3/2}\rangle \qquad 6.13$$
$$\langle {}^2\Pi_{3/2}|BL_+|{}^2\Sigma_{1/2}\rangle\langle {}^2\Sigma_{1/2}|BL_+|{}^2\Pi_{-1/2}\rangle\langle {}^2\Pi_{-1/2}|BL_+|{}^2\Delta_{-3/2}\rangle$$

The spin representations for the $^2\Pi$, $^2\Sigma^+$ and $^2\Sigma^-$ states have been given in section 6.5, those for the $^2\Delta$ state are as follows

$^2\Delta_{5/2}$	$\|\sigma\pi_+\bar{\pi}_+\|$
$^2\Delta_{-5/2}$	$\|\sigma\pi_-\bar{\pi}_-\|$
$^2\Delta_{3/2}$	$\|\bar{\sigma}\pi_+\bar{\pi}_+\|$
$^2\Delta_{-3/2}$	$\|\bar{\sigma}\pi_-\bar{\pi}_-\|$

Most of the elements in eqns 6.12 and 6.13 have been evaluated in section 6.5, the others are given below

$$\langle {}^2\Delta_{3/2}|\mathcal{H}_{so}|{}^2\Pi_{3/2}\rangle = \langle\bar{\pi}_+|\mathcal{H}_{so}|\sigma\rangle = 1/2\zeta\langle\bar{\pi}_+|L_+|\bar{\sigma}\rangle = 1/\sqrt{2}\,\zeta$$
$$\langle {}^2\Delta_{3/2}|BL_+|{}^2\Pi_{1/2}\rangle = -\langle\pi_+|BL_+|\sigma\rangle = -\sqrt{2}\,B$$
$$\langle {}^2\Delta_{5/2}|BL_+|{}^2\Pi_{3/2}\rangle = -\langle\bar{\pi}_+|BL_+|\bar{\sigma}\rangle = -\sqrt{2}\,B$$
$$\langle {}^2\Sigma^+_{1/2}|BL_+|{}^2\Pi_{-1/2}\rangle = -1/\sqrt{2}\langle\bar{\pi}_+|BL_+|\bar{\sigma}\rangle = -B$$
$$\langle {}^2\Pi_{-1/2}|BL_+|{}^2\Delta_{-3/2}\rangle = -\langle\bar{\sigma}|BL_+|\bar{\pi}_-\rangle = -\sqrt{2}\,B$$
$$\langle {}^2\Sigma^-_{1/2}|BL_+|{}^2\Pi_{-1/2}\rangle = 1/\sqrt{6}(-2\langle\pi_+|BL_+|\sigma\rangle - \langle\bar{\pi}_+|BL_+|\bar{\sigma}\rangle = -\sqrt{3}\,B$$

Substituting these terms in the expressions for p and q gives

$$p = -4(E_\Delta - E_\pi)((-\zeta B^3 - \zeta B^3)(E_\Delta - E_{\Sigma^+})^{-1} + (3\zeta B^3 - \zeta B^3)(E_\Delta - E_{\Sigma^-})^{-1}) \quad 6.14$$

$$q = 2(E_\Delta - E_\pi)^{-2}((2B^4)(E_\Delta - E_{\Sigma^+})^{-1} + (-6B^4)(E_\Delta - E_{\Sigma^-})^{-1}) \quad 6.15$$

substituting $B = 14.6\ cm^{-1}$ $\zeta = 27.5\ cm^{-1}$
and taking the energy separations (19) as

$$E_\Delta - E_\pi = 23217.5\ cm^{-1}$$
$$E_\Delta - E_{\Sigma^+} = -8560.6\ cm^{-1}$$
$$E_\Delta - E_{\Sigma^-} = -2480.7\ cm^{-1}$$

gives

$$p = 4.0 \times 10^{-7}\ cm^{-1} \text{ and } q = 3.3 \times 10^{-7}\ cm^{-1}$$

As a comparison the experimental values with two standard deviations for the error are

$$p = 10.\ (24) \times 10^{-7}\ cm^{-1} \text{ and } q = 1.5\ (12) \times 10^{-7}\ cm^{-1}$$

Clearly the value for p is not determined and thus no comparison can be made. The experimental value for q is somewhat lower than the calculated one but the error on this is quite large and it is possible for the true value to be somewhat closer. The numbers are in fair agreement however and provide confirmation both of the somewhat marginal experimental data and of the origin of those terms on which the calculations above were based. It would be nice to have slightly more accurate experimental values for the lambda doubling constants so that a more stringent test of the theoretically calculated values could be made. These could be provided by measuring the spin-rotation transitions in the $^2\Delta$ state using MODR and by recording the LIF spectra of higher temperature CH sources to the same precision as was obtained here. Even so this first observation of lambda

doubling in the $A^2\Delta$ state is of some importance and shows that such effects can not be neglected.

A calculation of the spin-rotation parameter γ can also be made in the same way as for the ground state. The main contribution is going to come from the interaction with the $X^2\Pi$ state and this has already been calculated in section 6.5. The sign of the previous result must be changed as the order of the states being considered is reversed, this gives γ as follows

$$\gamma = 1007 \text{ MHz}$$

As a comparison the experimentally determined value is

$$\gamma = 1264 \text{ (16) MHz}$$

This is in quite good agreement, but a pssible cause of the discrepancy is the neglect of interactions with other high lying $^2\Pi$ states one of which is likely to arise from the $1\sigma^2 2\sigma^2 1\pi^3$ configuration which can interact with the $A^2\Delta$ state.

A total of three hyperfine parameters a, b and c were determined for the $A^2\Delta$ of CH. The electronic configuration of the $^2\Delta$ state is

$$1\sigma^2 2\sigma^2 3\sigma^1 1\pi^2$$

and thus the main contribution to the hyperfine effects arises fronm the unpaired 3σ electron which is primarily in a carbon $2p\sigma$ orbital. The hyperfine constants are given by the following expressions

$$a/cm^{-1} = \mu_o/4\pi hc \sum_i 2\mu_B g_N \mu_N \langle 1/r^3 \rangle \qquad 6.15$$

$$b_F/cm^{-1} = \mu_o/hc \sum_i (2/3) g_i \mu_B g_N \mu_N \langle \delta(r_i) \rangle \qquad 6.16$$

$$c/cm^{-1} = \mu_o/4\pi hc \sum_i (3/2) g_i \mu_B g_N \mu_N \langle (3\cos^2\theta_i - 1)/r^3 \rangle \qquad 6.17$$

The nuclear-spin orbit interaction a depends only on $\langle 1/r^3 \rangle$ and as the radial wavefunction for a carbon 2pσ orbital is the same as for a 2pπ orbital the value of a should be the same for the excited state as for the $X^2\Pi$ state of CH. The values obtained are as follows with 2 standard deviation errors in brackets

$X^2\Pi$ a = 54.3 (3) MHz

$A^2\Delta$ a = 57.3 (17) MHz

These two results are quite close and provide confirmation for the assumed carbon 2p nature of the unpaired electron.

The experimental data were fitted using Frosch and Foley's b rather than b_F as this is the parameter which actually determines the splitting. However the value of c was also determined and this can be used to obtain an estimate of the Fermi contact term

$$b_F = b - 1/3\ c = 543.\ (9)\ MHz$$

This contains contributions from the 2pσ orbital density at the proton together with any hydrogen 1s contribution. The 2pσ wavefunction may be written as a Slater type orbital

$$\psi = 1/(4(2\pi)^{1/2})\ K^{3/2}\rho\exp(-\rho/2)\cos\theta \qquad 6.18$$

where

K = Z/ao

Z = 3.18 by Slater's rules

ao = 5.29×10^{-11} m the Bohr radius

ρ = Kr

r = the distance from the electron to the carbon nucleus

θ = the angle between a straight line to the electron and the C-H bond

It is required to evaluate $|\psi|^2$ at the proton and thus r = ro the C-H bond length in the υ = 0 vibrational level

and $\theta = 0°$, thus $\cos\theta = 1$.

$$B_o = 14.57916\ cm^{-1} = h/(8\pi^2\mu r^2)$$

where μ is the reduced mass of CH

this gives $r_o = 1.115195 \times 10^{-10}$ m

and thus $|\psi|^2 = 1.19 \times 10^{29}\ m^{-3}$

substituting this value in the expression for the Fermi contact term gives

$$b_F = 78.9\ MHz$$

Thus the carbon 2pσ electron is expected to make quite a significant contribution to the Fermi contact interaction but this still leaves a large amount unaccounted for and this must be due to an appreciable hydrogen 1s contribution to the molecular orbital containing the unpaired electron. Substracting off the 2pσ contribution gives

$$b_F\ (H1s) = 464\ MHz$$

The Fermi contact term for one electron in a hydrogen 1s orbital is 1420 MHz (27) which means that the b_F value for CH corresponds to a hydrogen 1s contribution of 32.6%. This rather contradicts the earlier calculations based on carbon 2p orbitals but it appears that near the carbon nucleus this is quite a good representation but that as the proton is approached it is neccessary to include the hydrogen 1s contribution to the molecular orbital.

To estimate a value for c the expectation value $\langle\psi|(3\cos^2\theta-1)/r^3|\psi\rangle$ must be evaluated. The Slater type orbital given above may be used to represent ψ and it is

necessary to calculate

$$\int_0^{\infty}\int_0^{2\pi}\int_0^{\pi}\psi^2(3\cos^2\theta-1)/r^3\,(r')^2\sin\theta'\,d\phi'\,d\theta'\,dr' \qquad 6.19$$

where the primed coordinates are relative to the carbon nucleus and the unprimed ones relative to the proton. Such expressions have been evaluated for π radicals, like CH, and the following result obtained (28), with a subsequent correction (29) to take account of the contribution at the proton included.

$$\langle\psi|(3\cos^2\theta-1)/r^3|\psi\rangle = 2/R^3[1+18/a^2-(4a^5/3+2a^4+6a^3+14a^2 \qquad 6.20$$
$$+26a+37+36/a+18/a^2)\exp(-2a)]$$

where R is the CH internuclear distance and a = ZR/2ao is a dimensionless radial parameter.

Taking a = 3.352 and R = ro = 1.115×10^{-10} m gives

$$\langle\psi|(3\cos^2\theta-1)/r^3|\psi\rangle = 1.39 \times 10^{30}\ m^{-3}$$

Substituting this value in the expression for the spin dipolar term gives

$$c = 165\ MHz$$

This is somewhat larger than the experimental result

$$c = 61\ (16)\ MHz$$

As the proton contributes 32.6% towards the spin density a correction for this should be included, this gives

$$c = 111\ MHz$$

which is still somewhat larger than the experimental result.

Possible resons for this are that a significant carbon 2s contribution occurs, this would not contribute to the spin dipolar term. Also the actual expression used, is based on the effective nuclear charge Z, and slight changes to this would be likely to lead to rather large changes in the calculated value for c.

6.8 Conclusion

We have made the first laboratory observations of the microwave spectrum of CH. The very high signal to noise obtained on these measurements shows the great increase in sensitivity which can be obtained when the technique of MODR is used rather than conventional microwave absorption spectroscopy. These observations together with the other microwave results and the LMR measurements have resulted in a very accurate characterisation of the $X^2\Pi$ state of CH. The high precision of these measurements has already led to the observation of two new CH lines in the interstellar medium, and it is hoped that many more will be seen in the future. This will provide important information on the extent of rotational excitation of CH in different astrophysical sources.

The $A^2\Delta$ state for which previously only the spin orbit and rotational constants were known has also been extensively examined and the fine and hyperfine structure characterised. From these results the unpaired electron distribution in the excited state has been shown to involve a significant contribution from the hydrogen 1s orbital. Effects due to lambda doubling in the $^2\Delta$ state have also been observed for the first time and one of the lambda doubling constants determined. Further investigation of this is required however both by LIF for the higher rotational lines where the effect is much greater, the N = 20 lines are predicted to show a splitting of more than 1 GHz. It should also be possible to observe several spin-rotation transitions in the $^2\Delta$ state by MODR which are expected to show effects due to lambda doubling, these measurements will also lead to a more precise characterisation of the fine and hyperfine structure in the $A^2\Delta$ state.

References

1. L.Gero, Z. Phys. **118**, 27-36 (1941).
2. N.H.Keiss and H.P.Broida, Astrophys. J. **123**, 166-171 (1956).
3. G.Herzberg and J.W.C.Johns, Astrophys. J. **158**, 399-418 (1969).
4. A.E.Douglas and G.A.Elliott, Can. J. Phys. **43**, 496-502 (1965).
5. K.M.Evenson, H.E.Radford and M.M.Moran Jr. Appl. Phys. Lett. **18**, 426-429 (1971).
6. O.E.H.Rydbeck, J.Ellder and W.M.Irvine, Nature (London) **246**, 466-468 (1973).
7. B.E.Turner and B.Zuckerman, Astrophys. J. Lett. **187**, L59-L62 (1974).
8. J.T.Hougen, J.A.Mucha, D.A.Jenning and K.M.Everson, J. Mol. Spectrosc. **72**, 463-483 (1978).
9. J.M.Brown and K.M.Evenson, J. Mol. Spectrosc. **98**, 392-403 (1983).
10. J.M.Brown and K.M.Evenson, Astrophys. J. **268**, L51-L56 (1983).
11. C.R.Brazier and J.M.Brown, J. Chem. Phys. **78**(3), 1608-1610 (1983).
12. M.Bogey, C.Demynck and J.L.Destombes, Chem. Phys. Lett. **100**, 105 (1983).
13. L.M.Ziurys, Private Commmunication, 1983.
14. J.Cariou and P.Luc, "Atlas du spectre d'absorption de la molecule de tellure", CNRS II, Orsay, 1980.
15. M.Kakimoto and T.Kasuya, J. Mol. Spectrosc. **94**, 380-392 (1982)
16. J.Brzozowski, P.Bunker, N.Elander and P.Erman, Astrophys. J. **207**, 414-424 (1976).
17. J.M.Brown, E.A.Colbourn, J.K.G.Watson and F.D.Wayne, J. Mol. Spectrosc. **74**, 294-318 (1979).
18. J.M.Brown, M.Kaise, C.M.L.Kerr and D.J.Milton, Molec. Phys. **36**, 553-582 (1978).
19. K.P.Huber and G.Herzberg, "Constants of Diatomic Molecules", Van Nostrand Reinhold Co. New York, 1979.

20. A.Carrington and A.D.McLachlan, "Introduction to Magnetic Resonance", Harper & Row, New York, 1967.
21. W.G.Richards H.P.Trivedi and D.L.Cooper, "Spin Orbit coupling in molecules", Oxford University Press 1981.
22. L. Veseth, J. Phys. B, **3**, 1677-1691 (1970).
23. D.H.Levy and J.Hinze, Astrophys. J. **200**, 236-238 (1975).
24. J.M.Brown, D.J.Milton and T.C.Steimle, Faraday Discussions RSC, No. 71, Faraday Symposium 71 (1981).
25. T.C.Steimle, Private Communication, 1983
26. M.Takami, Jap. J. Appl. Phys. **15**, 1889-1897 (1976).
27. P.B.Ayscough, "Electron Spin Resonance in Chemistry", Methuen, London, 1967, Appendix 3.
28. H.M.McConnell and J.Strathdee, Mol. Phys. **2**, 129-138 (1959).
29. R.M.Pitzer, C.W.Kern and W.N.Lipscomb, J. Chem. Phys. **37**, 267-274 (1962).

Chapter 7 The $A^2\Delta$ - $X^2\Pi$ system of SiH

Introduction

The energy levels and thus the spectrum of SiH are in many ways quite similar to that of CH. In particular the ground states are both $^2\Pi$ and exhibit lambda doubling effects of approximately the same size. It is also thought that there are large amounts of SiH in interstellar space, based on the high concentration found of silicon atoms in many regions. Unfortunately no direct astrophysical observations of SiH have so far been made despite many searches. The lambda doubling transition in the lowest rotational level F_1 J=1/2 at about 3 GHz has been the main object of these searches. Several estimates of this transition have been made based on the optical spectrum (1)(2) using extrapolation from higher rotational levels, although Klynning et al (2) measure the 3 GHz splitting directly they consider this inferior to their extrapolated value. Recently the SiH spectrum has been recorded using fourier transform spectroscopy in the infra-red (5) and by LMR in the mid (6) and far (7) infra-red regions leading to improved values for the lambda doubling constsnts (7). Theoretical calculations of the lambda doubling frequencies have also been made (3)(4), similar calculations have been shown to be fairly accurate for CH, see chapter 6.

It has not so far been possible however to make direct laboratory measurements of the lambda doubling frequencies by observing the microwave spectrum and it was the intention of this work to make these observations. The technique of MODR was shown to be very sensitive in making the first laboratory measurements of the CH microwave spectrum, described earlier, and it was hoped to use the same technique to measure the spectrum of SiH.

Figure 1. The $A^2\Delta - X^2\Pi$ system of SiH recorded by scanning the dye-laser broadband at approximately 1 cm^{-1} resolution. Many of the features shown are due to other species for example SiH_2 and SiHF. This congestion makes the spectrum much more difficult to examine than was the case for CH.

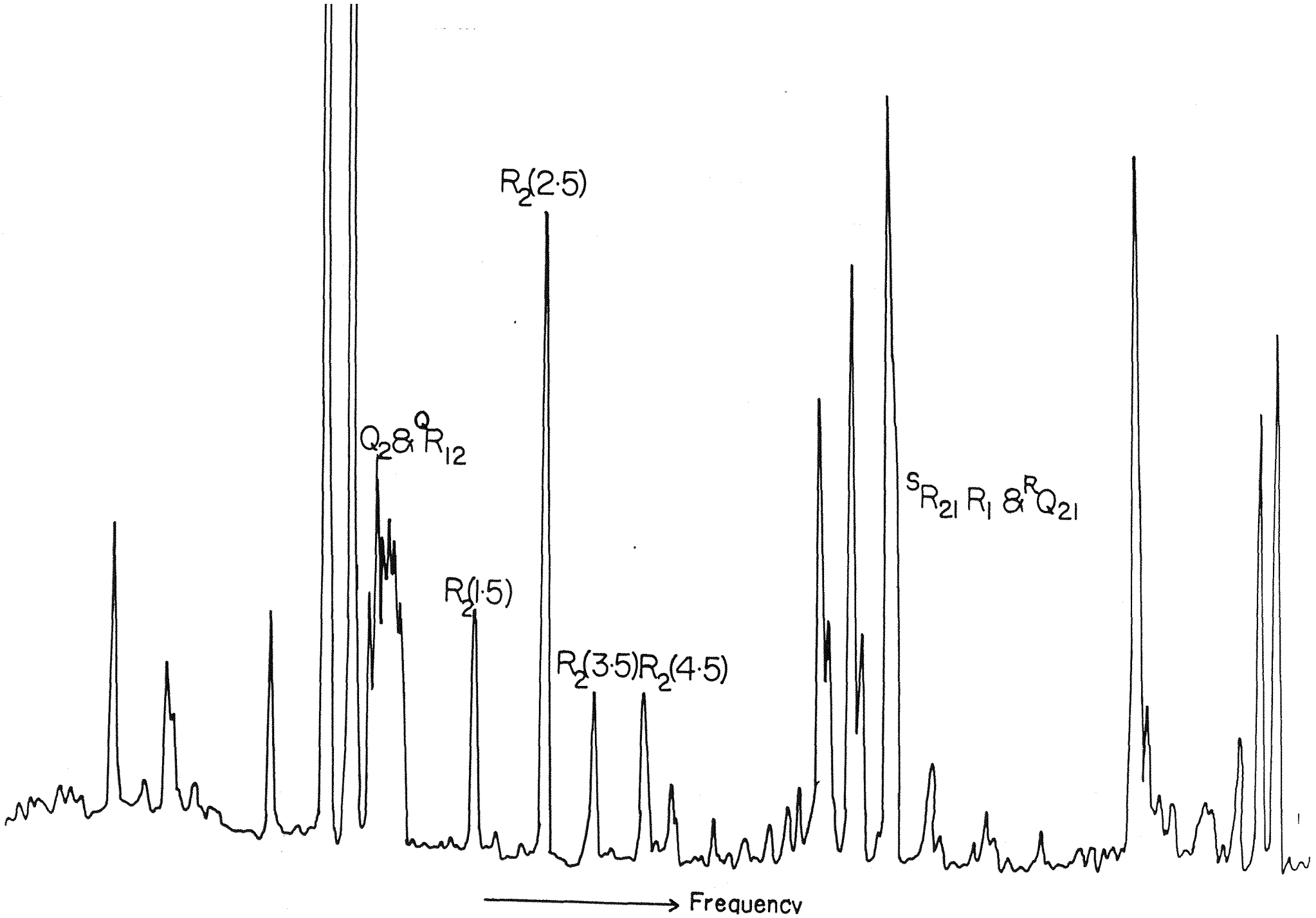
$R_2(2{\cdot}5)$
$Q_2 \& {}^{Q}R_{12}$
$R_2(1{\cdot}5)$
$R_2(3{\cdot}5) R_2(4{\cdot}5)$
${}^{S}R_{21}\, R_1 \& {}^{R}Q_{21}$
Frequency

Experimental and Observations

It is possible to produce SiH by several different methods, but the initial observations were made by reacting silane, SiH_4, with the products of a microwave discharge of fluorine in helium as was done successfully for CH. This resulted in production of significant quantities of SiH and the spectrum recorded with 1 cm^{-1} resolution is shown in figure 1. While the lines due to SiH are clearly visible there are also a large number of strong lines due to other species such as SiH_2, SiHF etc. Unfortunately, these overlap the SiH spectrum, especially parts of the R branches which are the strongest bands for the $A^2\Delta - X^2\Pi$ transition of SiH. An additional problem was that a white deposit formed quite rapidly on the walls of the reaction cell, obscuring the laser induced fluorescence signal. This necessitated frequent dismantling of the apparatus for cleaning which clearly was not very convenient. To overcome this problem a new cell was constructed with an extension port and window through which the fluorescence could be viewed, this is shown in figure 2. Using the new cell it was possible to record spectra for about an hour before the window became obscured.

The radiation source for these experiments was an argon ion laser producing about 1.8 Watts in the ultraviolet, pumping a dye-laser operating with Stilbene 3. The $A^2\Delta - X^2\Pi$ system of SiH lies at about 410 nm which is at the extreme blue end of the lasing range for Stilbene 3 and operating without intracavity etalons it was possible to obtain only about 150 mWatts. When the laser was operated single frequency it was very hard to obtain any power at all with the best output being only 5 to 10 mWatts. Consequently the laser output was somewhat unstable, making the recording of spectra difficult. Another problem is that the tellurium atlas does not cover this part of the visible region and lines could be identified only by reference to a monochrometer and use of the measured SiH frequencies (2).

Despite these problems the $^sR(0.5)$ line, which goes

Figure 2. Improved cell design for the detection of SiH signals. The use of a teflon slit and a side arm with an observation window, dramatically reduces the rate of deposition on the surface through which the fluorescence signal is detected.

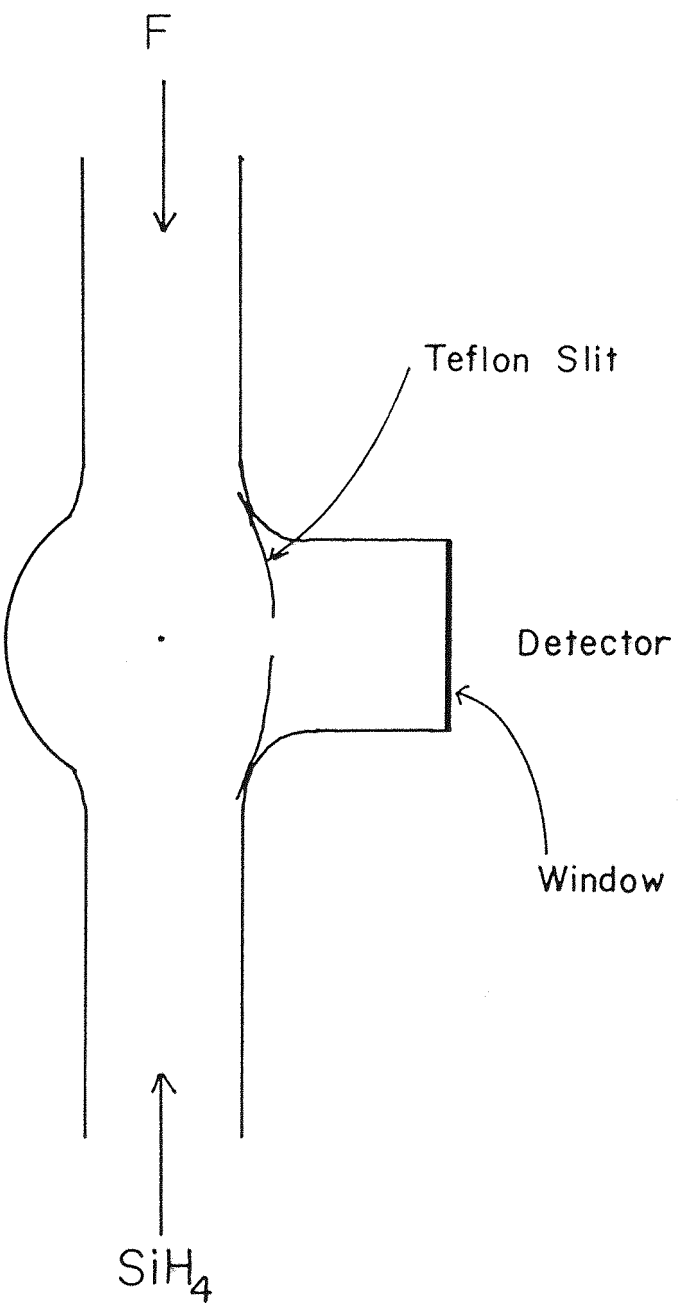
F
Teflon Slit
Detector
Window
SiH4

Figure 3. Possible hyperfine structure at Doppler-limited resolution on the $^{s}R_{21}(0.5)$ line of the (0,0) band of the $A^2\Delta - X^2\Pi$ system of SiH. The lambda doubling splitting in the ground state is also shown.

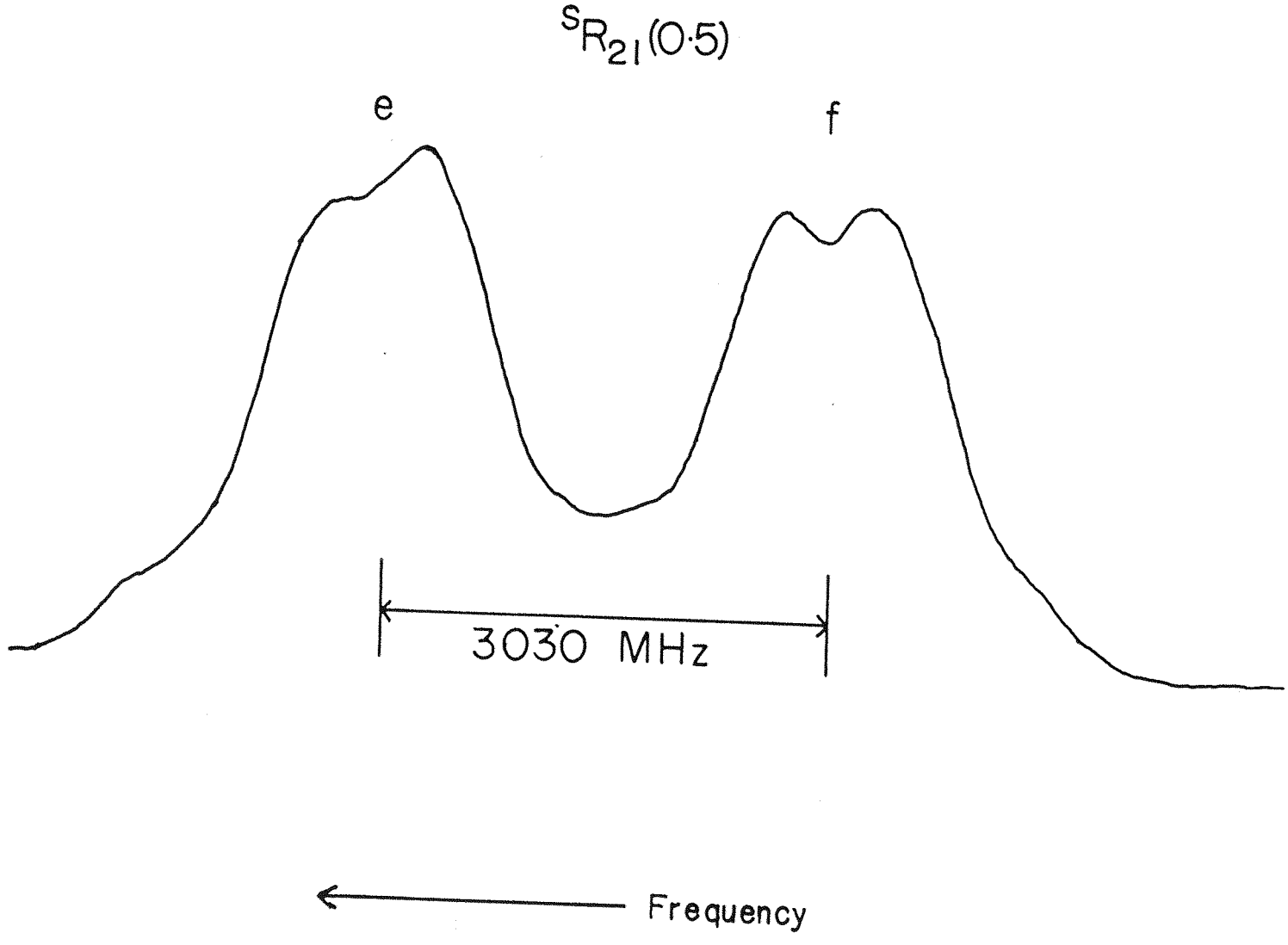
$^{S}R_{21}(0\cdot5)$
e
f
3030 MHz
Frequency

from the lowest rotational level in the ground state, was recorded at Doppler-limited resolution. Out of a total of 22 scans only two without laser 'mode-hops' were obtained, one of these is shown in figure 3. The main splitting is the $^2\Pi$ lambda doubling but each component appears to show some further splitting which must be hyperfine structure, if it is real. The only other possibility is some strange mode effect due to the laser, effects like this were observed at other times, but in this case the splitting seems to be reproducible. One problem is that the transition to the F=2 component in the excited state which has the highest intensity should be on the low frequency side in each lambda doublet but in fact is to the high frequencty side in one of them. The only explanation for this is that there are weak transitions underlying the main signals, there is some evidence of these either side of the $^sR(0.5)$ lines. The splitting is about 500 MHz which must be due mainly to hyperfine effects in the $A^2\Delta$ state as the ground state splitting, based on calculated hyperfine constants (8), is only 11 MHz. The $^2\Delta$ J = 3/2 level in CH has a splitting of only 160 MHz and for PH^+ which is iso-electronic with SiH it is 308 MHz (9) in the v=1 level. Neither of these are as large as the value obtained from the SiH spectrum. If the observed splitting is real then a rather large b value of about 1000 MHz is required. This would result in even larger splittings in other lines, than those observed for $^sR(0.5)$ but unfortunately no further measurements were made at the time of the original recording.

It is also possible to make an estimate of the ground state lambda doubling from the $^sR(0.5)$ transition. Both observations which were free of laser 'mode-hops' were measured and the splitting is estimated to be 3030±25 MHz which is rather larger than the value determined from the optical spectrum by Klynning et al (2) of 2967±7 MHz. Although subsequent refitting of their data in this laboratory, with the p_o and q_o parameters allowed to vary rather than being included as corrections in the expressions for p and q, has resulted in a value of 2982 MHz. The best theo-

retical calculations (4) give a value of 3000 MHz for the splitting, while the latest LMR results (7) predict 3006 MHz. The main purpose of the study was to measure the microwave spectrum however, and in order to improve the possibility of doing this other methods of production of SiH were investigated. In previous studies (2) SiH had been generated using a hollow cathode source, but at this time no such source was available. As an alternative the possibility of producing silicon atoms by heating silicon powder in a Broida type oven, described in chapter 5, and reacting them with hydrogen gas was investigated. Despite the high temperature required, at least 1500°C to melt the silicon, some signals were observed, possibly due to SiF, but none were identifiable as SiH. Following these experiments a hollow cathode source similar to that used by Klynning et al (2) was constructed but no attempt to produce SiH has been made.

Unfortunately the UV output of the argon ion laser was falling quite rapidly at this time and once this dropped below about 1.6 Watts it was no longer possible to obtain single frequency output at 410 nm. Hence further investigation of the laser induced fluorescence spectrum was not possible nor could any search for the MODR transitions be made.

Conclusion

It has been possible to observe laser induced fluorescence spectra of SiH both at 1 cm^{-1} and Doppler-limited resolution, however this was extremely difficult as it involved operating on the extreme edge of the gain curve for Stilbene 3. A more extensive investigation requires a laser dye somewhat easier to operate in this region. The ideal dye is Stilbene 1 which should give about 30 mWatts single mode at 410 nm. Unfortunately it has a rather higher threshold than Stilbene 3 and requires about 3 Watts of UV radiation to pump it efficiently. Use of a ring dye laser rather than standing wave would also give a considerable

improvement with a single mode output of about 100 mWatts in this region. Thus although the measurement of the SiH microwave spectrum should be quite straightforward, the region of the optical transition means that rather heavy investment in the appropriate lasers is required.

References

1. A.E.Douglas and G.A.Elliott, Can. J. Phys. **43**, 496-502 (1965).
2. L.Klynning, B.Lindgren and U.Sassenberg, Phys. Scrip. **20**, 617-619 (1979).
3. I.D.L.Wilson and W.G.Richards, Nature, **258**, 133-134 (1975).
4. D.L.Cooper and W.G.Richards, J. Chem. Phys. **74**, 96-98 (1981).
5. J.C.Knights, J.P.M.Schmitt, J.Perrin and G.Guelachvili, J. Chem. Phys. **76**, 3414-3421 (1982).
6. J.M.Brown and D.R.Robinson, Mol.Phys. submitted.
7. J.M.Brown, R.F.Curl Jr. and K.M.Evenson, Astrophys. J. and J. Mol. Spectrosc. to be published.
8. P.J.Sarre, Private communication, 1983.